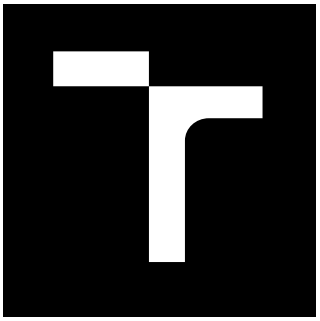

BRNO UNIVERSITY OF TECHNOLOGY

VYSOKÉ UČENÍ TECHNICKÉ V BRNĚ

FACULTY OF MECHANICAL ENGINEERING

FAKULTA STROJNÍHO INŽENÝRSTVÍ

INSTITUTE OF PHYSICAL ENGINEERING

ÚSTAV FYZIKÁLNÍHO INŽENÝRSTVÍ

DETECTION AND CHARACTERIZATION OF LASER-INDUCED PLASMAS

ZOBRAZOVANÍ A CHARAKTERIZACE LASEREM BUZENÉHO PLAZMATU

MASTER'S THESIS

DIPLOMOVÁ PRÁCE

AUTHOR — **Bc. Josef Hrdlička**

AUTOR PRÁCE

SUPERVISOR — **Ing. Jakub Buday, Ph.D.**

VEDOUCÍ PRÁCE

BRNO 2025

BRNO UNIVERSITY OF TECHNOLOGY
FACULTY OF MECHANICAL ENGINEERING

Assignment of Master's thesis

Institute:	Institute of Physical Engineering
Student:	**Bc. Josef Hrdlička**
Degree program:	Physical Engineering and Nanotechnology
Branch:	No specialization
Supervisor:	**Ing. Jakub Buday, Ph.D.**
Academic year:	2024/25

As provided by Act No. 111/98 Coll. on higher education institutions and the BUT Study and Examination Regulations, the director of the Institute hereby assigns the following topic of master's thesis:

Detection and characterization of laser–induced plasmas

Brief description of the thesis topic:

Detection and characterization of the laser-induced plasma provides the opportunity to obtain additional ablation data typical for LIBS. These data are typically used to standardize LIBS spectra, determine the temperature or electron density of the plasma, and for other purposes. All of these parameters are important for advanced analysis. Therefore, this work deals with more advanced characterization of laser-induced plasma and the use of other data obtained for its standardization.

Objectives of the Master's thesis:

1. Literature search on the topic.
2. Implement the Mach-Zehnder interferometer in the experimental setup of LIBS.
3. Plasma plume analysis using a Mach-Zehnder interferometer
4. Data processing and evaluation

Recommended bibliography:

MIZIOLEK, Andrzej W.; PALLESCHI, Vincenzo a SCHECHTER, Israel (ed.), 2006. Laser-induced breakdown spectroscopy (LIBS): fundamentals and applications. Cambridge: Cambridge University Press. ISBN 978-0-521-07100-0.

Deadline for submission of the master's thesis is given by the schedule of the academic year 2024/25.

In Brno,

L. S.

……	……
prof. RNDr. Tomáš Šikola, CSc.	doc. Ing. Jiří Hlinka, Ph.D.
Director of the Institute	FME dean

Abstrakt

Tato diplomová práce popisuje vývoj a demonstraci Mach–Zehnderova interferometru integrovaného do systému Spektroskopie Laserem Buzeného Plazmatu (LIBS) pro měření časově i prostorově rozlišené elektronové hustoty a dynamiky rázových vln v laserem buzeném plazmatu. Jako excitační zdroj byl nově využit infračervený Ho:YAG laser o vlnové délce 2090 nm (délka pulsu 4 ns, energie 3.65 mJ), který byl porovnán s konvenčním Nd:YAG laserem s 1064 nm (délka pulsu 5 ns, energie 23 mJ) na ocelových vzorcích různých tvrdostí (H0–H6) a na mědi. Vše bylo měřeno za laboratorních podmínek. Pro dosažení stabilních interferenčních proužků byly optické komponenty upevněny v tuhé klecové konstrukci, čímž se minimalizovaly větší mechanické posuny. Byl vytvořen poloautomatizovaný skript v jazyce Python, který je schopný zpracovat rozsáhlou sadu interferenčních obrazců. Provádí ořez obrazu, extrakci fázového posunu pomocí Fourierovy transformace, Abelovu inverzi, výpočet hustoty elektronů a segmentaci plazmatu během několika sekund na jeden snímek. Mezi klíčová zjištění patří vyšší hustoty elektronů v plazmatu a ostřejší interferenční proužky rázových vln u excitace na 1064 nm, což lze přisoudit vyšší energii fotonů. Byla prokázána jasná korelace mezi tvrdostí vzorku a hustotou elektronů, přičemž měď vykazovala nejnižší hodnoty. Tato výsledná data potvrzují účinnost Mach–Zehnderova uspořádání pro kvantitativní diagnostiku plazmatu a představují 2090 nm excitační laser jako novou perspektivní vlnovou délku pro LIBS, zejména v kombinaci s automatizovanou analýzou obrazů pro efektivní zpracování velkých objemů dat.

Summary

This diploma thesis reports the development and demonstration of a Mach–Zehnder interferometer integrated into a Laser-Induced Breakdown Spectroscopy (LIBS) setup to measure time and spatially resolved electron density and shock-wave dynamics in laser-induced plasmas. A novel, near-infrared Ho:YAG laser at 2090 nm (4 ns pulses, 3.65 mJ) was compared to a conventional Nd:YAG source at 1064 nm (5 ns, 23 mJ) across steel samples of varying hardness (H0–H6) and copper. Measurements were done under standard laboratory conditions. To produce stable interference fringes over extended periods, optical components were mounted in a rigid cage system design, minimizing mechanical drift. A semi-automated Python-based processing script was created to handle the vast interferogram dataset, performing image cropping, Fourier-transform phase extraction, Abel inversion, electron density calculation, and plasma segmentation in seconds per frame. Key findings include higher plasma electron densities and more distinct shock-wave fringes for 1064 nm excitation, attributable to its greater photon energy. A clear correlation between sample hardness and electron density, with copper exhibiting the lowest values. These results validate the Mach–Zehnder approach for quantitative plasma diagnostics and introduce the 2090 nm pump laser as a promising new wavelength for LIBS, particularly when combined with automated image analysis for high-throughput data processing.

Klíčová slova
LIBS, laser-indeced plasma, plazma, ablace, abelova transformace, elektronová hustota, atomární spektrum, Mach-Zehnder Interferometer, zpracování obrazu.

Keywords
LIBS, laser-indeced plasma, plasma, ablation, abel transform, electron density, atomic spectra, Mach-Zehnder Interferometer, image processing.

HRDLIČKA, J.*DETECTION AND CHARACTERIZATION OF LASER-INDUCED PLASMAS*. Brno University of Technology, Faculty of Mechanical Engineering, 2025. 78 s. Supervisor Ing. Jakub Buday, Ph.D.

I hereby declare that this thesis is my original work, carried out independently under the supervision of Ing. Jakub Buday, Ph.D., and that all sources I have used are listed in the bibliography.

Bc. Josef Hrdlička

Rád bych touto cestou vyjádřil upřímné poděkování svému vedoucímu práce Ing. Jakubu Budayovi, Ph.D., za jeho trpělivost, cenné rady a neustálou podporu v nejednoznačných a náročných chvílích mého výzkumu. Děkuji také své rodině a přátelům za jejich morální podporu, pochopení a povzbuzení, které mi umožnily práci úspěšně dokončit. Závěrem děkuji svým přátelům s tlapkami, kteří tolerovali mou nepřetržitou přítomnost při zpracování dat a byli mi v nejedné chvilce příjemnou společností.

Bc. Josef Hrdlička

Contents

Introduction

Laser–Induced Breakdown Spectroscopy (LIBS) is a powerful, minimally invasive analytical technique that utilizes focused, pulsed laser irradiation to ablate a small volume of material, generating a transient plasma whose optical emission encodes the elemental composition of the target. While the majority of LIBS research has historically employed ultraviolet (UV) to near-infrared (NIR) pump wavelengths, most commonly the 1064 nm fundamental of Nd:YAG lasers, or long-wavelength CO_2 sources at 10 µm, the intermediate NIR regime around 2 µm remains largely unexplored. In particular, no published study has to date leveraged a 2090 nm Ho:YAG laser for LIBS measurements, despite the unique ablation and plasma characteristics expected at that wavelength.

The primary goal of this thesis is to design, build, and validate a time-resolved Mach–Zehnder interferometer (MZI) integrated into a LIBS setup, and to compare its diagnostic performance using both a conventional 1064 nm pump laser and a novel 2090 nm pump source under standard laboratory conditions. To achieve this, three interrelated objectives were pursued:

1. **Optical design and implementation of MZI**: develop a mechanically stable, free-space Mach–Zehnder arrangement capable of producing high-contrast fringes over longer time periods.

2. **Automated interferogram processing**: implement a Python-based pipeline to perform image cropping, Fourier-transform phase extraction, Abel inversion, using the Drude model to calculate electron density, and plasma segmentation, reducing processing time from ∼10 min per frame to a few seconds.

3. **Data evaluation**: extracting the average electron density from the segmented plasma and comparing it across all samples. Then correlate the integrated spectral intensity with these density values and compare the results against data from literature to prove the functionality of the whole process.

Accurate determination of electron density in LIBS plasmas is critical for quantitative elemental analysis. By providing spatially and temporally resolved electron density profiles, the Mach–Zehnder interferometer enables tighter correlation between spectral emission intensities and plasma conditions, which in turn improves calibration curve linearity (higher R^2 values) and reduces measurement variability. Moreover, combining these interferometric density measurements with conventional spectral data offers complementary insights, using the emission spectra to support and refine plasma parameter interpretation, ultimately yielding more reliable sample analyses.

The theoretical underpinnings of LIBS emission, interferometric plasma diagnostics, and Abel inversion are reviewed in Chapter 1. Chapter 2 includes all the experimental work done in this thesis. Chapter 2.2 describes the mechanical design of the Mach–Zehnder interferometer, including the rigid cage-system mount that minimizes drift and maintains fringe contrast over hours of operation. In Chapter 2.3 are details on the measurement process. Chapter 2.6 presents the development of the semi-automated image-processing script, outlining each processing step and validating its accuracy. The experimental results

of electron density maps, shock-wave fringe analysis, and comparative metrics between the two probe laser wavelengths are reported in Chapter 2.8. Finally, Chapter 3 summarizes the key findings, discusses limitations, and proposes directions for future work.

This work makes several novel contributions: (i) the first demonstration of a 2090 nm pump laser in a LIBS experiment, (ii) a robust Mach–Zehnder interferometric platform for time-resolved plasma diagnostics, and (iii) a reproducible image-analysis framework that enables high-throughput data processing. By combining these innovations, I established a versatile diagnostic toolset that can be extended to other laser-plasma interactions, materials analyses, and dynamic phenomena.

1. Theoretical part

In the first section 1.1, the general properties of plasma provide a foundation for understanding the behavior of this state of matter. Then, the specific properties of laser-induced plasma and ablation are discussed. The LIBS chapter 1.2 is focused on the application of laser-induced plasma and the description of spectra, which also describes the measurement setup and individual components of the LIBS system. Finally, in section 1.3, the theory behind interferometry and tomography of plasma is examined.

1.1. Plasma

Plasma is the fourth state of matter. It consists of negatively charged electrons, positively charged ions, and neutral atoms. As a quasi-neutral gas, it contains approximately equal numbers of positive and negative charges within its volume, making it appear overall electrically neutral. The plasma contains free charge carriers, which collectively generate and respond to electromagnetic fields [1].

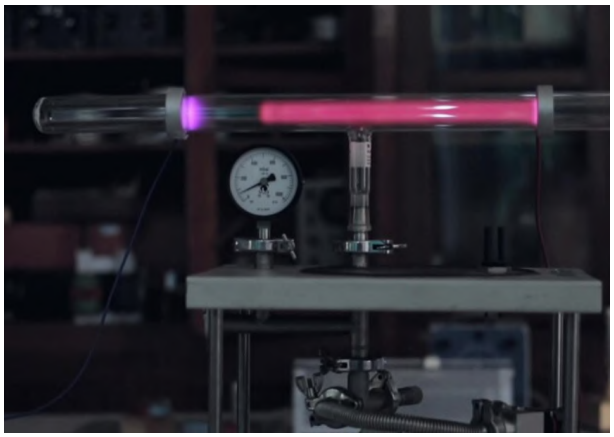

Figure 1.1: A glow discharge is an electrical discharge that occurs at reduced pressure in a tube filled with a noble gas, producing a glowing plasma. Taken from [2].

To transform any substance into plasma, it must undergo a phase transition. The process of converting any state of matter into plasma is called ionization, while the reverse process is known as recombination. During ionization, one or more electrons are removed from the electron shell of an atom or molecule. Free electron and an ion are produced. Ionization can be triggered by thermal energy, absorption of electromagnetic radiation, or an electrical discharge. In solids, liquids, and gases, first-order phase transitions occur. This means they involve latent heat. Energy supplied during the transition is absorbed at constant temperature (preserving the system's kinetic energy), while the material's density changes suddenly (due to a change in internal energy U). In contrast, the transition into plasma is considered a second-order phase transition, which does not involve latent heat [3]. Ionization in gases occurs gradually, and the density of charged particles in the plasma increases progressively, as illustrated in Figure 1.2.

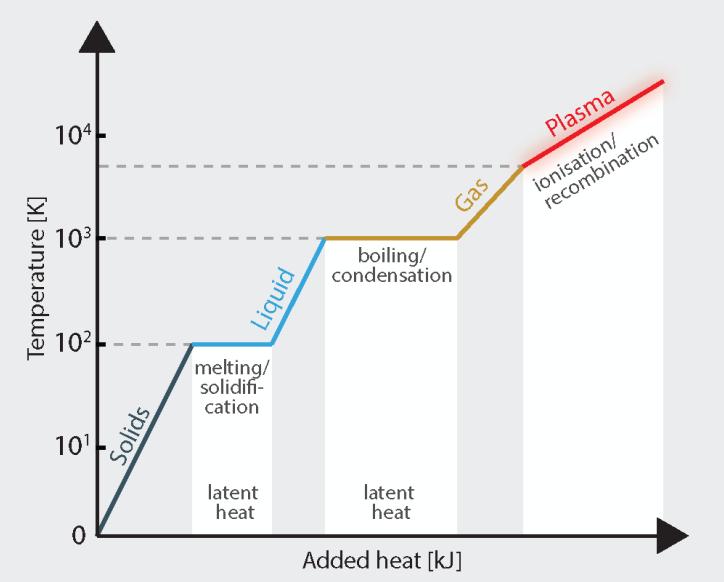

Figure 1.2: A graph showing the dependence of temperature on added heat (Enthalpy ΔH) for a typical metal. Both first-order and second-order phase transitions are illustrated. Inspired by [4], with the plasma state added based on [3].

Ionization energy varies with the atomic number of the element and exhibits periodic trends (see Figure 1.3). Noble gases are more difficult to ionize due to their fully occupied valence orbitals. In contrast, the elements most easily ionized are found in Group 1 of the periodic table (alkali metals and hydrogen). In a plasma, an element can generally undergo multiple ionizations.

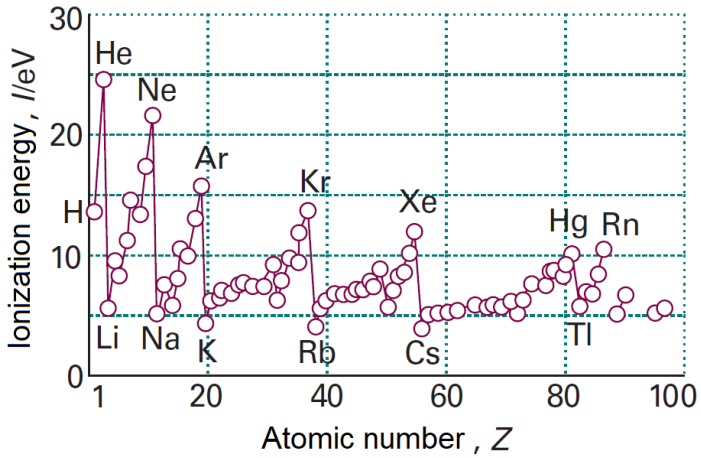

Figure 1.3: A graph of first ionization energy as a function of atomic number. Taken from [3].

1.1.1. General plasma parameters

Due to their low mass, electrons are much more mobile than ions and therefore serve as the primary carriers of energy in a plasma. As a result, the main parameters used to describe plasma are the electron temperature T_e (K) and the electron density n_e cm^{-3}),

which represents the number of free electrons per unit volume of the plasma.

Coulomb forces play a key role in describing plasma behavior. Consider a positively charged particle placed in an otherwise electrically neutral plasma, as illustrated in Figure 1.4. This particle generates an electric field that disturbs the plasma equilibrium. To restore balance, surrounding electrons redistribute themselves around the charged particle, partially canceling its electric field. This leads to an exponential decay of the field of the point charge, characterized by the Debye length λ_D, at which both the electric potential and field fall to $1/e$ of their original value given by Coulomb's law. For an ionized plasma in thermodynamic equilibrium, the Debye length is given by:

$$\lambda_D = \sqrt{\frac{\varepsilon_0 k_B T}{(1+z) n_e e^2}} \text{ (m)}, \tag{1.1}$$

where ε_0 is the vacuum permitivity, k_b is Boltzmann constant, T is the plasma temperature, z is the ionization degree, and e (C) is the elementary electron charge.

The region in which electrostatic interactions between individual particles are non-negligible is called the Debye sphere. Beyond this boundary, the potential of a point charge is considered effectively shielded. Particles outside the sphere experience only the smooth, averaged electric field produced by the collective behavior of all particles within the sphere. The number of particles inside the Debye sphere is given by:

$$N_D = 4/3\pi\lambda_D^3 n_e, \tag{1.2}$$

Another quantity describing electrostatic behavior in a plasma is the coupling parameter Γ. It expresses the ratio of the Coulomb potential energy between charged particles to their average kinetic energy, which corresponds to the thermal energy of the electrons. This dimensionless parameter quantifies how strongly the particles are electrostatically bound to each other compared to their thermal motion. For non-degenerate particles, the relationship is given by:

$$\Gamma = \frac{E_p}{E_k} = \frac{\left(\frac{e^2}{4\pi\varepsilon_0}\right) z^2 \sqrt[3]{n_e}}{k_B T_e}, \tag{1.3}$$

where r is the mean separation distance between particles of a given type. The kinetic energy is proportional to the electron temperature $E_k \sim T_e$, which expresses the intensity of their random thermal motion. The potential energy in a homogeneous plasma depends on the electron density and the ionization degree $E_p \sim z^2 \sqrt[3]{n_e}$ [5].

Plasma can behave as either ideal or non-ideal, depending on how strongly particles interact through electrostatic forces. It is considered ideal when the Debye sphere contains a large number of particles ($N_D >> 1$), as illustrated in Figure 1.4 part A. In this case, the Debye length is much smaller than the characteristic size of the plasma L (e.g. radius), meaning $\lambda_D << L$. The electrostatic fields of individual particles are effectively shielded. Here, particles interact mainly through an averaged, smooth, collective electromagnetic field rather. They move freely with minimal collisions. This condition is expressed by $\omega\tau > 1$, where ω is the particle oscillation frequency in plasma and τ is the mean time

between collisions. In other words, particles have enough time to respond to collective fields before undergoing a collision. An ideal plasma can often be described by the general gas equation, and is typically found in environments with high temperature or low density, where particles possess high kinetic energy and are only weakly coupled ($\Gamma << 1$).

In contrast, when the Debye sphere contains relatively few particles ($N_D << 1$), Coulomb forces are only partially screened, as shown in Figure 1.4 part C. The plasma is then considered non-ideal. In this regime, collisional processes dominate, and interactions between individual particles are more local. The condition $\omega\tau < 1$ now indicates that particles collide before they can respond to collective fields. This behavior typically arises in dense or cold plasmas, or in metals, and corresponds to a strongly coupled plasma $\Gamma >> 1$, where the ideal gas model no longer applies.

Between these two extremes lies an intermediate regime known as warm dense matter (WDM), where $\Gamma \approx 1$. In this state, both collective effects and particle collisions are significant. Electron and ion temperatures are not necessarily in thermal equilibrium, and the behavior of the plasma depends on both types of interactions. Approximations for modeling this regime are discussed in more detail in Chapter 1.1.5, which focuses on local thermodynamic equilibrium (LTE).

All information in this subsection is taken from [1, 6].

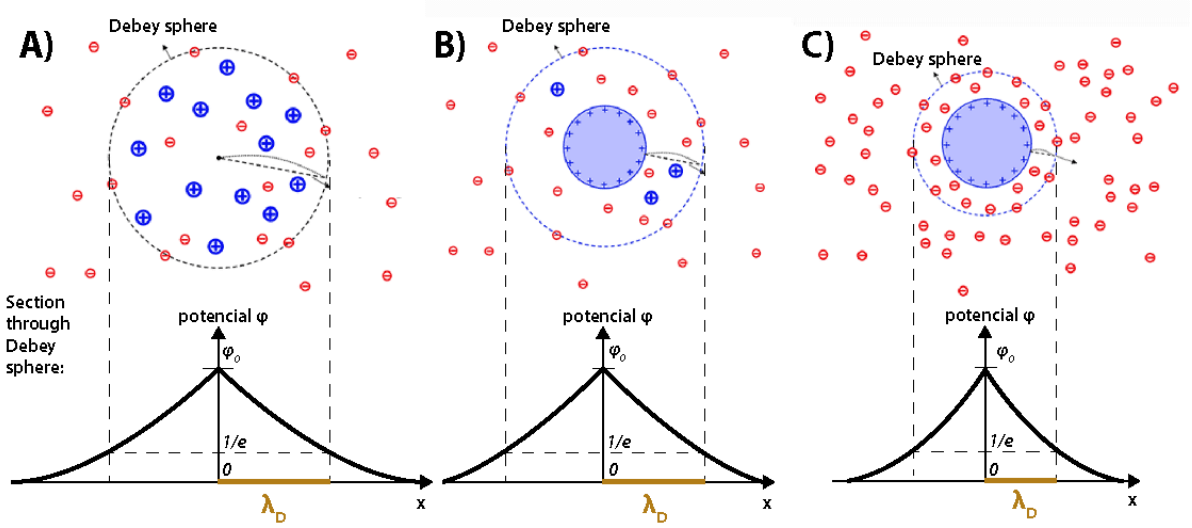

Figure 1.4: A), B), and C) are 2D diagrams illustrating charge distributions around the Debye sphere. Each diagram includes a cross-section of the Debye sphere alongside the corresponding electric potential profile. Blue circles represent positively charged ions, while red circles represent negatively charged electrons. A) A single charged particle maintains local neutrality; this represents the case of an ideal plasma. B) When electron density N_e is low, then the Debye length λ_D becomes large, resulting in a gradual decline of the electric potential. The blue ring indicates the effective range of negative charge. C) In a high-density plasma where N_e is large, the Debye length λ_D is short. The potential drops rapidly with distance, which is characteristic of non-ideal plasma behavior. Diagrams adapted from [7], with potential profiles added from [6].

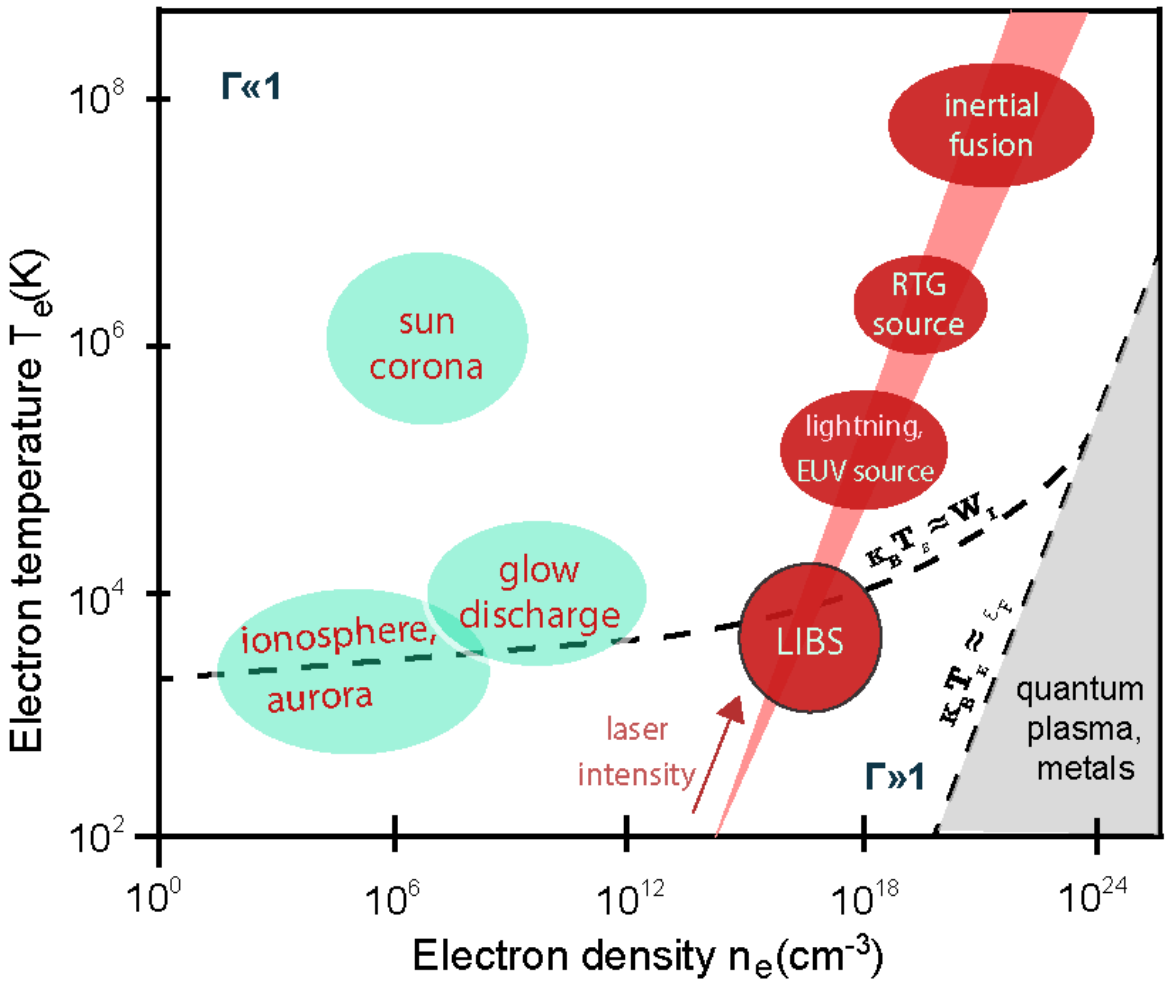

Figure 1.5: The graph divides plasma into regions based on the potential energy of hydrogen $E_p = k_B T_e$ and includes examples of different plasma types outlined by colored ellipses. These examples are not limited to hydrogen alone. On the right side lies the quantum plasma region, where the plasma is dense and cold enough to exhibit quantum behavior described by Fermi–Dirac statistics (e.g., metals). Outside this region, the plasma follows Boltzmann statistics and can be treated as a classical system, where the degeneracy of the electron gas is negligible. In this classical regime, the potential energy exceeds the Fermi energy of electrons ε_F, making quantum effects such as electron degeneracy negligible. The full ionization line indicates the condition under which hydrogen becomes singly ionized, specifically, when the electron thermal energy exceeds the ionization energy W_i. Well-known examples of plasma are highlighted in green, spanning a wide range of densities: from low-density systems like the ionosphere and aurora, to higher-density environments such as the solar corona, glow discharges, and lightning. Lightning overlaps with the EUV sources. Examples of laser-produced plasma applications are highlighted in red ellipses. These represent increasing laser intensity: LIBS, EUV plasma sources, plasma X-ray sources, and inertial confinement fusion. The base graph is adapted from [1], with laser-driven plasma examples added from [8].

1.1.2. Wave propagation in plasma

Plasma can transmit various transverse and longitudinal waves in response to external stimuli. For our purposes, a classical model is sufficient to describe wave behavior. The assumptions of this model are based on kinetic gas theory, as described for example in [9].

We now consider plasma waves and oscillations in the absence of an external magnetic field. Because ions have much greater mass than electrons, they are unable to respond to high-frequency stimuli such as visible light. We thus assume the ions have infinite mass, allowing us to neglect their movement entirely. The thermal motion of electrons is also neglected. The optical properties of plasma are then described only by free electrons. The Drude dispersion model, also called the cold plasma model, describes how free electrons interact with electromagnetic waves. The dielectric function describing such dispersion has the following form:

$$\varepsilon_r(\omega) = 1 - \frac{\omega_p}{\omega^2 + i\gamma\omega}, \tag{1.4}$$

where ω is the frequency of the electromagnetic wave interacting with the plasma, $\gamma = 1/\tau$ is the damping constant, and ω_p is the plasma frequency. The plasma frequency represents the natural oscillation frequency of the electron gas at which the relative permittivity $\varepsilon_r(\omega_p) = 0$. It is described by:

$$\omega_p = \sqrt{\frac{n_e e^2}{\epsilon_0 m_e}}\ (\text{Hz}), \tag{1.5}$$

where m_e(kg) is the electron mass. The plasma frequency is a fundamental parameter in describing plasma behavior and depends solely on the electron density n_e. All free electrons oscillate in phase as a collective motion at this frequency.

Figure 1.6 shows the dielectric function from the Drude model, while Figure 1.7 displays the corresponding reflectivity. When $\omega < \omega_p$, the dielectric function becomes negative, and the wave number describing propagation $k = N_O \frac{\omega}{c}$ becomes purely imaginary. This leads to exponential attenuation of the wave in the direction of propagation, and the wave is reflected. In this regime, the plasma behaves like a mirror. Conversely, when $\omega > \omega_p$, both the dielectric function and the wave vector are real numbers. In this case, the plasma behaves like a dielectric, allowing electromagnetic waves to propagate through [10].

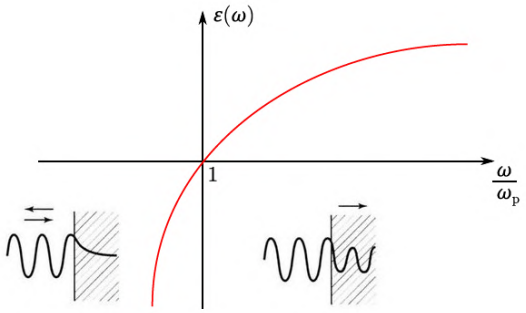

Figure 1.6: The real part of the dielectric function in the Drude model [11].

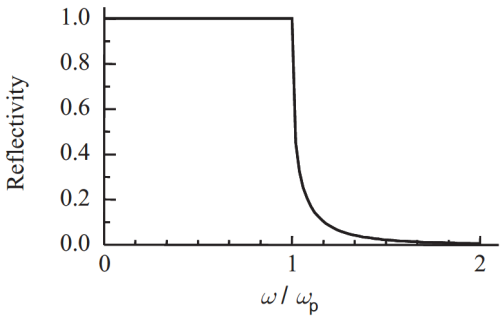

Figure 1.7: Plasma reflectivity $R = \left|\frac{N-1}{N+1}\right|^2$ [12].

As shown in the previous chapter 1.1.1, collisions are negligible in cold plasma, meaning $\tau >> \omega$, and thus the damping term can be set to $\gamma = 0$. In the absence of an external magnetic field, the refractive index for the so-called ordinary wave ("O" wave) is related to the dielectric function by $N_O = \sqrt{\varepsilon_r}$. The relationship between the refractive index and the dielectric function gives the following equation:

$$N_O(\omega) = \sqrt{1 - \frac{\omega_p^2}{\omega^2}}. \tag{1.6}$$

By substituting Equation 1.5 into Equation 1.6 and solving for n_e, we obtain the dependence of electron density on the refractive index:

$$n_e(N_0) = \frac{\omega \varepsilon_0 m_e \sqrt{1 - N_0}}{e^2}. \tag{1.7}$$

The model remains valid only up to the point when energy-level transitions occur.

1.1.3. Laser-induced plasma

Laser-induced plasma is a spatially and temporally varying plasma generated by a highly intense, focused laser beam. This is typically achieved with ultrashort laser pulses ranging from femtoseconds to milliseconds. The specifics of the laser–matter interaction depend on many laser parameters. Key laser parameters include pulse energy, laser fluence, wavelength, and pulse shape. Material parameters include elemental composition and a range of physical and chemical properties [13]. Energy is absorbed primarily via the photoelectric effect. The peak power of a pulsed laser is given by:

$$P = \frac{E}{\Delta t}\ (\mathrm{W}), \tag{1.8}$$

where E is the energy of a single pulse and Δt the pulse duration. The laser is focused to a spot just about a hundred $\mu\mathrm{m}^2$ in size. This tiny focal area concentrates the peak power and other beam parameters into a very small volume, shaping the formation and properties of the resulting microscopic plasma (i.e. microplasma). The microplasma typically expands to a maximum size of a few millimetres. The optical intensity is then defined as:

$$I = \frac{P}{S}\ \left(\frac{\mathrm{W}}{\mathrm{cm}^2}\right), \tag{1.9}$$

where S is the area illuminated by the laser beam [14].

The previous chapters and Figure 1.5 provide the foundation for a straightforward description of laser-induced plasma (LIP). Here, we concentrate on its behavior in the context of LIBS:

- The plasma is partially or fully ionized.
- It is considered a cold plasma, with temperatures below 10^6K. Collisional processes and collective behavior occur at comparable magnitudes.

- Energy-level populations follow the Boltzmann distribution. It follows classical (non-quantum) plasma behavior.
- The plasma is not in equilibrium. The laser primarily interacts with electrons, which then secondarily transfer its energy to ions in secondary. Two different temperatures are created for two different charge carriers.
- The collisions between particles are dominant. In a fully ionized plasma, charged particles interact mainly via Coulomb collisions. For partially ionized plasma the combination of collisions with electrons, ions and neutral atoms is present.
- The plasma evolves both in time and space from an optically thin to an optically thick state. In the optically thin regime, radiation generated within the plasma is able to escape. As the plasma cools and electrons recombine with ions to form neutral atoms, the plasma becomes optically thick and absorbs a portion of its own emission.

Table 1.1 summarizes the plasma parameters used in LIBS. Based on these values, we can see that the plasma behaves like a mirror up to frequencies in the Terahertz radiation region and becomes opaque for radiation at higher frequencies.

Table 1.1: An example of typical parameters for laser-induced plasma generated by a nanosecond pulse in LIBS. The values of T_e and n_e are taken from [15], values λ_D, N_D, Γ and ω_p are computed for $z = 1$ using equations 1.1, 1.2, 1.3 a 1.5.

T_e (K)	n_e (cm^{-3})	Γ	λ_D (nm)	N_D (−)	ω_p (THz)
$7 \cdot 10^3 - 4 \cdot 10^4$	$10^{16} - 10^{18}$	$0.01 - 0.24$	$4 - 100$	$0.3 - 40$	$0.9 - 9$

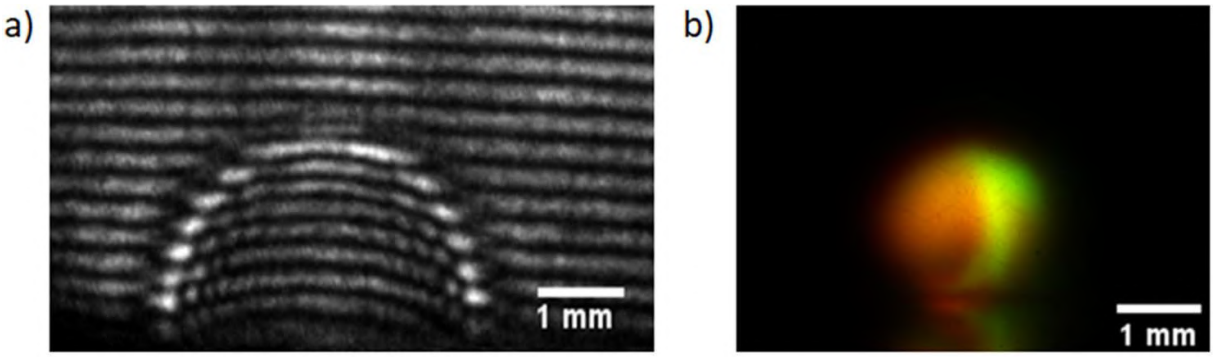

Figure 1.8: a) Interferogram a b) Emission intensity of laser-induced plasma. Both images were captured at the same time. Taken from [16].

1.1.4. Ablation

Ablation begins once the peak power of a laser pulse exceeds a certain threshold, causing atoms and molecules to be removed from the target material. For pulse durations of hundreds of picoseconds or more, the process is dominated by thermal mechanisms. For pulses of a few picoseconds or less, non-thermal processes occur. The minimum laser power required for ablation is given by the Moencke–Blankenburg relation:

$$I_{min} = \rho L_V \sqrt{\frac{\kappa}{\Delta t}}, \tag{1.10}$$

where ρ is the material density, L_V the latent heat of vaporization, and κ the thermal diffusivity [17]. In LIBS ablation, laser pulse energies typically range from a few hundred μJ up to several hundred mJ. We will now focus on the ablation dynamics of nanosecond-pulse lasers, which are widely used for their commercial availability.

Nanosecond laser

Ablation and plasma formation by a nanosecond-pulse laser occur at intensities above $10^7 \left(\frac{\mathrm{W}}{\mathrm{cm}^2}\right)$ [18]. Detailed descriptions of the ablation dynamics and plasma evolution during a single nanosecond pulse for both metals and dielectrics is now presented [15, 19, 20, 21]. The scheme in Figure 1.9 is complementary to the text.

1. 0 - 10^{-9} s: The pulsed laser beam is focused perpendicular to the material surface and penetrates via the skin effect. Within this thin surface layer, energy is absorbed by two main mechanisms: multiphoton absorption and inverse bremsstrahlung. At laser intensities under the ablation treshold, individual photons often lack sufficient energy to bridge the material's band gap, so linear absorption may not occur. At higher laser fluences, multiphoton absorption allows several photons to be absorbed simultaneously, enabling long wavelengths to excite the material. Inverse bremsstrahlung is physical phenomenon which occurs when a free electron absorbs a photon and then transfers that energy through collisions with neutral atoms or ions. Then it irradiates a continuous spectrum.

   Immediately upon pulse arrival and the beginning of absorption, the material heats rapidly at the rates of $10^{10}\frac{\mathrm{K}}{\mathrm{s}}$. The relatively long duration of a nanosecond pulse establishes a steep temperature gradient, causing heat to diffuse through the material.

2. 10^{-9} - 10^{-8} s: The target material begins to ablate, forming a plasma plume composed of atoms, ions, and free electrons from both the material and the ambient media. In the nanosecond regime, ablation proceeds via three mechanisms, which happen simultaneously [17]:

   - **evaporation**, during which the material undergoes successive first-order phase transitions up to the gas phase (see Figure 1.2).
   - **explosive boiling**, where localized superheating above the boiling point produces bubbles that rapidly grow and collapse, enlarging the ablation crater.
   - **phase explosion**, in which the superheated surface layer gets over the boiling point and is ejected in form of gas or liquid droplets due to the difference is pressure. vaporization and droplet ejection due to rapid pressure buildup.

   At this stage, the plasma plume reaches its peak temperature and undergoes rapid, symmetric expansion at speeds up to $2 \times 10^4 \ \frac{\mathrm{m}}{\mathrm{s}}$. This expansion creates a shock wave. In vacuum, the plume expands adiabatically. The laser pulse continues to deposit energy, further heating and ionizing the ablated material. This leads to plasma shielding, where the dense, ionized vapor absorbs and shields the incoming pulse, preventing it from reaching the sample surface.

The plasma now emits a strong continuous spectrum driven by inverse bremsstrahlung absorption and recombination processes. Ionic emission lines also appear against this background. In nanosecond-pulse excitation, the continuum is especially intense, and its intensity grows with the plasma temperature. The time evolution of spectra can be seen in Figure 1.10.

3. 10^{-8} - 10^{-6} s: After the laser pulse terminates, the plasma begins to cool. The plume still expands, but its growth is decelerated by interaction with the ambient medium. The plasma is in a quasi-stable state, behaving differently each time. The center of the crater remains hot while the edges cool. Molten material ejected as droplets from collapsing vapor bubbles solidifies around the crater rim, forming a molten collar. This can be seen in Figure 1.11. Within the crater, the steep temperature gradients during cooling can induce microcracks. Hydrodynamic fission occurs in later times [22].

   The spectral lines observed during this period originate from electronic transitions in the plasma. These include recombination of singly ionized atoms back to neutral atoms, as well as transitions from multiply ionized atoms to lower ionization states. Each transition releases energy, which is emitted as light. The energy of the emitted photon corresponds to the difference between the two energy levels $E = E_2 - E_1$, where E_2 is the higher energy level the atoms occupy and E_1 is the lower level.

4. 10^{-6} - 10^{-3} s: As the plasma cools further, emission lines from ions, atoms, and molecules emerge. The decelerating interface between the expanding plasma and the surrounding medium develops hydrodynamic Rayleigh–Taylor instabilities [23].

5. 10^{-6} - 10^{-3} s: Once the internal pressure of the plasma plume equilibrates with the surrounding atmosphere, its expansion stops. As all charged species recombine into neutral atoms, part of the ablated material is expelled into the surroundings, while the remainder falls back onto the sample under gravity, forming a deposited debris.

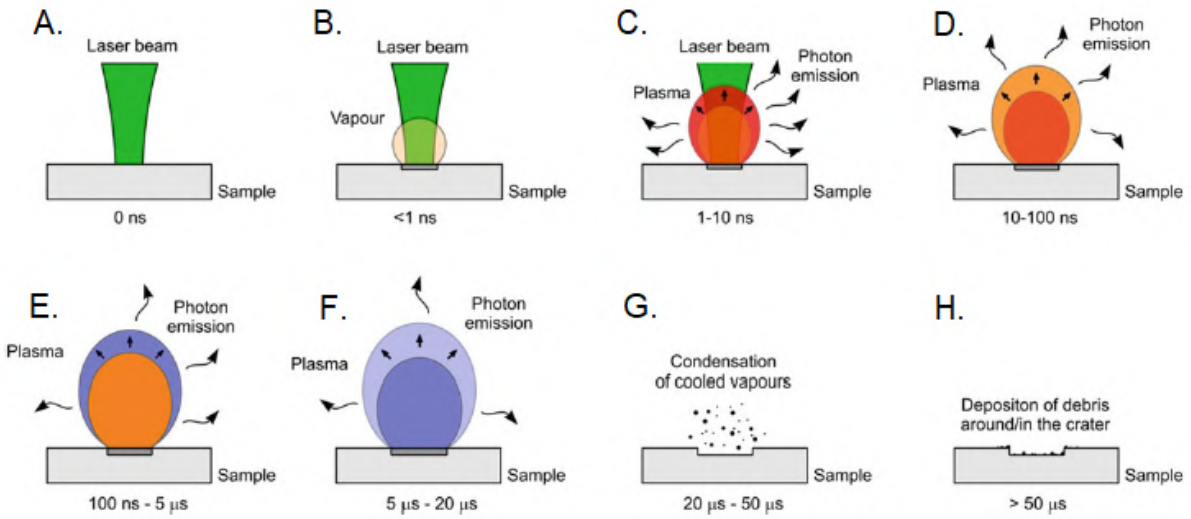

Figure 1.9: Schematic of plasma development in space and time under excitation by a 5–10 ns laser. Time labels are only approximate, and the number of arrows indicates the relative emission intensity. The steps are labeled A to H. Taken from [15].

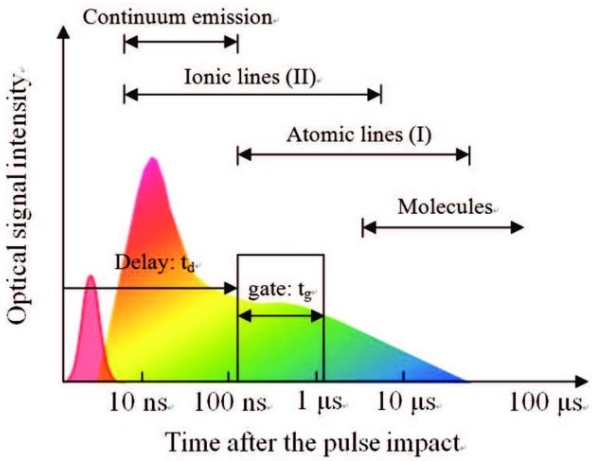

Figure 1.10: Time-resolved plasma emission with corresponding spectral characterization. The first peak (pink) corresponds to the pulsed laser. The maxima of plasma emission corresponds to a high continuum. Taken from [24].

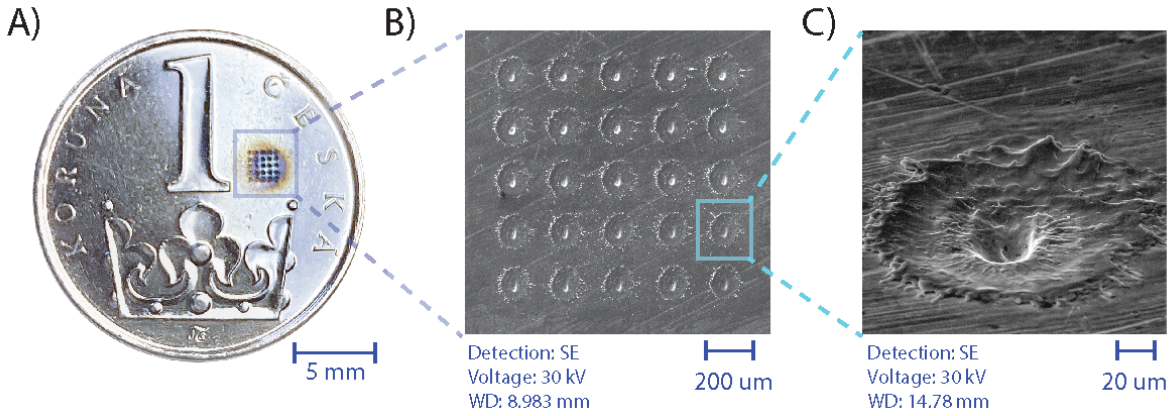

Figure 1.11: Images of different scales showing ablation damage: (A) the sample—a coin, (B) laser-ablated craters on the coin surface, (C) a single crater viewed at a 45° angle. Images (B) and (C) were acquired using a Tescan Vega scanning electron microscope.

Femtosecond laser

A femtosecond pulse deposits its entire energy onto the material surface in an ultra-short moment, preventing the formation of a shielding plasma layer. Only the low-mass free electrons can respond to the extreme intensities (above $10^{13}\,\mathrm{W\,cm^{-2}}$), generating an electron cloud with a strong electric field, that directly ionizes the target. Ablation is dominated by Coulomb explosion, in which the electrostatic repulsion between highly charged particles on the surface and the neutral bulk rapidly ejects material. Energy transfer from electrons to ions occurs over a few to tens of picoseconds, comparable to the time the material needs to conduct heat. The femtosecond pulse and Coulomb explosion are complete before significant heat conduction can occur. As a result, thermal damage is minimized, producing a smooth, well-defined crater with little impact on surrounding structures. The plasma produced expands more quickly, remains cooler, and has higher density than in nanosecond-pulse ablation [25, 26, 27].

1.1.5. Local thermodynamic equilibrium

Accurate modeling of laser-induced plasma (LIP) is crucial for quantitative analysis. A fully kinetic description captures all microscopic processes but is impractical due to the large number of parameters varying in space and time. A thermodynamic approach, in contrast, requires only three macroscopic parameters: electron temperature T_e, electron density n_e, and total particle density, all of which can be experimentally measured. Thermodynamic equilibrium means that a single temperature describes all forms of energy. In LIP, true global equilibrium never exists because temperature and density change rapidly in both space and time. However, *local* thermodynamic equilibrium (LTE) can be assumed within small regions of the plasma if certain conditions are met [28, 29]:

- **Collision-dominated plasma:** The rate of Coulomb collisions must greatly exceed the rate of radiative processes. Collisional energy exchange among electrons enforces a Maxwellian distribution, while radiative losses must be small enough to not disrupt this equilibrium.
- **Single-temperature description:** All plasma properties—excited-state populations (via the Boltzmann distribution), particle kinetic energies, and ionization balance—can be characterized by the same temperature T_e.
- **Minimum electron density:** The McWhirter criterion ensures sufficient amount of particles for collision processes:

$$n_e \geq 1.6 \cdot 10^{12} \sqrt{T} (\Delta E)^3, \tag{1.11}$$

  where ΔE (eV) is the energy gap between two atomic levels.
- **Optically thin plasma:** Radiation must escape the plasma without significant re-absorption, so that radiative energy losses do not disrupt the local thermal balance.

Laser-induced plasma in LIBS does not maintain LTE throughout its evolution, particularly during the first 100 ns after ablation [30].

1.2. Laser-Induced Breakdown Spectroscopy

Laser-Induced Breakdown Spectroscopy (LIBS) is a type of atomic emission spectroscopy. A short, energetic laser pulse is focused onto a sample. The irradiance (in the GW/cm^2 orders) ablates a small volume of material and forms a laser-induced plasma. As the plasma cools, the excited atoms/ions emit their element-specific spectral lines. A fast, gated spectrometer records this light. Because the laser itself handles sampling and excitation in one step, LIBS delivers rapid analysis.

Two years after T. H. Maiman built the first solid-state laser in 1960, F. Brech and L. Cross performed the first laser-spark emission experiment, now regarded as the birth of Laser-Induced Breakdown Spectroscopy (LIBS). As laser sources, timing electronics and computerised data processing matured in the late 1980s, the technique evolved from a niche laboratory tool into a widely studied method that fuels rapid advances across many

fields. On Mars, NASA's Curiosity and Perseverance rovers use the ChemCam and SuperCam instruments to probe rock chemistry from several metres away. In biomedicine, LIBS supports trace-element mapping, nanoparticle tracking, and early studies on cancer diagnostics. Cultural-heritage specialists employ it to identify pigments and paint layers while removing only microscopic amounts of material. These cases represent only a fraction of the expanding portfolio of LIBS applications reported each year [15, 31]. LIBS delivers analyses across solids, liquids, gases, and aerosols. Its advantage is also the detection of light elements such as lithium. It can operate in situ, over large distances, or under controlled laboratory conditions with typical limits of detection in the low-ppm range (about 1–50 ppm for most elements in solids). Its disadvantage is that after the sample gets damaged during the measurement, however, only on a microscopic level.

1.2.1. LIBS components

A typical LIBS system consists of a pulsed laser synchronized with a gated spectrometer—commonly of the Czerny–Turner, Echelle, or Paschen–Runge type—which collects spectra at very short exposure times, typically hundreds of nanoseconds after plasma formation. The laser is focused on a sample, generating plasma on its surface. The emitted light from the plasma is collected by optical components and focused into a multimode optical fiber, which guides the signal to the spectrometer and detection unit. The system also includes an XYZ translation stage, enabling depth profiling as well as 2D mapping, resulting in hyperspectral images. The system can be seen in Figure 1.12.

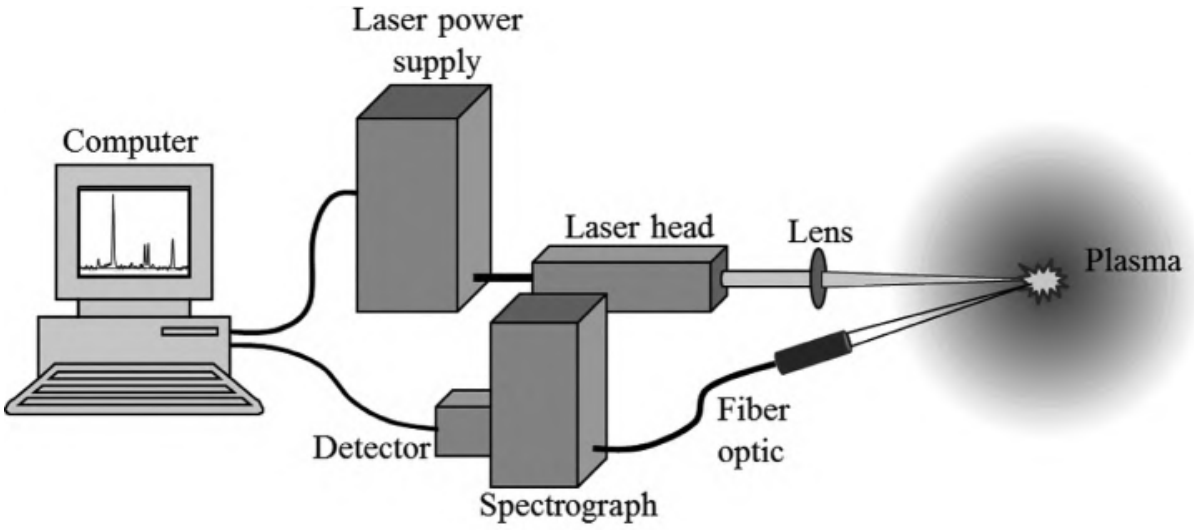

Figure 1.12: Typical LIBS setup, taken from [17]

1.2.2. Observed spectra

The origin of spectra was already described in Chapter 1.1.4. Here, I would like to focus on the shape of spectra and how to distinguish individual elements.

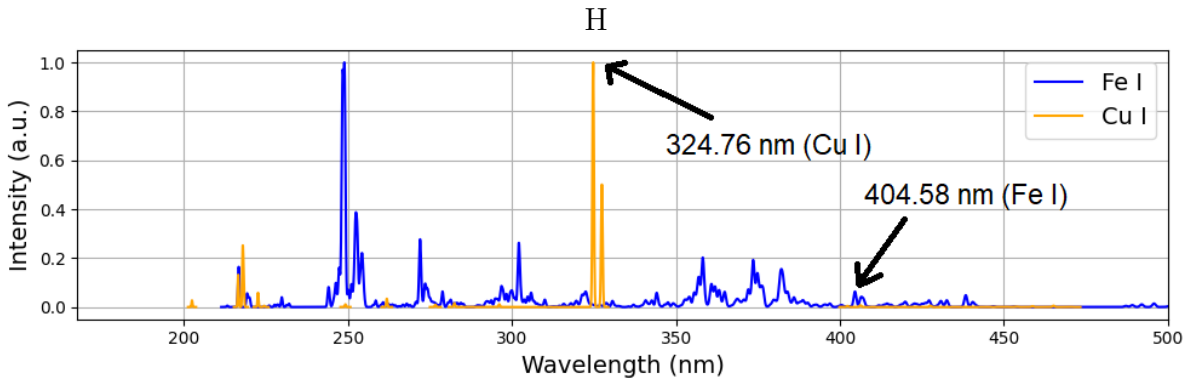

Figure 1.13: Simulated atomic spectra of copper and iron with their typical spectral peaks, generated from [32] at 1×10^{17} cm^{-3}.

Multiple mechanisms can broaden the spectral line. Because of the Heisenberg principle $\Delta E \leq h \cdot \Delta t$, where the spectrum is measured in a finite amount of time, it can not be certain which exact energy is measured. The spectral line broadens. The spectra can broaden in a certain shape. The first group of mechanisms broadens into a Gaussian profile (G). Second into Lorentzian profile (L). In general, we observe spectra corresponding to a convolution of those two profiles called the Voigt function

$$V = L * G. \tag{1.12}$$

To identify which spectral peaks correspond to specific elements, the measured LIBS spectra are compared to reference databases containing simulated atomic and ionic emission lines. In samples dominated by a single element, peak identification is usually straightforward. However, many spectral lines are shared between elements, making manual analysis more difficult. Fortunately, some lines are unique to individual elements and serve as reliable identifiers. For more complex samples containing a wider range of elements, statistical methods such as principal component analysis (PCA) or machine learning algorithms can assist in determining the composition. In Figure 1.13, the simulated atomic and ion spectra of iron and copper can be seen.

The complete chemical and physical environment in which the analyzed target element or compound resides is called the matrix, and its influence on the analytical signal is known as the matrix effect. In quantitative LIBS (and many other spectrochemical methods), matrix effects can significantly impact measurement accuracy. We distinguish two main types:

- **Chemical matrix effects** originate from the material's composition. Different chemical environments alter processes such as particle formation, vaporization efficiency, plasma temperature, and electron density. For example, a steel alloy rich in carbon will generate a plasma with different chemistry (and thus different emission intensities) compared to a low-carbon steel, even when the concentration of a trace metal is identical.
- **Physical matrix effects** originate from mechanical and thermal properties such as hardness, thermal conductivity, reflectivity, porosity, and surface roughness. These factors determine how much mass is ablated per laser pulse and how efficiently energy couples into the sample. Under identical laser parameters, a hard ceramic

will produce a smaller crater and less ablated mass than a softer polymer, leading to systematically lower emission signals.

Together, chemical and physical matrix effects can produce non-linear calibration curves and element-to-element interferences. Common ways to reduce these effects include using reference materials with a similar composition, normalizing the signal to an internal standard (known concentration of an element in the sample), or using data analysis methods like the already mentioned PCA to correct for matrix differences [28].

1.3. Optical Interferometry for Plasma Diagnostics

Plasma diagnostics via interferometry enables noninvasive, high-resolution measurement of the optical phase shift by plasma refractive index changes. From that data, we can derive electron density. Since the plasma ω_p is in the range of single units of THz as stated in chapter 1.1.3, it is possible to probe with a laser of visible wavelength (which has the frequency of 500 THz). In this chapter, we first discuss the fundamental conditions required for interference, describe the Mach-Zehnder interferometer to measure phase-shift in plasma, and then develop the mathematical description used to extract refractive index information from interference fringes to calculate the electron density of plasma. [33, 34]

1.3.1. Fundamentals of interference

Interference is a phenomenon describing the interaction of waves. Conditions for the interference of two waves are as follows: [34]

- **Superposition Principle:** The linear combination of complex wave functions must also be a valid solution. In practice, this requires that the interfering beams propagate in the same direction so that their wavefronts overlap.
- **Coherence:**
  - *Temporal Coherence:* The waves must be monochromatic (i.e. having the same wavelength) so that their phase remains nearly constant over time within the coherence interval. For interference to be observed, the optical path difference (OPD) between the two arms must be less than the coherence length of the light source.
  - *Spatial Coherence:* The beam, being composed of individual waves, must have a uniform phase across its wavefront. This is typically achieved by collimating the light.
- **Polarization:** The electric field vectors of the two waves should be oriented in the same plane. If they are orthogonal, no interference will be observed.

If these conditions are not fully met, for example, if the beams are only partially coherent or partially polarized, the resulting interference pattern will exhibit reduced fringe visibility and contrast, and in extreme cases, the interference fringes may vanish entirely. Sources meeting these conditions operate in the same mode. A laser is a device capable of producing such waves.

In optical interferometry, physical detectors measure intensity rather than the instantaneous electric field. The intensity I is defined as the time average of the square of the electric field:

$$I \propto \langle |E(t)| \rangle = \langle E(t)E^*(t) \rangle, \tag{1.13}$$

where the angle brackets $\langle \cdot \rangle$ denote a time average over many optical cycles. When two beams interfere, their complex electric fields (assuming the same polarization and frequency) are given by:

$$E_1(t) = A_1 e^{i\omega t - i\phi_1} \quad \text{and} \quad E_2(t) = A_2 e^{i\omega t - i\phi_2}, \tag{1.14}$$

where their complex amplitudes are

$$A_1 = |A_1| e^{-i\phi_1} \quad \text{and} \quad A_2 = |A_2| e^{-i\phi_2}, \tag{1.15}$$

and their total complex field is

$$E(t) = E_1(t) + E_2(t). \tag{1.16}$$

Expanding the intensity using time averaging gives

$$I = \frac{1}{2}\Big(|A_1|^2 + |A_2|^2 + A_1^* A_2 + A_1 A_2^* \Big). \tag{1.17}$$

Here, we define $I_1 = \frac{1}{2}|A_1|^2$ and $I_2 = \frac{1}{2}|A_2|^2$. With $\Delta\phi = \phi_1 - \phi_2$, we obtain the final expression:

$$I = I_1 + I_2 + 2\sqrt{I_1 I_2}\cos(\Delta\phi). \tag{1.18}$$

The term $2\sqrt{I_1 I_2}\cos(\Delta\phi)$ represents the interference contribution (i.e. interference term) which includes the phase from the complex amplitude. When $\Delta\phi = 2\pi m$ (with m an integer), $\cos(\Delta\phi) = 1$ and the interference is constructive, yielding maximum intensity; conversely, when $\Delta\phi = (2m+1)\pi$, $\cos(\Delta\phi) = -1$ and the interference is destructive, leading to minimum intensity.

Interference can be measured by various interferometric techniques. In spatial interferometry, which is used in this thesis, the intensity $I(x, y, t = t_0)$ is observed at a single time t_0 on a two-dimensional detector. Interference results in the formation of an interference pattern (i.e. interferogram) that can be seen in the Figure 1.14.

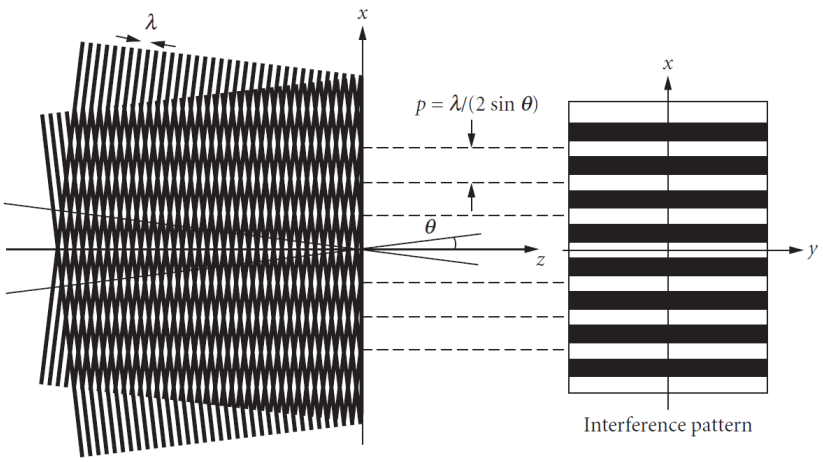

Figure 1.14: Spatial interference of two planar waves under an angle θ forms line fringes. The greater the angle, the more fringes appear. Taken from [34].

1.3.2. Mach-Zehnder interferometry

In plasma diagnostics, the Mach–Zehnder interferometer (MZI) is widely employed to translate small changes in the plasma refractive index into measurable shifts in the interference pattern, thereby enabling the determination of local electron density [35]. In this setup (seen in the Figure 1.15), a collimated laser beam with a single frequency is divided into two paths by a 50:50 beam splitter. One beam (the sample beam) passes through the plasma while the other (the reference beam) travels an identical optical path in the absence of plasma. The two beams are then recombined at a second 50:50 beam splitter. Two interference patterns are created, where one is contrast-inverted to the other because of a phase shift of π on the last reflection [33, 34].

A key concept in interferometry is the optical path length (OPL), which is defined by the integral

$$OPL = \int_S^P N_O(x)\, dx, \tag{1.19}$$

where $N_O(x$ is the refractive index along the beam path dx, and the integration is carried out along the path from the source S to the observation point P. The progress of N_O can be seen in the Figure 1.16.

The formation of interference fringes follows directly from the principles of optical interference. The equation 1.18 shows that the resultant intensity depends on the individual intensities as well as on the phase difference between the two beams. In the MZI, the phase difference arises because the plasma introduces a change in the refractive index along the sample arm, altering its optical path length relative to the reference arm. The difference between the OPLs (i.e., the optical path difference is given by

$$OPD = OPL_2 - OPL_1. \tag{1.20}$$

This OPD leads to a phase shift between the two beams, described by

$$\Delta\Phi = 2\pi \frac{OPD}{\lambda}. \tag{1.21}$$

When the plasma is introduced into one arm, its refractive index change alters the OPL, resulting in a phase shift $\Delta\Phi$ that appears as a displacement in the interference fringes. A key feature of the MZI is that the fringe pattern can be manipulated by adjusting the mirror inclinations. By introducing a slight tilt, the recombining beams intersect at a small angle, leading to a denser fringe pattern with thinner, closely spaced lines. This increased fringe density improves measurement precision because even a small phase shift causes a noticeable movement across multiple fringes. In effect, the high fringe density acts like an increased sampling rate of the phase front (as per the Nyquist theorem, the higher the sampling frequency, the more resolution in finer details we find). A denser fringe pattern provides a more sensitive and precise determination of the phase-changing phenomena [8].

Overall the Mach–Zehnder configuration has several advantages:

- **Flexible Configuration:** The spatially separated beams allow easy insertion of the plasma cell and isolation from environmental disturbances.

- **Single-pass Measurement:** The sample beam passes through the plasma only once, minimizing cumulative phase errors.
- **Fringe Control:** The ability to adjust mirror inclinations permits tailoring the fringe density to achieve higher sensitivity.
- **Versatility:** By covering the reference arm, system can image shadowgraphs.

and challenges:

- **Alignment Sensitivity:** Precise alignment of the beam splitters and mirrors is critical; any misalignment can reduce fringe visibility and introduce measurement errors.
- **Environmental Isolation:** Although the design helps mitigate disturbances, additional measures (vibration isolation, air flow control) are necessary for high-precision measurements.

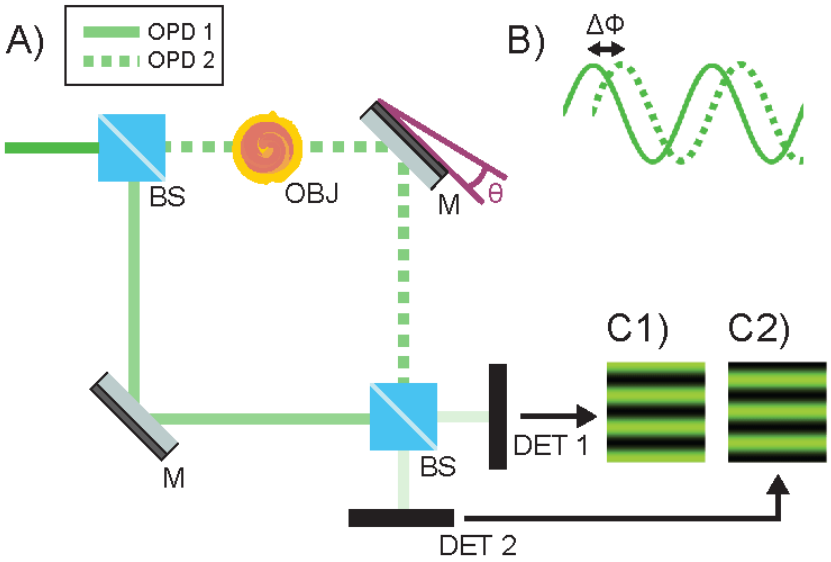

Figure 1.15: A) Mach-Zhender interferometer with 50:50 beam splitters (BS), adjustable mirrors (M) where one is tilted by angle θ, detectors (DET 1 and DET 2) and phase object (OBJ). B) is a scheme of interfering waves shifted by $\Delta\Phi$. C1) and C2) are complementary images of fringes (without the object) formed from two plane waves shifted by π. Redrawn from [36].

1.3.3. Phase extraction

The most straightforward method to extract the phase from the interferogram is phase referencing. Two interferograms are taken one serving as a reference with undisturbed interference fringes, the other is the phase-shift measurement. Φ_O is the phase shift made without the observed object. Φ is the phase shift image [37, 38, 39]:

$$\Phi = \Phi_O + \Delta\Phi \tag{1.22}$$

$$\Phi_O = \int_S^P N_O(y,z)\,dx \tag{1.23}$$

$$\Delta\Phi(y,z) = \int_S^P N_{ambient}(x) - N_O(x)\,dx = \int_S^P \Delta N_O(x)\,dx, \tag{1.24}$$

where $N_{ambient}(x)$ is the ambient index of refraction the reference arm goes through, and $\Delta N_O(x)$ is the resulting change in index of refraction.

A single interferometric image is essentially a measurement of OPLs. To retrieve the phase shift, one must perform the Fourier transform to obtain phase data. And subtract the phase of two images from a reference image in the measurement [40].

The 2D Fourier transform $F(u,v)$ is a mathematical analytical tool that can decompose a signal into its individual harmonic components. It is a linear operation in the form:

$$\mathcal{F}\{I(x,y)\} = \iint I(x,y)\cdot e^{-i2\pi(xu+yv)}\,dx\,dy, \tag{1.25}$$

where $u = \omega\cdot\cos\alpha$ and $v = \omega\cdot\sin\alpha$ are spatial frequencies which are orthogonal to each other, $f(x,y)$ is the 2-D image with coordinates x and y, and the complex term $e^{-i2\pi(xu+yv)}$ represents the phase shift of waves in space. The phase is extracted by:

$$\Phi = arctg\left(\frac{Im(A)}{Re(A)}\right), \tag{1.26}$$

where

$$Re(FFT) = A\cdot cos(\Phi) \quad \text{and} \quad Im(FFT) = A\cdot sin(\Phi). \tag{1.27}$$

In numerical computations, the continuous Fourier transform is replaced by its discrete counterpart, the Discrete Fourier Transform (DFT). To perform this efficiently, the two-dimensional Fast Fourier Transform (FFT2) algorithm is commonly used.

To extract the phase information from an interferogram, a 2D Fourier transform of the fringe pattern is applied. In the frequency domain, the spectrum typically contains a central zero-order component and two symmetric first-order diffraction terms. One of the first diffraction orders is isolated using a frequency filter, while all other components are suppressed. This filtered component contains the relevant phase information (as seen in the interference terms in Chapter 1.3.1) and can be shifted back to the origin before applying the inverse Fourier transform. The result is a complex field from which the phase distribution can be directly calculated.

A reference interferogram is first recorded under known conditions, followed by a second one taken after introducing a phase-altering element. By comparing the two, the measurement is effectively referenced to a known baseline, isolating the phase shift caused solely by the object [40].

1.3.4. Plasma tomography

Tomography is the process of reconstructing the internal structure of an object from its projections. A projection is obtained by integrating a measurable optical property of the object with a penetrating wave. In plasma interferometry, such a property is the change in OPL due to refractive index variations leading to a phase shift $\Delta\Phi$. Figure 1.16 illustrates how a single pass of the wave through the interferometer's object arm at time t_0 produces an optical path length OPL. This OPL is integrated along the beam path from the source to the sensor pixel. Such integration produces a one-dimensional projection of the three-dimensional plasma structure, as shown in Figure 1.17. A tomographic slice, by contrast, is a cross-sectional view of an object (in the XY plane). A geometry of such a slice can be seen in the Figure 1.18. It is reconstructed by a mathematical algorithm from an input of projections made on a pixel array. Various integral transformations can be used, most commonly the Radon transform and in optics Abel transform. It is good to mention that, as there is only a limited number of measurements, the reconstructed function is not continuous and is only an approximation at best to the exact distribution [37, 41].

The goal in plasma tomography is to use the spatially resolved interferometric measurement $I(x, y, t = t_0)$ to determine the full three-dimensional refractive index distribution $N_O(x, y, z, t = t_0)$. By combining the projection data, it is possible to reconstruct multiple tomographic slices which, when assembled, reveal the plasma's internal structure.

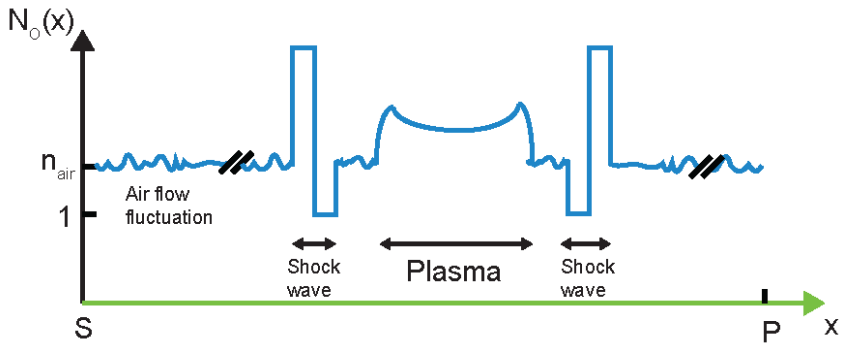

Figure 1.16: Single pass of a probing wave through the interferometer's object arm at time t_0. The integral of this path is equal to OPL.

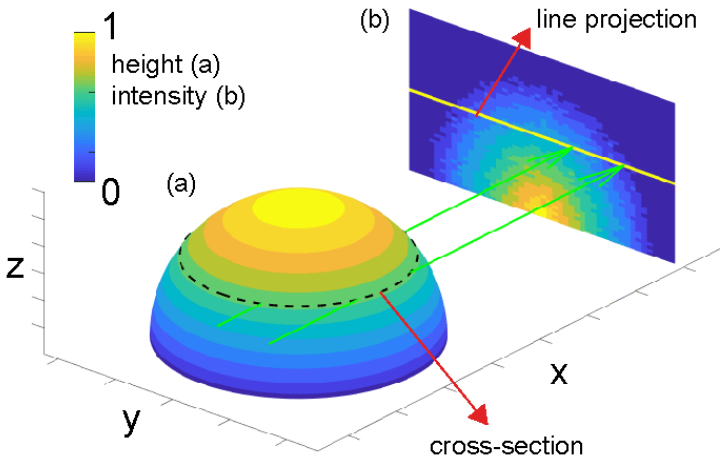

Figure 1.17: Graphical description of tomography. (a) The axisymmetric object is integrated along lines parallel to the x-axis, and a line-of-sight projection is obtained from the cross-section area highlighted by the dashed line. The line of sight of individual waves is illustrated by the green arrows. (b) Projection on the XZ-plane, which contains noise due to air and other fluctuations. The green arrows point to a line of projection, which highlights the data used for tomographic slice reconstruction. Figure is recreated in MATLAB from inspiration [42] and edited.

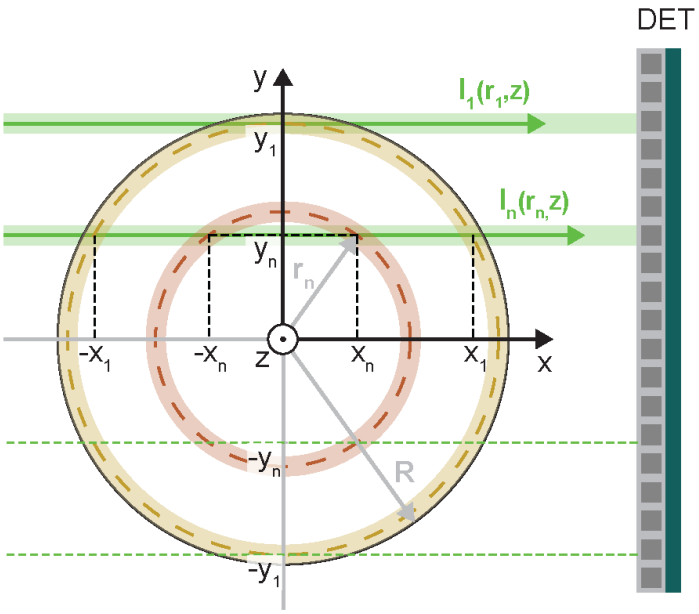

Figure 1.18: Reconstructed slice (section at constant coordinate z) of an ideally symmetric object from Abel transform. It is probed by beams depicting (green) intensity I_n on detector (DET) at radius r_n and coordinate y_n. The beam I_n integrates over multiple layers (yellow and red discs) of constant value at points $-x_1, -x_n, x_n$ and x_1. The same intensity is recorded at the opposite coordinates $-y_1$ for $I_1(r_1, z)$ and $-y_n$ for $I_n(r_n, z)$. The object is bounded by distance R. Redrawn and edited from [43].

In many tomographic applications, object projections are acquired from multiple directions because the acquisition time is sufficiently slow to resolve each projection individually. In laser-induced plasma, however, the plasma's lifetime is very short, making it

challenging to directly measure its three-dimensional properties from a single ablation event. While the most accurate method involves using an array of cameras to capture images simultaneously from multiple viewing angles, this technique is both expensive and complex to implement [44]. The process of obtaining data can be simplified by introducing assumptions. One assumption is that the plasma maintains the same shape and internal distribution at identical time acquisition in different ablation events. This allows multiple plasma ablations to be recorded over a set of angles while rotating the sample stage [45]. Furthermore, by making a geometrical assumption about the plasma, the complexity of data collection can be greatly reduced, enabling reconstruction from a single projection measurement.

Abel transform assumes cylindrical symmetry of an object. It can be viewed as a special case of the Radon transform [41]. A transformation from Cartesian coordinates to cylindrical coordinates is denoted as:

$$N_O(x, y, z) = N_O(r, z), \tag{1.28}$$

where $r^2 = x^2 + y^2$ is the radius from the axis of symmetry. This means that the internal density structure is nested on circular surfaces.

For most applications, a single pulse LIBS analysis is used, so this transform may be sufficient in most cases. In the other cases, when two or three pulse LIBS analysis is used, the plasma is asymmetric [45]. Subsequently, when the ablation happens at the interface of two materials, the plasma electron density is not homogeneous [16]. The Abel transform accuracy is therefore limited to symmetric and isotropic cases of plasma.

Abel transform is defined as a radial function $f(r)$ integrated over a curve perpendicular to the axis of symmetry, giving projection $p(y) = F(y)$ [46]:

$$p(y) = F(y) = \int_0^{\sqrt{R^2-r^2}} f(r)dx. \tag{1.29}$$

To connect interferometric measurements with the Abel transform, the specific functions are assigned physical meanings:

$$F(y) = \Delta\phi(y), \quad \text{and} \quad f(r) = \Delta N_0(r), \tag{1.30}$$

where $N(r)$ is the refraction index of the reference medium. The substitution to cylindrical coordinates yields:

$$F(y) = 2\int_y^R \frac{f(r)r}{\sqrt{y^2 - r^2}}dr, \tag{1.31}$$

when $0 < r < R$. Where y is the distance of the curve from the axis of symmetry, $f(r)$ is the radial refractive index at the distance r, and R is the edge of the region. Outside of this region $f(r \geq R) = 0$.

The inverse problem is to reconstruct the three-dimensional object from the two-dimensional projection. In this case, the goal is to derive the radial refractive index profile from a measured phase shift in interferometric data. To achieve this, the inverse Abel transform is

employed, which is an indirect method used to recover the index of refraction at each radial position r. The solution to the Abel inversion equation is given by:

$$f(r) = -\frac{1}{\pi}\int_{-y}^{R}\frac{dF(y)}{dy}\frac{dy}{\sqrt{y^2-r^2}}. \tag{1.32}$$

Abel inversion does not have any analytical solution, so numerical methods must be implemented. However, three major issues with finding the solution arise: [47]

- The boundary R is not clearly defined as plasma decays continuously outwards
- The phase shift $\Delta\phi(y)$ is susceptible to noise, and taking its derivative $dF(y)/dy$ amplifies this noise. At derivative $dF(y)/dy$, if we divide a noisy signal $dF(y)$ by a small step dy, the noise of the data gets amplified.
- In theory a singularity $\sqrt{y^2-r^2}=0$ of the kernel at the axis of symmetry happens as $y \to r$. However, when we measure discrete data by a sensor, this never happens. Instead, the square root in $\frac{dy}{\sqrt{y^2-r^2}}$ yields a small number, which then massively amplifies the noise near the center of the axis of symmetry. This perturbation can affect the whole solution for Abel inversion.

Any noise present in the measured phase $\Phi(y,z)$ becomes amplified during differentiation, potentially leading to unstable or nonphysical results. These challenges require careful numerical treatment, including the use of smoothing or regularization techniques, to reliably reconstruct the radial refractive index.

1.3.5. Practical considerations in measuring plasma electron density

In most interferometric studies of laser-produced plasmas (LPP), it is commonly assumed that only free electrons contribute to the refractive index. However, bound electrons can also influence fringe shifts—often in the opposite direction—especially if the probe laser wavelength overlaps with absorption resonances. To minimize this effect, the probe wavelength should be selected far from any such resonances. Accurate electron density measurement also requires high temporal resolution, as LPPs evolve rapidly. If the probe pulse duration is too long, electron density gradients during the exposure can blur the fringes. To preserve fringe visibility, short-pulsed probe lasers are preferred [8].

The sensitivity of interferometric measurements depends on both the configuration and the wavelength of the probe laser. Shorter wavelengths improve both spatial resolution and sensitivity [48].

Interferometric images exhibit a clear hemispherical wavefront. At the shock front, interference fringes shift toward the sample surface, meaning there was a local increase in refractive index caused by compressed air and ablated particles. Behind this front—inside the sphere defined by the shock leading edge, the fringes shift in the opposite direction (toward positive z), so the refractive index is $n < 1$. This reduction in n comes from both free-electron dispersion and from rarefaction, i.e. a local drop in gas density behind

the shock front. Because these fringe displacements are symmetric about the z-axis, Abel inversion can be applied to reconstruct the spatial refractive index profile [28].

Beyond these physical limits, practical challenges such as beam deflection in steep density gradients, inverse bremsstrahlung absorption, and strong plasma self-emission can degrade fringe contrast and obscure the interferogram. These issues emphasize the importance of careful probe beam selection and sufficient intensity to overcome both attenuation and optical noise.

2. Experimental part

The main goal in the experimental part was to use a Mach-Zehnder interferometer to measure the evolution of electron density. The experimental part describes the steps taken to build and optimize a Mach-Zehnder Interferometer in chapter 2.2. Then, describing the process of measuring steel samples and one copper sample with pump lasers 1064 and novel 2090 nm in chapter 2.3. The raw data interpretation is resolved in chapter 2.4. The shock wave measurement in chapter 2.5. The data processing method is later described in great detail in chapter 2.6. Finally, the results are presented in chapter 2.7.

2.1. Used devices and its parameters

2.1.1. ICCD

An intensified CCD camera is used to capture the rapidly evolving plasma interferograms. It uses an external electrical signal trigger to synchronize with the laser, which induces plasma. It can be cooled down to relatively low temperatures to minimize dark current and thermal noise. Also, a voltage can be applied to a photon amplifier, which works on the photoelectric effect. This intensifies the incoming signal. Both of these benefits are leading to good signal-to-noise ratio images. It uses Andor Solis software to communicate with the device and retrieve measured data. The camera parameters are in the Table 2.1.

Table 2.1: Specifications of the Istar 720 series 18-03

Parameter	**Specification**
Device	Istar 720 series 18-03
Active area of CCD	18 × 6.7 mm
Pixel size	26 × 26 µm
Resolution	1024 × 256 px
Spectral range	199.25 – 900 nm
Minimum optical gate width	5 ns
Minimum readout time	4.4 s
Thermo-Electric cooling max	–25°C
Gain (voltage)	0 – 255
Bit depth	16

2.1.2. Echelle spectrometer

This spectrometer uses the same camera as the one for imaging plasma: Istar 720 series 18-03. It is further modified to input an optical fiber carrying the plasma spectra information. Spectral lines are captured by the CCD chip. The intensity is fitted with a calibrated function and returned as spectra.

2.1.3. Probing laser diode

The laser probing plasma in the ambient atmosphere needs to be chosen carefully, because the cooling plasma could absorb its wavelength, which could degrade the image data.

A green laser at 532 nm avoids all the important spectral lines for hydrogen, oxygen, nitrogen, carbon, iron, and copper. The laser wavelength is also limited by the plasma frequency, which is in the THz region for electron densities created in LIBS. It is a very cheap and compact device. The laser diode parameters are in the Table 2.2. The output beam needed to be expanded, for which the Thorlabs 5X Mid-IR Galilean Beam Expander was used, expanding to 5x magnification. It has a collimation adjustment ring (further talked about in Chapter 2.2) and a thread to mount the laser.

Table 2.2: Specifications of Thorlabs CPS532 Laser Module

Model	Thorlabs CPS532 Collimated Laser-Diode-Pumped DPSS Laser Module
Type	Continuous
Wavelength	532 nm
Output Power	4.5 mW
Beam Shape	Round Beam

2.1.4. Near infrared pump laser

This is the first of the pump lasers used to produce plasma. This laser with the Nd:YAG active medium is typical for LIBS applications. It has a very high maximum energy of 400 mJ, however has a fairly slow pulse repetition rate of 10 Hz. It can stay idle for longer periods of time. The laser parameters are in the Table 2.3.

It has straightforward and automated controls. The repetition rate and energy is controlled by the LIBS Navigator program software created at Brno, CEITEC. This software also enables to definition of the number of pulses, the delay time for data acquisition, and defining the scanning map area on the live view of the sample by controlling an XYZ motorized stage.

Table 2.3: Specifications of Quantel Brilliant B Pulsed Nd: YAG Laser

Model	Quantel Brilliant B
Laser Type	Pulsed Nd: YAG
Wavelength	1064 nm
Output Beam Diameter	8 mm
Energy (Min - Max)	10 - 400 mJ
Pulse Duration	5 ns
Beam Profile	Gaussian
Maximum Repetition Rate	10 Hz

2.1.5. Far infrared pump laser

This pulsed laser is unique with its wavelength at 2090 nm. To our knowledge, no such laser has been used for LIBS applications. It has a fast pulse repetition rate, making it appealing for scanning large sample areas. Thanks to the small output beam diameter, it can be focused to a spot size of the order of tens of micrometers.

The disadvantage is the controlling system. This device is a prototype, which has manual controls for the voltage applied to the Pockels cell and the current controlling the optical

pumping for the active medium. It is not suitable for slow applications. It should not be in an idle state for more than two minutes to ensure its longevity. The laser parameters are in the Table 2.4.

Table 2.4: Specifications of HiLASE Perla 2000 Micro (Ho: YAG) Laser

Model	HiLASE Perla 2000 Micro
Laser Type	Pulsed Ho: YAG
Wavelength	2090 nm
Output Beam Diameter	4 mm
Energy (Min - Max)	1.3–4.7 mJ
Pulse Duration	4–4.1 ns
Beam Profile	Gaussian
Maximum Repetition Rate	20 - 1000 Hz

2.2. Construction of the measuring setup

To measure the spatial and temporal behavior of the plasma, I constructed a Mach–Zehnder interferometer (MZI) as a complementary diagnostic tool to the conventional spectral methods used in LIBS. Plasma image can be seen in Figure 2.1.

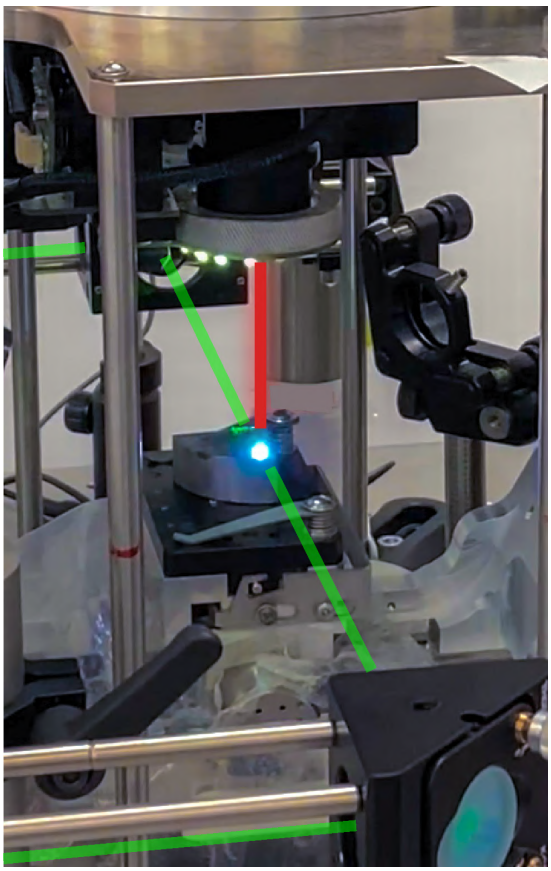

Figure 2.1: Laser induced plasma on a steel sample. Green lines indicate probe laser, red indicates pulsed laser.

Since a large laser system (2090 nm) was scheduled to be installed on the same optical table during the time frame of this thesis, the design of the Mach–Zehnder interferometer

had to be carefully planned to avoid any collision with the future pulsed laser beam path and other optical constructions. The size of the incoming system significantly limited available space, making thoughtful layout and positioning essential.

Initially, I constructed the Mach–Zehnder interferometer without significant mechanical constraints, which proved impractical. Fine alignment was difficult to maintain, and even minor adjustments often resulted in the loss of interference. It became evident that the system needed to remain reliably aligned over time and not be prone to misalignment from small disturbances.

To address these challenges, I opted for a cage system construction. This ensured that all optical components remained fixed in equidistant, collinear positions, allowing the beam path to stay consistently aligned. However, this approach could only be applied to three sides of the interferometer's arms, as the objective arm containing the plasma plume had to remain unobstructed. The key requirements for the resulting setup were the presence of clearly visible interference fringes across the entire beam profile and the ability to return to the system after a longer period (in days or weeks) and still observe stable interference without major realignment. To enhance overall stability, as many mechanical degrees of freedom as possible were eliminated. Heavy and rigid column holders were used to reduce sensitivity to vibrations or unintentional contact. The final setup can be seen as a scheme in Figure 2.2 and the real form in Figures 2.3 and 2.4.

Maintaining alignment was particularly challenging due to the characteristics of the probing laser used. The laser likely exhibited poor spatial coherence, possibly resulting from a broad spectral linewidth, which led to a short coherence length. As a result, interference occurred only over a limited optical path difference. Additionally, the beam exhibited non-uniform illumination, and slight divergence (or convergence) introduced by the beam expander made the system more susceptible to loss of interference. The divergence was needed to fully illuminate the plasma area and was chosen as an optimal ratio between area illumination and resulting intensity on a camera. Despite these limitations, once the new design was properly aligned, it proved effective. The alignment remained stable over time, with only minor changes observed in the orientation of the interference fringes, likely caused by thermal expansion of the mounting materials.

Another Galilean beam expander was implemented after the Mach–Zehnder interferometer, this time to magnify the interferogram and enable the resolution of finer spatial details. This design was selected for its compactness, resistance to in-air focal points (which can trigger unwanted plasma formation under high-power pulsed probing lasers), and the fact that it produces a non-inverted output beam. The expander consists of a concave lens (CC) to diverge the beam, followed by a convex lens (CX) to recollimate it. The nominal magnification factor is given by the ratio of their focal lengths

$$M_{nominal} = \frac{|f_{\mathrm{CX}}|}{|f_{\mathrm{CC}}|}. \tag{2.1}$$

Since the CX lens is not proportionally scaled in diameter with the magnification, the expanded beam is partially cropped due to the limited aperture size of the lens. In a

Galilean configuration, where $f_{\mathrm{CC}} < 0$, and laser divergence correction Δ is introduced, the spacing between the two lenses is given by the equation:

$$d = f_{\mathrm{CX}} + f_{\mathrm{CC}} \pm \Delta. \tag{2.2}$$

A focal length $f_{CX} = 100\ mm$ lens was used as the CX element. For 4× magnification, a –25 mm CC lens was used. For 2× magnification, a –50 mm CC lens was substituted. For the 1× setting, the expander was removed entirely. Each change in magnification required replacing the CC lens accordingly. The Table 2.5 shows the distance separations.

Table 2.5: Magnification modes with a corresponding concave lens and lens separation

Mode	**CC Lens f_{CC} (mm)**	**Lens Separation d (mm)**
4× mode	–25	69
2× mode	–50	44
1× mode	—	Expander removed

Since the beam path from the source to the camera is approximately 1.6 meters, even slight divergence or convergence in the beam is noticeable and must be compensated. To characterize the laser's natural collimation and adjust for it, the focusing behavior of the beam was measured using only the CX lens. While the lens nominally has a focal length of 100 mm, the measured focus position *a'* varied depending on the adjustment of the laser expander collimation ring. The beam was adjusted to provide a sufficient diameter for plasma imaging, yielding $a' = 94$ mm. From the thin-lens equation, the inequality $a' < f_{CX}$ indicates a diverging input beam. Therefore, the lens separation was reduced by $f_{CX} - a' = \Delta = 6$ mm. The resulting effective magnifications (0.94×, 1.88×, and 3.76×) and corresponding pixel resolutions are summarized in Table 2.6.

Table 2.6: Nominal and effective interferogram magnifications with corresponding camera resolution

Mode	**Nominal Mag.**	**Effective Mag.**	**Camera pixel resolution (µm)**
1× mode	1	0.94	27.7
2× mode	2	1.88	13.8
4× mode	4	3.76	6.9

A mechanical constraint imposed by the thick socket of the beam splitter further restricted the beam cross-section at that point in the optical path. This mechanical shadowing was most noticeable at 1× and 2× magnifications, where the beam did not fully cover the entrance aperture of the second lens or the camera sensor. Nevertheless, this limitation did not significantly affect the quality of the acquired interferograms, aside from a modest reduction in the usable image area and spatial coverage.

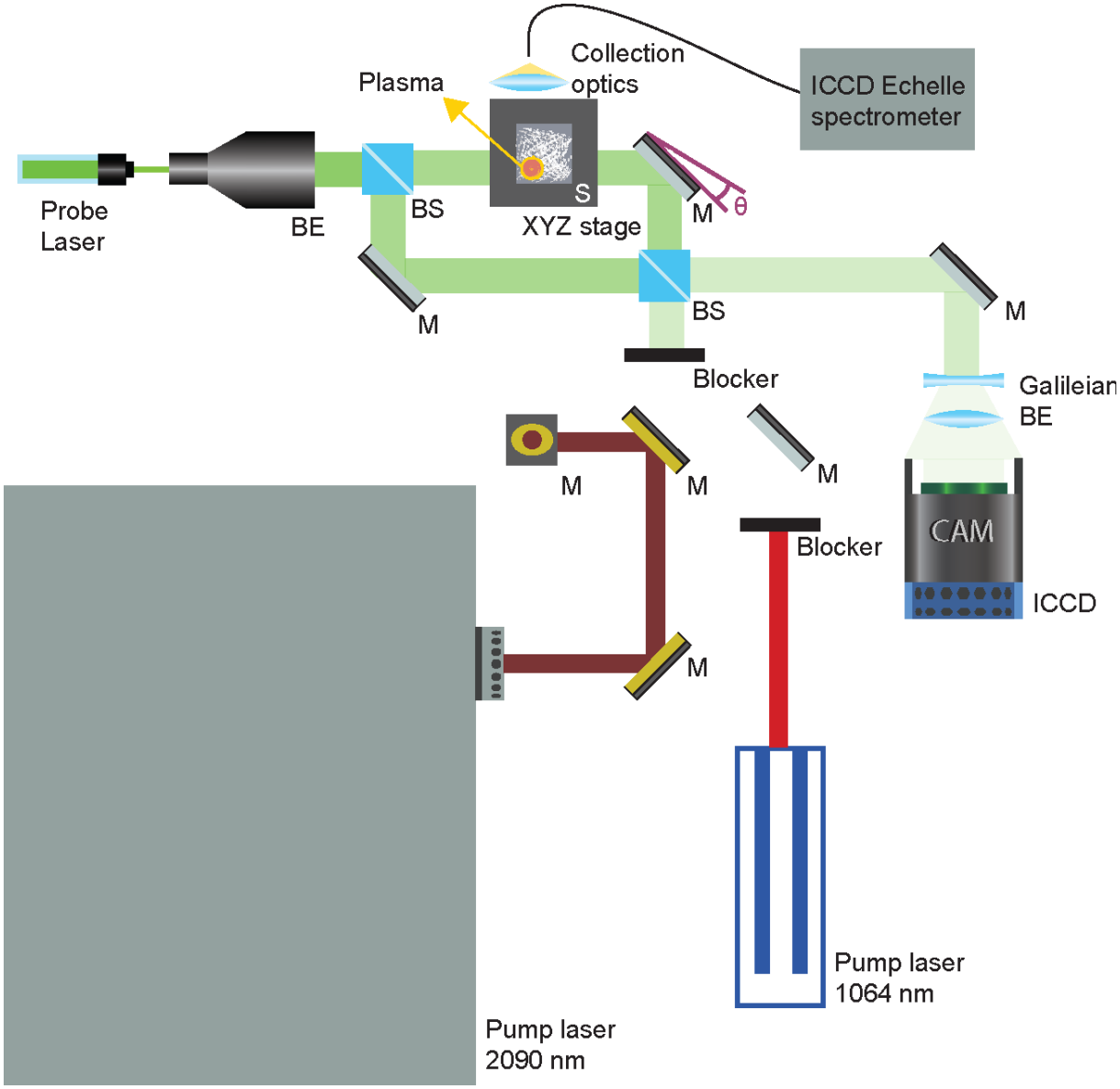

Figure 2.2: Measuring setup scheme. Green lines indicate the Mach-Zehnder probe laser path, red and dark red lines indicate pump lasers, where the 2090 nm is unblocked. M - Mirror, BE - Beam expander, S - sample, BE - Beam expander

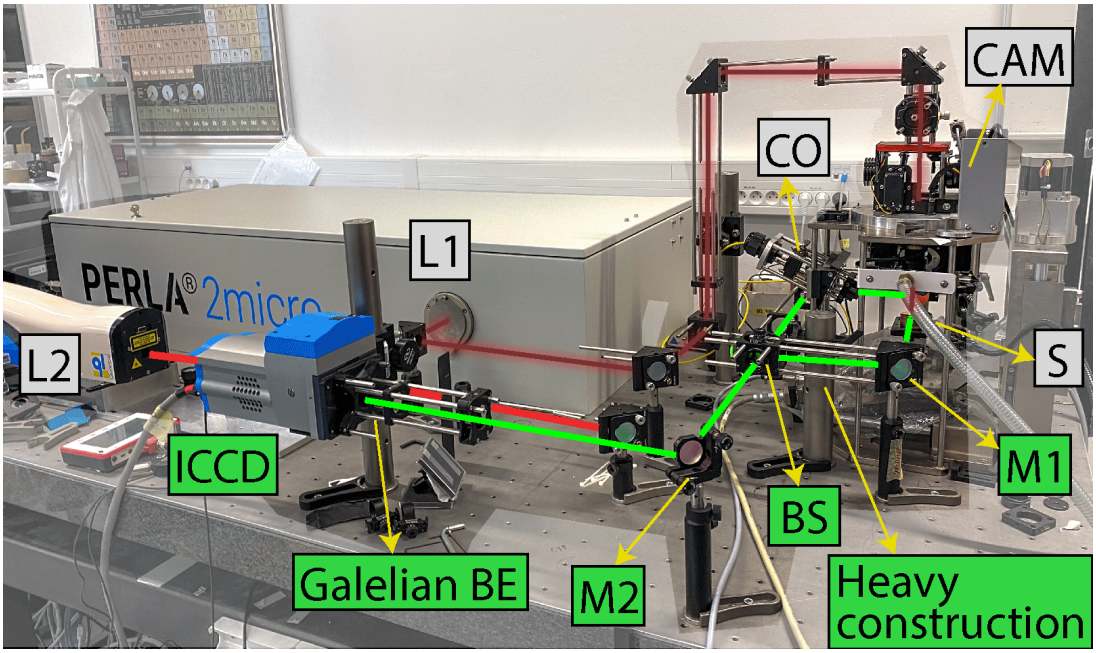

Figure 2.3: Measuring setup image. Green lines indicate the probe laser path, red L1 (1064 nm) and dark red L2 (2090 nm) indicate the pulsed laser path. The 1064 nm path is blocked. Green labels highlight parts of the setup I built, and gray labels highlight standard LIBS components. BE - interferogram beam expander, M1 - Mirror used to fine control fringes, M2 - mirror for additional image alignment, CO - collection optics, CAM - camera from viewing sample, S - sample

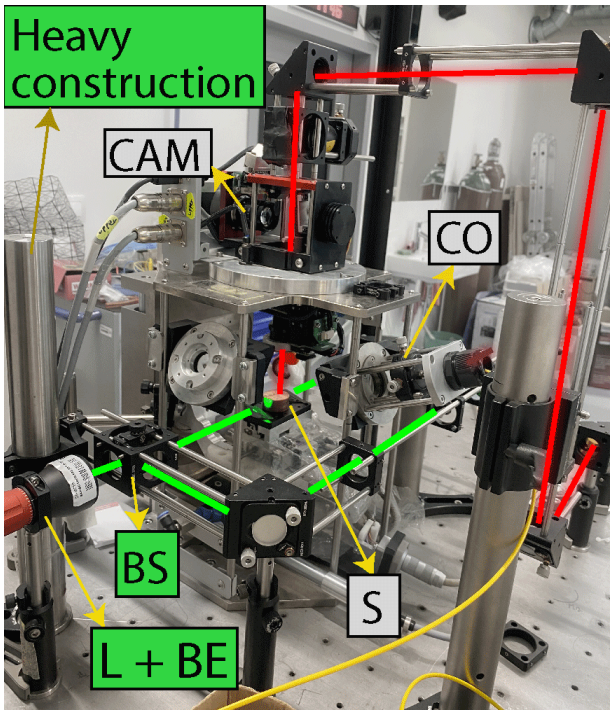

Figure 2.4: Measuring setup image from a different angle. Green labels highlight parts of the setup I built, and gray labels highlight standard LIBS components. L + BE - Probe laser + laser beam expander, BS - Beam splitter, CO - collection optics, CAM - camera from viewing sample, S - sample

2.3. Measurement methodology

To evaluate the performance of the Mach–Zehnder interferometer and validate the electron density reconstruction methodology, steel samples with identical chemical composition but subjected to different heat treatments were analyzed. These treatments resulted in varying hardness levels, potentially giving rise to the physical matrix effect. Additionally, a copper sample was included to investigate the response of a material with a distinctly different elemental composition. The microstructure of the steel samples, which underlies their mechanical properties, has not yet been determined and is outside the scope of this thesis. All measurements were conducted using pulsed lasers operating at wavelengths 1064 nm and 2090 nm mentioned in Section 2.1.

A sample overview can be seen in Table 2.7. Steel samples were prepared and measured by material scientists at Brno University of Technology. Hardness was determined with the Brinell method 5/750, performing three measurements.

Table 2.7: Overview of measured samples with additional information about hardness and heat treatment for steel

Sample	**Heat Treatment**	**Hardness** ($\mathrm{kg \cdot f/mm^2}$)
H0	without heat treatment, i.e. as cast	161
H3	normalizing 920°C/2h/ventilator + hardening 920°C/2h/water + tempering 620°C/2h/furnace	183
H6	normalizing 920°C/2h/ventilator + hardening 920°C/2h/water + tempering 200°C/1.5h/air	346
Cu	no heat treatment (copper sample as received)	–

Before measurements, the sample surfaces were first brushed with fine sandpaper to expose a fresh area, removing any baked-on oils or carbon residues from previous LIBS analyses. Each laser-induced plasma event was recorded individually because the plasma evolves too quickly for the ICCD camera's frame rate, and every shot was made on a newly cleaned region of the sample. To ensure the probing beam struck the surface at right angles, all samples were carefully leveled with adhesive putty, compensating for any wedge-shaped geometry. Precise synchronization of the spectrometer and ICCD camera timing with the rest of the electronics was carried out to determine the exact moment of plasma formation. The delay at which the first detectable emission appeared was then used as the reference point for all subsequent data acquisitions. This has been achieved with 50 ns precision. The spectral and imaging cameras were synchronized to acquire data at identical time points, with the spectral data primarily serving the purpose of validating the early stages of plasma evolution.

Sample H0 was measured using a half-step increment across all time intervals, except for the 50–1000 ns range, in comparison to the other samples. This approach was taken to refine the selection of step size and time intervals for subsequent measurements, as well as to determine the appropriate magnification of the plasma interferogram. Changing

magnification is important because the plasma initially forms as a small, localized event and later expands significantly, requiring increased spatial detail to capture its evolution accurately. The step size was set to increase exponentially. The first events are happening very fast, requiring exposure times close to the operational limit of the ICCD camera. Due to the use of higher magnification via the beam expander and the reduced exposure times, the captured intensity was significantly lower. To compensate for this, the ICCD camera gain was set to 240 (-) (with 255 (-) being the maximum) at 4x and 2x magnification, and set to 190 for 1× magnification. The spectral camera gain was fixed at 180 and remained unchanged during the most critical time interval range of 50 ns to 2 µs. It is important to note that gain values do not correspond to a linear increase in signal amplification, therefore, changes in gain can have a disproportionate effect on measured spectra intensity. Table 2.8 summarizes the key time-related measurement settings.

For each sample, a total of 72 time frames were recorded across three different magnifications. To ensure statistical reliability, each time frame was captured 10 times, resulting in a large dataset of 720 plasma images per sample. Reference images, crucial for electron density map reconstruction, were acquired at the end of each measurement sequence. For each magnification set up, the number of interference fringes may need to be adjusted to remain within the camera's resolution limits. Based on prior experience, a minimum of 24 visible fringes is recommended for good resolution and reliable data reconstruction at any magnification level. The fringes should be placed horizontally, i.e., parallel to the plasma expansion direction.

Additionally, the final mirror directing the plasma projection onto the camera sensor required manual adjustment to include a small portion of the sample base in the frame. This ensured the entire plasma was captured without accidental cropping. It is also ideal to keep the image in the middle of the camera sensor to avoid any optical distortion. Alignment was carried out using the camera's live view mode.

Table 2.8: Time intervals, step sizes, and number of measurements at various magnifications

Nominal magnification	**Time interval**	**Step size**	**No. of images**
4×	50 ns – 1000 ns	50 ns	20
	1.1 µs – 2.1 µs	200 ns	6
	2.2 µs – 5 µs	400 ns	8
2×	6 µs – 15 µs	1 µs	10
	25 µs – 95 µs	10 µs	8
1×	100 µs – 2 ms	100 µs	20

Proper focusing of the pulsed laser was performed using the LIBS Navigator software to ensure the smallest possible laser spot. To verify the focusing quality, I imaged the resulting ablation craters using a scanning electron microscope (SEM). An example image for H0 is shown in Figure 2.5. The diameters of the craters, which closely correspond to the actual size of the focused laser spots, were measured directly from the SEM images. The 1064 nm laser was focused to a radius of approximately 120 µm, while the 2090 nm laser was focused to a smaller radius of around 50 µm. The measured pulse energy for the 1064 nm laser was approximately 23 mJ, and for the 2090 nm laser, 3.65 mJ. Using the

irradiance formula presented in Section 1.1.3, the corresponding peak laser irradiances were calculated as: $I_{1064\,\mathrm{nm}} = 4.1 \times 10^{10}\ \mathrm{W\,cm^{-2}}$ and $I_{2090\,\mathrm{nm}} = 4.7 \times 10^{10}\ \mathrm{W\,cm^{-2}}$.

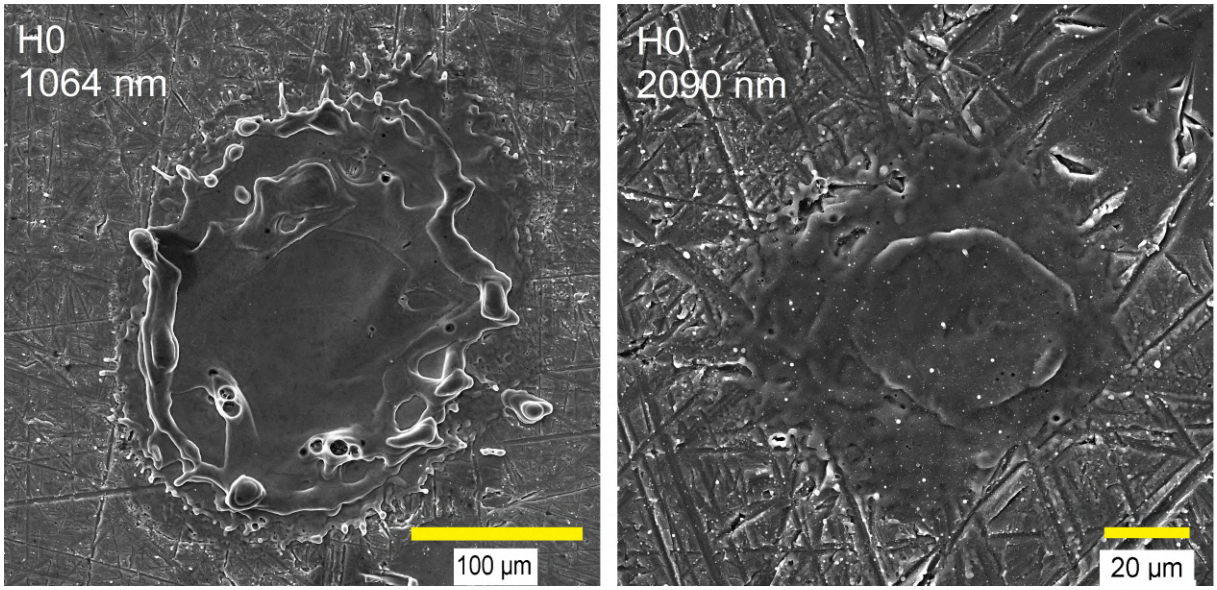

Figure 2.5: Craters for a single laser shot under Scanning Electron Microscope for H0 sample. Imaged on Tescan VEGA at 30keV, probe current 12 nA.

2.4. Spatial measurement

I have successfully measured image data at 2090 nm laser for all listed samples in Table 2.7. And only H0 and H6 samples for 1064 nm. Here, I discuss the form the data takes and what can be seen in the interferometric images.

At times of 50 ns and a pulse length of one order smaller (4 or 5 ns), the observable plasma is already cooling down. As this happens, the spectrum is most visible in the first microsecond and rapidly decreases as seen in Figure 2.6.

In the supplementary section, Figure 4.25 is a time evolution for all important time events seen in the images for 1064 nm measurement for H6 sample. In the first 50 - 150 ns, the plasma high-intensity radiation can enter the Mach-Zehnder interferometer optics, so a bright distorted spot can be seen in the upper left corner of the images. The plasma starts to take shape at 100 ns, creating shock wave ripples in the first 400 ns. Then it starts to expand rapidly up to about 4 μs, creating a shock wave in the process. After the shock wave leaves the field of view, the hydrodynamic fission starts to take place, which means a bubble object starts forming at the top. At this point, the plasma starts being asymmetric as the bubble is trying to leave the plasma. When the bubble leaves, it creates a Rayleigh-Taylor instability, which can be seen at hundreds of μs. This is a very unstable event, and can happen anywhere between 50 μs and 1 ms. The instability starts to fade after, and any trace of plasma completely disappears till 2 ms.

The interferometric measurements for 2090 nm can be seen in the supplementary section, Figure 4.28. It fades much quicker than for a 1064 nm pulse at around 25 μs, and no Rayleigh-Taylor instability is observed.

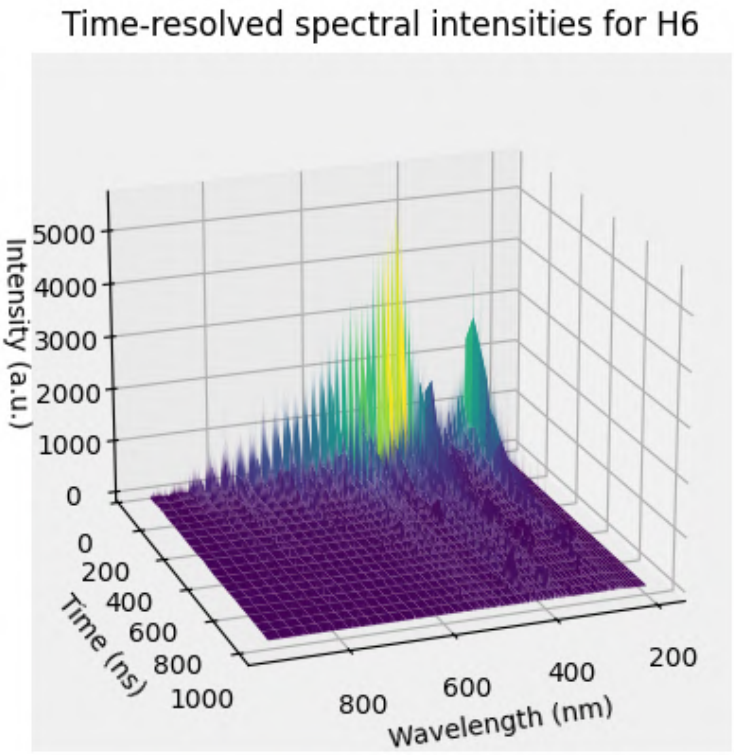

Figure 2.6: Spectral evolution in 50 - 1000 ns time span for steel H6 sample with 2090 nm laser.

2.5. Shock wave measurement

Since the plasma was generated under atmospheric conditions, the ambient gas is compressed by the rapidly expanding plasma, resulting in the formation of a shock wave. The velocity of this shock wave provides additional insight into the ablation process.

For the images, I selected time points shortly after shock wave formation, focusing on those that provided the clearest measurements. Observations indicate that the shock wave consistently begins to propagate at the same time frame for a given pulse energy and sample, suggesting that its initiation is largely independent of plasma fluctuations. The comparison if data visibility in images can be seen in Figure 2.7. The onset times of shock wave formation are summarized in Table 2.9. The time-resolved distance data, particularly distinct in the 1064 nm measurements, are presented in Figure 2.8. The corresponding results from fitting the shock wave propagation are provided in Table 2.10.

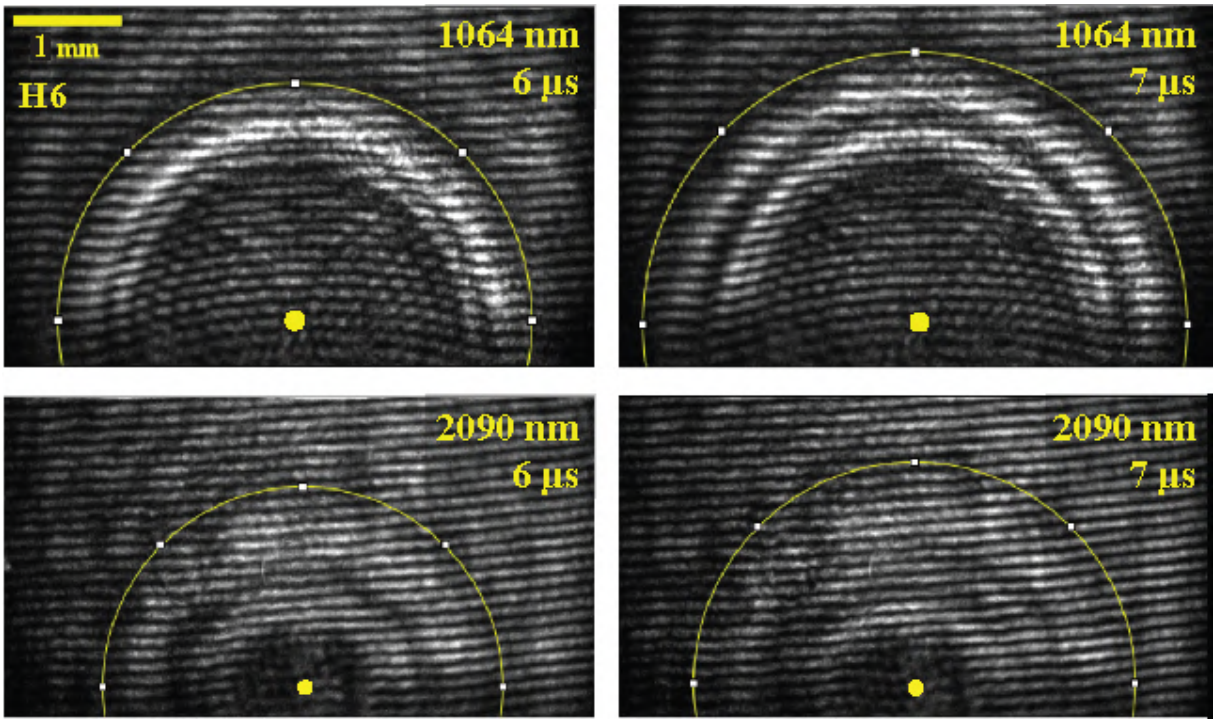

Figure 2.7: Shock wave examples for steel sample H6 at times 6 and 7 µs. The yellow point represents the center of plasma, and the yellow circle is the tool outline used in ImageJ to measure the radius.

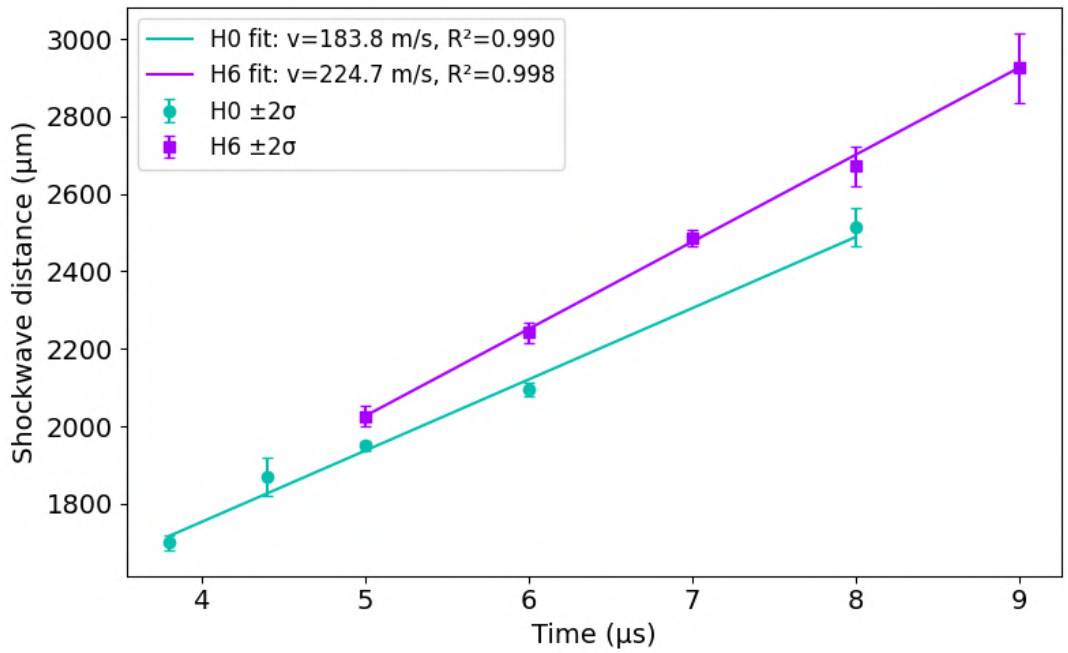

Figure 2.8: Shock wave time/distance linear fit for 1064 nm

Table 2.9: Observation times of clearly defined shock-wave formation in an image

Measurement	t (µs)
H0 1064 nm	3.8
H6 1064 nm	4.6
H0 2090 nm	3.4
H3 2090 nm	3.4
H6 2090 nm	3.0
Cu 2090 nm	2.6

Table 2.10: Average velocities from linear fits with $2\,\sigma$ errors

Measurement	**Velocity (m/s)**
H0 1064 nm	(183.8 ± 17.7)
H6 1064 nm	(224.7 ± 12.4)
H0 2090 nm	(211.1 ± 7.8)
H3 2090 nm	(213.9 ± 6.8)
H6 2090 nm	(202.9 ± 5.5)
Cu 2090 nm	(199.3 ± 7.1)

For the 1064 nm laser, the H6 sample exhibited a higher shock wave velocity compared to the H0 sample, indicating greater plasma energy. This suggests that a smaller portion of the pulse energy is required for material ablation, making the process more efficient in the H6 case. Additionally, the shock wave formation occurred later in H6, which may further reflect differences in energy deposition and plasma evolution.

In contrast, the results for the 2090 nm wavelength are less conclusive. The uncertainty intervals of the measured velocities overlap significantly, preventing a clear distinction in performance among the samples. Overall, the 2090 nm data lack definitive trends. In comparing the two laser wavelengths, the 1064 nm laser, with its higher pulse energy, consistently generated a more pronounced and well-defined shock wave, which appeared later in the sequence of interference images. The velocity differences between samples were also more discernible at 1064 nm. Conversely, the 2090 nm images produced weaker, less distinct signals, making measurement more challenging. The precise identification of the sample base in the interference images was often difficult, which contributed to measurement uncertainty.

2.6. Electron density reconstruction and image data handling

As measurements produced a large collection of images, manual post-processing became untenable. The twenty-year-old IDEA software provides only rudimentary routines that must be executed by hand, resulting in roughly ten minutes of labor per image. No existing tool offers an automated solution for this workflow. To address these bottlenecks, I developed a semi-automated script that reduces the processing time of a single image to just a few seconds. I have chosen the open-source Python programming language for its wide range of built-in tools and community-developed modules, which allow for the implementation of complex data-processing workflows in a fairly short amount of time. The following flowchart in Figure 2.9 gives an overview of the steps and logic behind the script.

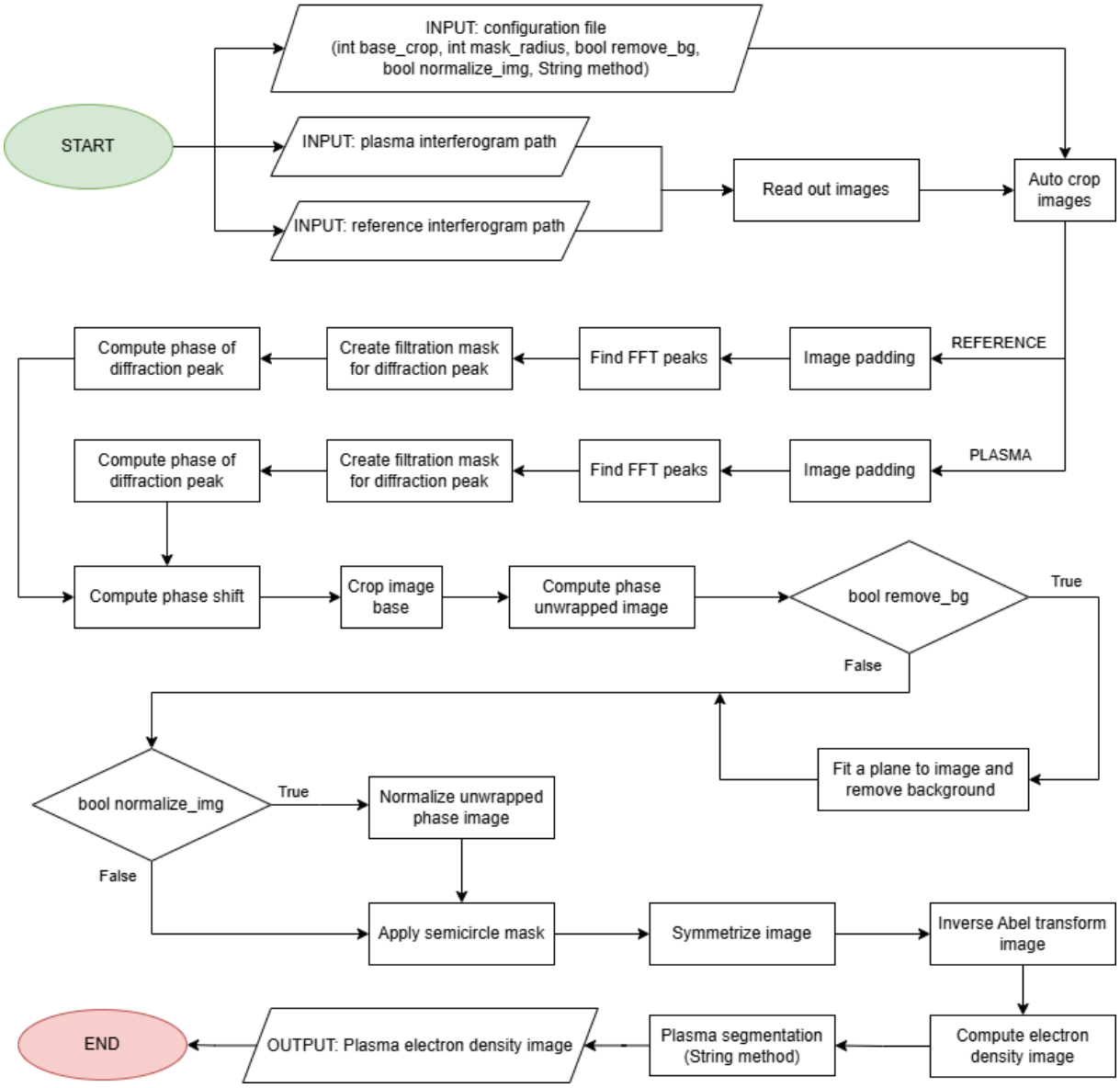

Figure 2.9: Electron density reconstruction flowchart

The following section provides a step-by-step description of the full processing pipeline, illustrated using a representative example: an image from the H6 sample at 2090 nm, recorded at 1.9 µs with 4× magnification.

2.6.1. Data preparation for phase extraction

From Fourier analysis, it can be deduced that any non-linear remapping of pixel values will almost certainly alter the phase spectrum. Those can be gamma correction or histogram equalization. Only linear operations with the form $g = \alpha f + \beta$ (where f is the input image, g output, and α, β are constants) leave the phase intact and can be used to prepare the data for the Fourier transform. Those can include simple data normalization to values (0,1). My data, however, did not seem to require any linear transformation. The raw input images colored with a green look-up table for greater visibility can be seen

in Figure 2.10 and in Supplementary Figure 4.1.

Figure 2.10: Raw unedited interferogram images of Plasma and reference, they are underexposed even for the camera gain of 245 (-), green colormap is used.

Assuming the input data is of sufficient quality, the first step after loading is to automatically crop the image. This is necessary because the region of interest—typically the area of highest intensity—does not always lie in the geometric center of the sensor. To address this, it is assumed that the plasma lies approximately at the center of the high-intensity region. The cropping algorithm begins by computing a one-dimensional intensity profile, obtained by summing pixel values along each column of the image (seen in Supplementary section Figure 4.2). This profile is then smoothed using a Gaussian filter with a standard deviation of $\sigma = 5$, which serves to reduce noise and suppress small fluctuations. Next, the gradient of the smoothed profile is calculated to identify rapid changes in intensity, corresponding to edges of the bright region. The gradient profile graph can be seen in Figure 4.3. A dynamic threshold method is applied. Only gradients exceeding 30% of the maximum gradient magnitude are considered significant. The first position where the gradient exceeds this positive threshold is interpreted as the left edge, and the last position falling below the corresponding negative threshold is taken as the right edge. This approach enables robust detection of the horizontal boundaries of the region of interest, independent of absolute intensity levels. An extra cropping parameter is needed to include only the central part of the image. I have set them to be 40 px for 4x magnification, and 20 px for 2x and 1x magnifications. The function returns a cropped image symmetrically around the center of the left and right boundaries to ensure an odd number of column pixels. This will be useful for the symmetrization step. The cropped images are in the Supplementary section in the Figure 4.4.

As the image has discrete, finite values, the next step is to pad the image borders. This will reduce the artifacts made by the Discrete Fourier Transform algorithm. Zero padding 15 px around the image yielded good results.

2.6.2. Phase extraction

The Fast Fourier Transform (FFT) algorithm was used to compute the Fourier transform of the interferograms. The resulting shifted logarithmic amplitude and phase spectra are shown in Figure 4.5 for the plasma interferogram, and in Figure 4.6 for the reference interferogram in the Supplementary section. As described in the theoretical background (Section 1.3.3), the ± 1 diffraction orders contain the relevant phase information that must be extracted. The distance between the 0th diffraction order (i.e., the zero frequency) and the ± 1 orders is proportional to the number of fringes in the original interferogram. If the fringes are perfectly horizontal, all diffraction maxima will lie along the same central

column index.

The first function locates the diffraction maxima. To prevent false detection near the origin, a circular region with a radius of 8 pixels is masked out around the 0th-order peak. Then a smoothing Gaussian function ($\sigma = 2$) is used to lower noise and enhance the true maxima location. The image is unraveled into a 1-D array, and then the first maxima is found as the location of the first peak. That peak is then masked out to allow detection of the second strongest peak. The coordinates of both detected peaks are then recovered. Their vertical positions (row indices) are compared with the center row of the image to determine whether they lie above or below the central axis. The peak above the center line is designated as the $+1$ diffraction order, while the one below is labeled as -1. The function ultimately returns the coordinates of all three diffraction orders: the central (0th), the +1st, and the −1st.

The user then selects which diffraction peak to use for phase extraction. To ensure consistency, the same diffraction order must be used for both the reference and plasma interferograms, and identical filtering parameters must be applied. An elliptical mask with values in the range [0,1] is generated by the next function. The center of the ellipse is positioned at the selected diffraction peak coordinates. The major axis is set to $a = 100\ px$, while the minor axis b is defined as the vertical distance between the 0th and ± 1 diffraction orders $b = |y_{Center} - y_{DO}| - 1$. This choice ensures that the mask excludes the 0th-order peak and captures the full frequency content of the selected diffraction maximum, enabling smooth and more accurate phase reconstruction. The mask can be optionally smoothed out by a Gaussian filter with a recommended minimum of $sigma = 1$. An elliptical mask ensures a degree of symmetry, which is beneficial for spectral filtering by including a similar portion of frequencies from all directions.

The mask is applied to the padded complex Fourier spectra of both the reference and plasma interferograms. The filtered spectrum of the plasma image can be seen in Figure 4.7 in the Supplementary section. The third function returns a phase image information part of the spectral diffraction peak, yielding a phase image $\Phi \in [-\pi, \pi)$ in real space. Finally, the result is cropped to remove the padding and restore the original image dimensions. Result can be seen in the Supplementary section in Figure 4.8.

2.6.3. Phase shift and phase unwrap handling

The phase shift was calculated by subtracting the two phase images $\Delta\Phi = \Phi_{ref} - \Phi_{plasma}$. The resulting phase shift image $\Delta\Phi$ is then wrapped into the interval $(0, 2\pi)$ using the modulo operation:

$$\Delta\widetilde{\Phi} = \Phi \bmod 2\pi, \tag{2.3}$$

so that $\Delta\widetilde{\Phi} \in [0, 2\pi)$. The raw phase shift can be in the Supplementary section in Figure 4.9, and the modulo wrapped image in Figure 4.10.

If the interferograms are well aligned (i.e., the fringes match), the resulting phase shift map appears smooth. However, a clear uneven region is now revealed near the bottom

of the image, corresponding to the base of the sample. This region introduces instability into the unwrapping process and must be cropped out to ensure clean results. Since the sample position is fixed for a given magnification and setup, this cropping threshold can be determined in advance for multiple measurements. An additional script was created to process sample images and determine the optimal crop margin. For the dataset shown in the Supplementary Figure 4.10, 15 rows were cropped from the bottom of the image. Additionally, artifacts often appear near the top and along the sides of the phase image. To eliminate these, an extra 10 pixels were removed from the top, left, and right edges of the final result.

The unwrapped phase image $\psi = \mathcal{W}^{-1}\{\widetilde{\Phi}\}$ is, in the context of Abel inversion, interpreted as the projection. Many algorithms exist for two-dimensional phase unwrapping, and the choice of method significantly affects the quality of the result. For this application, the most critical requirement is that the unwrapped phase map be smooth and free from artificial discontinuities or phase jumps. A reliable algorithm was implemented from the Scikit-restoration library. Details about this method can be viewed in the source [49]. The unwrapped result reveals the plasma structure. It is shown in the Figure 2.11 and in the Supplementary Figure 4.11.

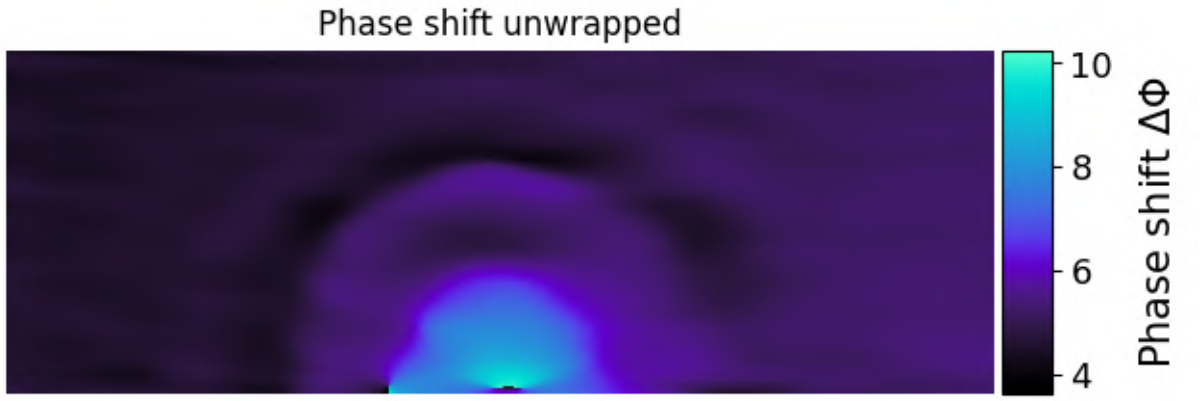

Figure 2.11: Unwrapped phase shift image

2.6.4. Abel inversion data preparation

The projection (i.e. the phase-unwrapped image ψ) requires additional pre-processing before it can be used in the Abel inversion. In particular, I observed that the background of the projection often exhibits a gradual gradient. After experimenting with different polynomial surface fits, I found that this background variation is best approximated as a linear tilt. To correct for it, I implemented a function that fits a first-order plane to the image using a least-squares approach. First, the linear system needs to be created as an input to a built-in function in the numpy library. Each pixel in the $H \times W$ (Height $\times$ Width) image is turned into a set of data points (x_k, y_k, z_k) by flattening the pixel grid and its values, where

$$x_k = j, \quad j \in \{0, \ldots, W-1\}, \quad y_k = i, \quad i \in \{0, \ldots, H-1\}, \quad z_k = \psi \text{ pixel value at } (i, j).$$

Stacking all $N = H \times W$ of these into vectors $\mathbf{x}, \mathbf{y}, \mathbf{Z}$ yields a matrix:

$$A = \begin{pmatrix} 1 & x_1 & y_1 \\ 1 & x_2 & y_2 \\ \vdots & \vdots & \vdots \\ 1 & x_N & y_N \end{pmatrix}, \quad \mathbf{c} = \begin{pmatrix} c_0 \\ c_x \\ c_y \end{pmatrix}, \quad \mathbf{Z} = \begin{pmatrix} z_1 \\ z_2 \\ \vdots \\ z_N \end{pmatrix}. \tag{2.4}$$

By solving the linear system $\mathbf{Z} = A\,\mathbf{c}$ using least squares minimalization, the coefficient vector $\mathbf{c} = (c_0, c_x, c_y)^T$ is obtained. Finally, the fitted background plane is reconstructed as a linear combination of three basis components, being a constant, column index, and row index given by:

$$\mathrm{bg}(i, j) = c_0 + c_x\, j + c_y\, i. \tag{2.5}$$

The background is then subtracted from the projection. Thanks to this improvement, much data could be processed more accurately. I have included another example in the Supplementary section, Figure 4.12. Without this step, the data would not be suitable for analysis.

Because Abel inversion assumes that the function vanishes outside the region of interest $(r >= R) = 0$, it is essential to ensure that all values beyond this boundary are zero. This condition is important because all the values inside the area will influence the inversion result. To satisfy this assumption, a semicircular mask was applied to the image. For the example shown in Supplementary Figure 4.13, the chosen radius was $R = 100$ px. This radius is another parameter that needs to be known before the script's usage. An optimal radius is slightly larger than the largest plasma size in the given time interval and magnification measurement.

Abel inversion also assumes a symmetric input, i.e. $h(x) = h(-x)$. To enforce this condition, I implemented a simple and robust symmetrization procedure based on the Fourier transform. The input 1D profile $h(x)$ is first transformed into the frequency domain using the FFT algorithm. This gives complex coefficients $H(k) = \mathcal{F}\{h(x)\}$. In the Fourier domain, the real part of each frequency corresponds to the even (symmetric) component of the signal, while the imaginary part corresponds to the odd (antisymmetric) component. To retain only the even part, the imaginary components are discarded $H_{\mathrm{even}}(k) = \mathrm{Re}\{H(k)\}$. Applying the inverse Fourier transform to this modified spectrum reconstructs a symmetrized version of the original profile $h_{\mathrm{sym}}(x) = \mathcal{F}^{-1}\{H_{\mathrm{even}}(k)\}$. The additional option of Gaussian smoothing was introduced as some Abel inversion algorithms may not handle sharp jumps and noisy data well. Because the image has an odd number of columns and the profile is symmetrized, the true center is now found in the central pixel column. Only half of the symmetrized projection image, including the central column, is needed for Abel inversion. The Supplementary Figure 4.14 shows the resulting symmetrized profile.

2.6.5. Abel inversion and electron density profile

Numerous algorithms exist for performing Abel inversion, many of which are implemented in the open-source PyAbel library. The library also provides a detailed comparison of the available methods, including performance and reconstruction quality. For this work, the

BASEX algorithm was selected. It is based on a basis-set expansion approach, in which the projection is modeled as a weighted and optimized sum of Gaussian functions with their known analytical inverse Abel transforms. This algorithm requires several input parameters that influence the behavior and quality of the inversion. In this work, a Gaussian basis width $\sigma = 2$ was selected to provide a balance between smoothness and resolution in the reconstructed profile. Narrower basis functions (smaller σ) yield higher resolution but are more susceptible to noise, while wider basis functions (larger σ) produce smoother, more stable results at the cost of fine detail. The pixel spacing was set to $dr = 1$, ensuring that the output preserves the same spatial resolution as the input image. The Tikhonov Regularization Strength parameter was set to $reg = 10$, which improved numerical stability and suppressed noise without overly blurring fine details. In general, lower values of reg preserve more detail but may introduce noise and artifacts, whereas higher values improve stability but may reduce resolution. Additionally, the built-in correction was enabled ($correction = True$) to account for minor intensity offsets introduced during the inversion process. These parameter values produced consistent and physically reasonable results across all the datasets. The 1-D resulting inversion can be seen in Supplementary Figures 4.15 (1-D phase shift profile), 4.16 (1-D symmetrized profile), 4.17 (1-D Abel inversion). The 2-D result for Abel inversion is in Figure 4.18. In the majority of cases, a high-intensity ring artifact appeared near the edge of the semicircular mask used during preprocessing. This artifact can be effectively removed by applying an additional semicircular mask with a slightly smaller radius, typically reduced by 10 to 20 pixels, thereby excluding the affected boundary region.

The Abel inversion yields a map representing the change in the refractive index of the medium. By applying the Drude model equation (outlined in the theoretical Section 1.1.2 and Equation 1.7), this map can be transformed into an electron density distribution. The local refractive index is computed as

$$N_O = (N_{air} - \Delta N_O), \tag{2.6}$$

where $N_{air} = 1.0003$ is the refractive index of air under standard conditions, and ΔN_O is the change recovered from the inversion (outlined in the theoretical Section 1.3.3 and Equation 1.24). Since the electron density corresponds to regions where the refractive index drops below unity ($N_O < 1$), care must be taken when evaluating expression $\sqrt{1 - N_O}$. In this work, any resulting negative square roots were handled by setting the value to zero to avoid unphysical (complex) results. Finally, the angular frequency is calculated for the probing laser as $\omega = 2\pi \frac{c}{532 \times 10^{-9}}$.

2.6.6. Plasma segmentation

Once the plasma structure was revealed by the Abel inversion, it became necessary to define a binary mask in order to calculate the average electron density accurately. Since the plasma evolves over time and can vary significantly between measurements, a universal segmentation strategy was not feasible. Instead, a tailored approach was applied to each dataset to ensure decent segmentation. In total, four methods (and one supplementary) were implemented:

- **Radius mask method:** This is the simplest but the least precise approach. It uses the circular mask function from the pre-inversion step. The smallest possible radius

that fully encloses the plasma is manually identified and applied to the electron density map.

- **Non-zero mask method:** This method provides precise segmentation when the plasma is clearly separated from the background. Only non-zero values are included in the mask, assuming the background has been successfully zeroed. The radius mask may optionally be used to enforce a clean boundary.
- **Otsu's method:** This thresholding method segments the image by dividing its histogram into two classes. Classes are typically corresponding to dark (background) and bright (plasma) regions. It is a global thresholding technique implemented via the skimage library.
- **Multi-Otsu's method:** Similar in principle to Otsu's method, this technique divides the image histogram into multiple intervals (a minimum of three), as specified by the user. One of these intervals is then selected to define the plasma region. This method is also implemented using skimage.
- **Fill bottom method:** The Otsus and Multiotsus methods, in some cases, did not include the bottom part of the plasma near the edge. This function tried to compensate for this issue by including this part if necessary. It worked on a principle of locating the maximal horizontal coordinates of the Otsu or Multi-Otsu mask and, from that point, filling the bottom to the edge of the image.

In the Supplementary section, I have included Tables 4.1 and 4.2 with the parameters and methods used for each measurement. For the 2090 nm measurements, the most effective method in the early stages of Plasma ($50-1000$ ns was the usage of either a radius mask or non-zero segmentation mask methods. This worked due to a well-separated background from the plasma, thanks to the prior handling of electron density computation (negative values become zero). In later stages, a mix of all methods was used. The Otsu and Multi-otsu methods are used in cases when the background near the plasma plume is not clearly separated. This likely happens in the presence of a forming shock wave or poor gradient features of the plasma plume. The radius mask method was used when the features were weak but visible by eye, so the methods presented could not resolve them. The electron density profile can be seen in Figure 2.12 and in the Supplementary Figure 4.19 with the corresponding binary mask as well as segmented in Figure 4.20.

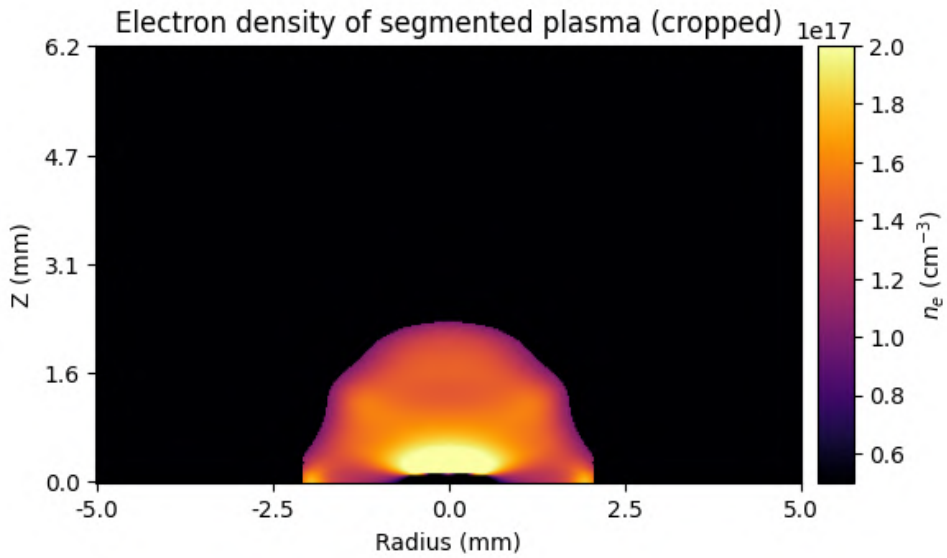

Figure 2.12: Unwrapped phase shift image

A set of slices revealing the internal structure may be visualised from the segmented plasma in Figure 2.13.

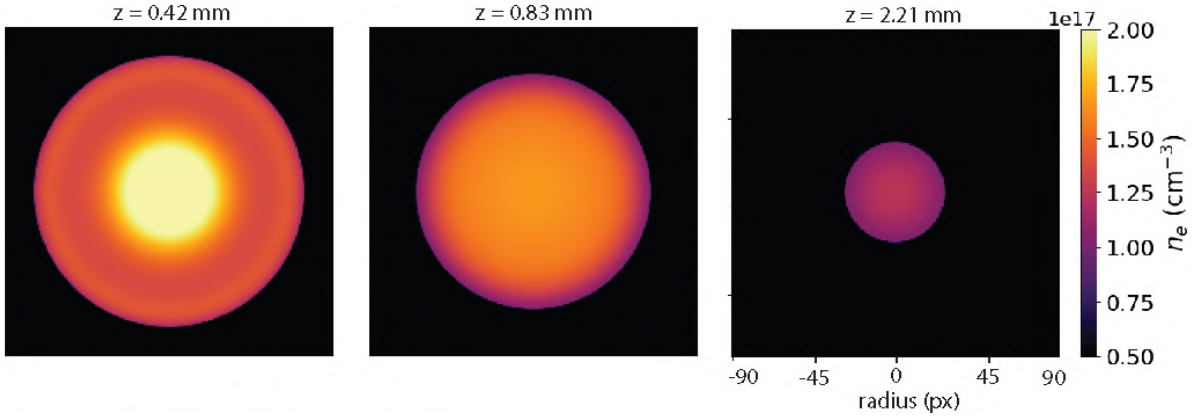

Figure 2.13: Plasma slices for z = 0.47, 0.83, 2.21 mm. The images have the same color map scale. The slices are taken from Figure 2.12.

2.6.7. Challenges, Failed Attempts and Workarounds

The above flowchart and described algorithm only represent the processing of a single image. I attempted to further automate the procedure for application across entire time intervals, as processing each image individually would be impractical for large datasets. This, however, required a larger number of configuration settings on the input.

The first challenge was detecting and removing blurred interferograms from the dataset. This is important as they lose critical spectral information and typically no longer exhibit clear diffraction peaks. Early on, I experimented with a fully automated approach—measuring each image's power spectral density and comparing it to a reference threshold from a "good" image. But this metric proved inconsistent and was ultimately abandoned. Instead, images were reviewed and selected manually, a process that proved

time-consuming but necessary to ensure data quality. To keep a clear consistency, I have created a matrix of binary values representing 1 as sharp and 0 as blurred images from each of the time interval data. This was added to the configuration file. The selection process revealed the amount of usable data, which was between 59% and 85% for all the time interval datasets. An example of the blurry image can be seen in the Supplementary section in Figure 4.21 and its spectrum in Figure 4.22.

Another significant challenge, one that also reduced the amount of usable data, was the correct identification of the diffraction peak used for phase extraction. If the incorrect peak is selected, the resulting phase map becomes distorted. The outer regions of the image may exhibit artificially high values, while the plasma region itself can appear with negative or low phase values. After Abel inversion, this leads to a reconstruction where the plasma region is incorrectly rendered with negative values. When the electron density is computed from such data, these negative values are discarded, effectively zeroing the plasma signal. To mitigate this issue, I initially implemented a method in which the average value within the masked plasma region was compared to that of the surrounding area. If the plasma region exhibited a lower average value, it was assumed that the incorrect diffraction peak had been selected. In such cases, the opposite peak was chosen, and the processing pipeline was rerun. However, this method proved to be unreliable. It did manage to correct some images, but it also produced several false positives (cases where valid data were incorrectly flagged and reprocessed). As a result, this approach was abandoned in favor of a more consistent strategy. A fixed diffraction peak was manually assigned for each time-resolved measurement sequence and stored in the configuration file. While this led to the exclusion of a few additional data points, the trade-off was acceptable as the majority of data in a single time interval tends to follow a single diffraction peak. Again, the problematic interferograms had to be removed from the dataset. Example of +1 and -1 diffraction peak selection can be seen in the Supplementary section in Figure 4.23.

The issue, where Abel inversion returned negative values, also repeated for data where the phase unwrapped image included large negative numbers. Sometimes the image would be only in negative numbers. For those cases, I have added an option to normalize the data by shifting the image values so that its minimum phase value is 0. It only helped in a few cases, and it would not be considered a robust approach. This happened less often after implementing the background removal function.

When calculating the phase image, sometimes the peak can not be located. For this case, I have wrapped the phase extraction method in an exception-handling block, which skips over the image. Such images had to be excluded from the dataset as well.

For the 1064 nm measurements, a low number of fringes was created, which led to poor spectral resolution of the early plasma and made the segmentation challenging. The spacing of the 1st and 0th diffraction orders was 12-16 pixels, indicating a limited range of spatial frequencies. This lack of spectral content caused instability in the unwrapped phase, often manifesting as phase jumps. To address this issue, the center of the elliptical filter mask was manually shifted by 20 pixels away from the zero-frequency peak. Additionally, a larger smoothing parameter was applied to the mask to expand its size and include more of the higher-frequency components. Because a small region around the

zero-order peak was excluded, the mask remained free of phase artifacts. This adjustment produced significantly smoother phase maps and greatly reduced the occurrence of phase discontinuities. As a result, most of the early-time data from the 1064 nm measurements could be recovered and included in the analysis. This can be seen in an example in the Supplementary section in Figure 4.24.

The final issue arose with the use of Otsu's and Multi-Otsu segmentation methods. In some cases, the electron density map lacked sufficient contrast or variation for the histogram-based thresholding to operate correctly. When the plasma and its background were too homogeneous, the histogram could not be meaningfully divided into distinct regions, resulting in an empty or invalid mask and triggering an error. One such example occurred in the copper target measurements at 1–2 µs, where Otsu-based methods failed. In these cases, segmentation was instead performed using the simpler radius mask approach to ensure a valid result.

2.7. Electron density measurement results

Due to the complexity of the process and time constraints, only a subset of the dataset was fully processed. Specifically, data were analyzed for the 1064 nm measurements at time points H0 and H6, and for the 2090 nm measurements at H0, H3, H6, and Cu samples up to 15 μs. These selections were made to ensure the dataset still included a representative sample for analysis.

To compute the mean electron density, the binary segmentation mask was applied to the electron density map, ensuring that only pixels within the plasma plume contributed to the result. By restricting the calculation to the masked region, this method yields more accurate density estimates, in some cases, unbiased by the surrounding plasma background. It also underscores the importance of precise plasma segmentation.

The average value was computed for all the resulting mean electron density calculations. The resulting data points were fitted by polynomial functions for the early development of plasma and its late development:

- **1064 nm:** The data were fitted till 1.1 µs for the early plasma development, then the late plasma was fitted from two time points before (from 950 ns) to get a good continuity of the two fits. The fits can be seen in Figure 2.14 and its polynomial parameters in Table 4.3.
- **2090 nm:** The data were fitted till 3 µs for the early plasma development, then the late plasma was fitted from two time points before (from 2.2 µs). The fits can be seen in Figure 2.15 and its polynomial parameters in Supplementary Tables 4.4 and 4.5.

For the 1064 nm measurements, the electron density is lowest at the earliest time point (50 ns), reaching 0.21×10^{17} cm^{-3}, and increasing rapidly up to approximately 1-2 μs. The highest average electron density observed in this dataset and in all measurements is 2.57×10^{17} cm^{-3}, recorded for H6 at time point 5 µs. H0 sample reaches its maxima at

3.4 µs and is noticeably lower than that of H6 at 2.03×10^{17} cm^{-3}.

At 2090 nm, the trend in electron density evolution follows a similar overall trajectory as in the 1064 nm case, though with some variations in timing and magnitude. Initially, the density is low, followed by a rapid increase until approximately 1–2 µs. For H6, the electron density again reaches the highest values in this dataset at 1.94×10^{17} cm^{-3}, with H0 keeping close to the H6 curve evolution but without any noticeable secondary increase in electron density. H3 then has a slower rising trend along with copper rising until 1.5 µs, then a sudden secondary increase occurs from 3.8 to 8 μs, where both samples reach their maxima. For H3 1.85×10^{17} cm^{-3} and for copper 1.75×10^{17} cm^{-3}. After the second maxima occur, all the electron densities start falling.

Comparing both graphs, for the 1064 nm laser, the electron density reaches higher levels for both samples. The density increases more steadily with fluctuations in early times. For the 2090 nm laser, the electron densities reach lower levels than in the 1064 nm case. Before reaching the second maxima, a sudden drop occurs with later increase and more fluctuations than in the 1064 nm case. Among the samples, H6 consistently exhibits the highest electron densities, while H0 is visibly lower. Copper shows the lowest electron density. After the initial rapid increase, the electron density continues to rise but with noticeable fluctuations, eventually reaching a secondary maximum. The densities start falling after the second (and highest value) maxima in all cases.

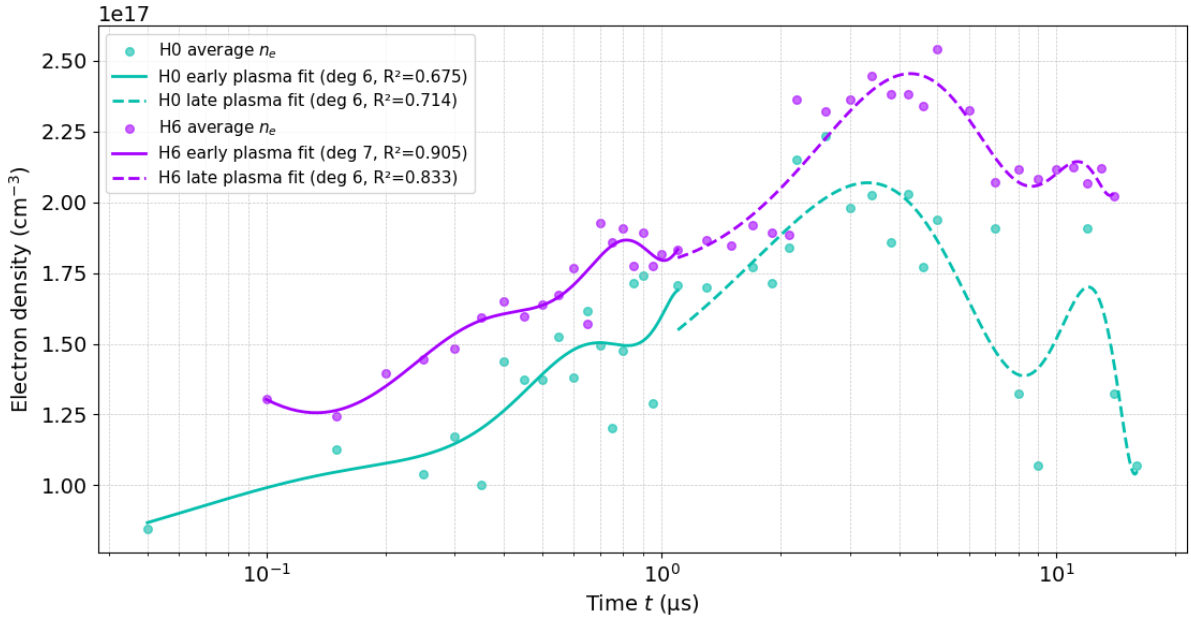

Figure 2.14: Mean electron density average of the plasma area 1064 nm

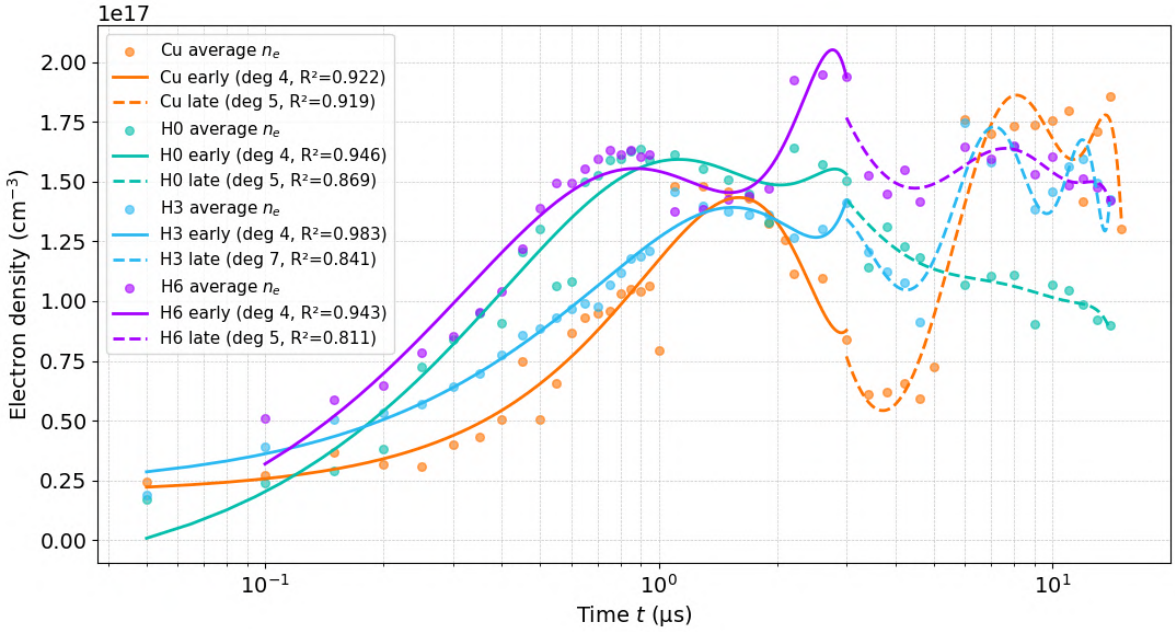

Figure 2.15: Mean electron density average of the plasma area 2090 nm

With the results presented, our attention now turns to understanding the accuracy and limitations of this method. Firstly, the standard error of the mean within a 2-sigma interval was calculated as $\sigma_{3SEM} = 1.55 \times 10^{16}\ cm^{-3}$. This represents approximately 11.4% of the measured data. Such a large deviation could be explained by the lack of usable data caused by vibrations, laser shots taking place on uneven surfaces, and in some cases, poorly defined segmentation borders. Another significant source of uncertainty is the symmetrization deviation. This error arises from assuming a symmetric plasma profile. To assess this, I symmetrized the unwrapped phase profile for each image measurement. Electron density images were then computed separately for each side (left and right). The symmetry between these two density images was evaluated using a correlation analysis. To minimize distortion from background elements, each image was cropped closely around the plasma region. Specifically, cropping followed the boundaries defined by the semi-circular mask applied immediately before Abel inversion. This ensured the plasma remained the primary focus of analysis. From the graph below, we observe that the plasma remains relatively stable during the initial 1 μs. Beyond this point, the uncertainty increases, and the measurements become more influenced by plasma fluctuations and instability in laser pulse energy. The values of symmetrization error can be seen in Figure 2.16.

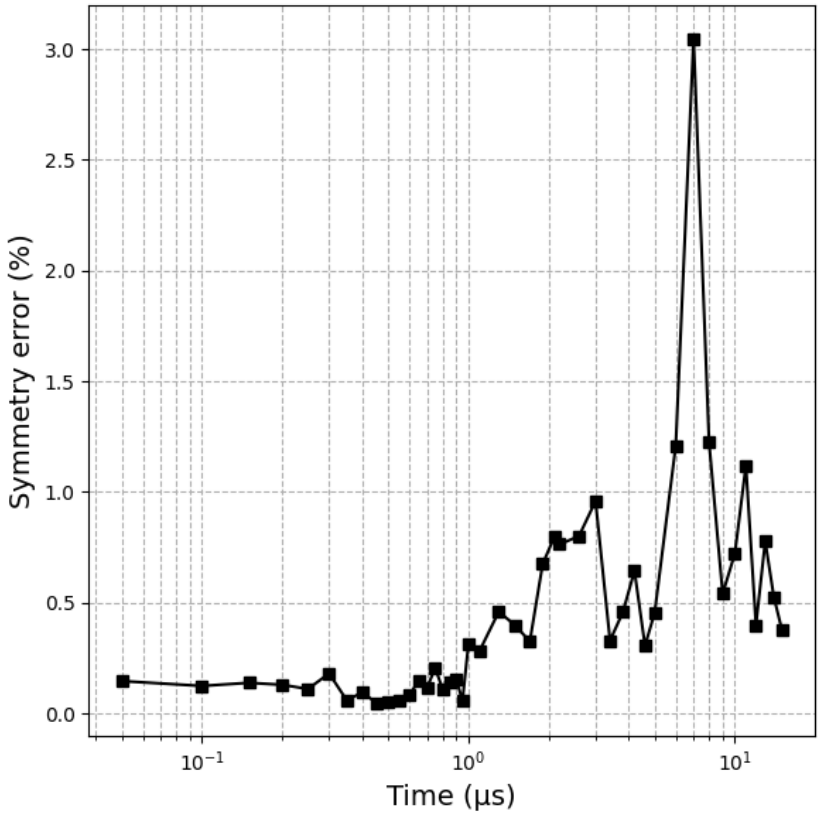

Figure 2.16: Mean symmetrization error of all data

The total error is given by combining the standard error of the mean and symmetry error

$$\Delta = \sqrt{\sigma_{Abel}^2 + \sigma_{3SEM}^2}. \tag{2.7}$$

I have compared the electron density with the plasma spectral irradiance in the following graph 2.17, where the spectral average intensities are normalised along with the electron density curves. It can be seen that as the intensity decreases with time, the electron density increases.

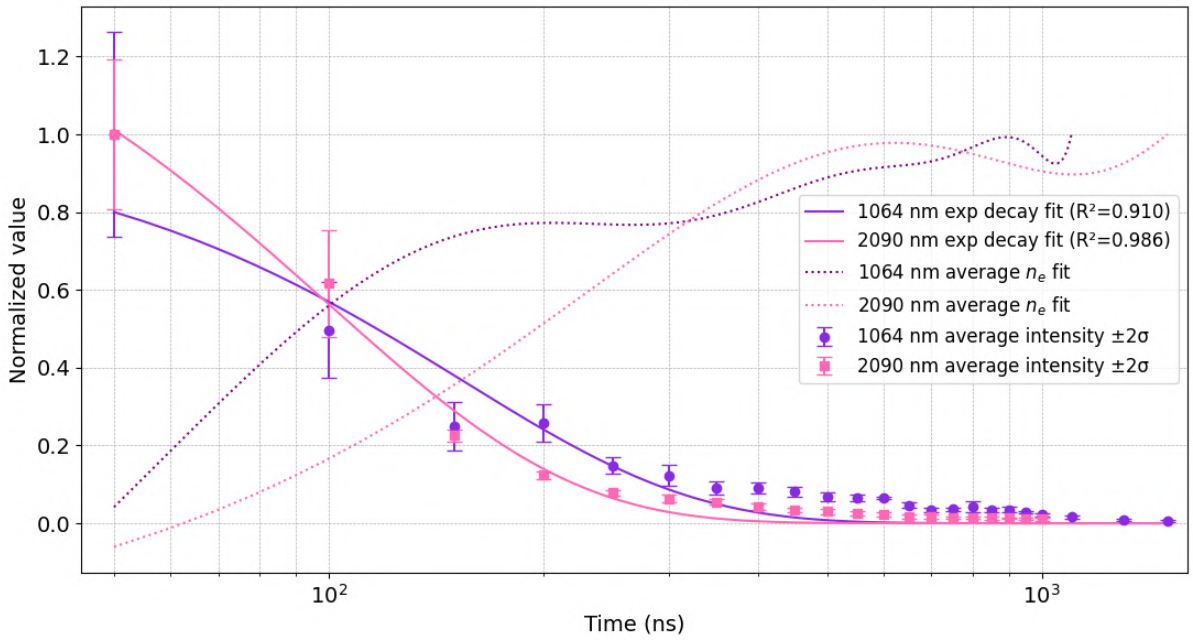

Figure 2.17: Comparison of electron density fit with average integrated spectral intensity normalised for the H6 sample, time axis is $t \in [50, 1500]$ ns

The temporal decay of the normalized integrated intensity was modeled using a stretched exponential $I(t) = A\exp\left[-(t/\tau)^{\beta}\right]$, where A is the amplitude, τ is the characteristic decay time (in nanoseconds), and β is the stretching exponent, which describes the deviation from a single decay time. However, if several mechanisms with different characteristic times contribute, the decay profile broadens, which is reflected by $\beta \neq 1$. The results of this fit are in Table 2.11.

Table 2.11: Stretched-exponential fit parameters for H6 sample at two wavelengths

Wavelength	$\boldsymbol{A}$	$\boldsymbol{\tau}$ (ns)	$\boldsymbol{\beta}$
1064 nm	1	(153.7 ± 10.6)	(1.34 ± 0.19)
2090 nm	(1.55 ± 0.25)	(99.1 ± 15.6)	(1.25 ± 0.22)

To reduce the uncertainty in the τ parameter, the amplitude A was fixed at 1 during the fitting process. The fitted characteristic decay time for the 2090 nm laser is shorter than that of the 1064 nm laser, suggesting a more rapid decrease in intensity. This typically indicates that the plasma has lower energy and extinguishes more quickly. However, this interpretation is not directly supported by the electron density trends: the electron density in Figure 2.14 begins to fall earlier than in Figure 2.15. Still, the faster intensity decay at 2090 nm may be related to reduced electron density overall, as the 1064 nm plasma reaches higher peak electron density. Finally, the shorter decay time may also imply that the plasma generated by the 2090 nm laser has a lower temperature.

In the Supplementary Section, I present the time evolution of unwrapped phase and the reconstructed electron-density maps for a selected subset of data for the H0 sample. The images must be carefully examined, as some of the shapes may be the result of Abel

inversion artifacts, especially in the regions with sudden phase drops.

For the 1064 nm case, the unwrapped phase appears in Figure 4.26, and the corresponding electron density map, taken before the segmentation, in Figure 4.27. These both derive from the raw interferogram shown in Figure 4.25. At the earliest time point (2.1 µs), the reconstruction quality is insufficient to support firm conclusions. However, from 2.1 µs onward, the electron density increases throughout the entire plasma region, peaking at 7 µs. By that moment, two concentric layers have formed: a higher-density inner core surrounded by a slightly less dense outer shell, with the layer boundaries themselves exhibiting the greatest density. At the top of the plasma region, a hydrodynamic fission manifests as a dark band, though phase ambiguity in these data could make it seem like a region with the highest electron density. After this peak, the overall electron density declines, remaining highest at the center and gradually fading toward the edges.

For 2090 nm, the unwrapped phase is in Figure 4.29 and the corresponding electron density in Figure 4.30. The raw interferogram from Figure 4.28 corresponds to those as well. The plasma rapidly gains electron density up till 950 ns without much expanding dynamics. From 950 ns to 1.3 µs, the plasma rapidly expanded, revealing its internal structure. There is only a single layer of plasma, which is denser towards the edges and slightly loses density towards the center. At 1.9 and 2.1 µs, the plasma core disappears, possibly because of the phase ambiguity. The core reappears at a time 2.2 µs, where it beins to have a much more complex shape. The hydrodynamic fission manifests with the highest electron density material trying to leave the plasma. This fission part probably does not have enough energy to leave the plasma (as no Rayleigh-Taylor instability appears), and this density is then redistributed to the edges at times 3 and 5 µs. At later times the plasma plume loses the electron density from the core to the upward direction. It stops changing its shape drastically.

2.8. Discussion and measurement interpretation

The shock wave measurement and electron density results do correspond. Greater speed of the shockwave means more effective ablation, which means greater electron density. Through heat treatment, steel's microstructure traps substantial residual stresses and defects in its crystal lattice. This residual stress energy is likely released with the laser pulse breaking the atomic bonds and contributes to the energy of the shock wave. This means the greater the hardness, the greater the velocity the shock wave should have, which agrees with the 1064 nm measurements. The magnitude of such energy is not negligible. The elastic strain energy density (energy stored per unit volume) in a material under uniaxial stress is given by:

$$U = \frac{\sigma^2}{2E} \left(\frac{\mathrm{J}}{\mathrm{cm}^3} \right) \tag{2.8}$$

where $\sigma \approx 200$ (MPa) is the typical residual stress of heat-treated material, and $E \approx 200$ (GPa) is the typical Young modulus stiffness of steel. This yields $U = 0.1 \left(\frac{\mathrm{J}}{\mathrm{cm}^3}\right)$, which when converted to power density for the energy released during the pulse duration $\Delta t = 5$ ns is $I = 2 \times 10^7 \left(\frac{\mathrm{W}}{\mathrm{cm}^3}\right)$. In comparison to the energy of the pump laser

$I = 4.7 \times 10^{10}$ $\left(\frac{\mathrm{W}}{\mathrm{cm}^2}\right)$ is not a negligible number. Further study is needed to support this hypothesis. The additional released energy also makes ionization easier, contributing to higher electron densities, which again corresponds to the results in both 1064 nm and 2090 nm cases.

The copper (Cu) sample displayed an unexpected outcome. Given Cu's lower melting point (1085°C) compared to steel (approximately 1400°C) and latent heats (205 $(\frac{\mathrm{J}}{\mathrm{g}})$ Cu versus 250 $(\frac{\mathrm{J}}{\mathrm{g}})$ steel), a higher shock wave velocity would be anticipated as more energy should be absorbed in the ablation process. However, the measurements indicate that Cu produced the lowest velocity among all tested materials, as well as the lowest electron density. The result could be explained by its much higher thermal conductivity (400 $(\frac{\mathrm{W}}{\mathrm{m}\cdot\mathrm{K}})$ for Cu versus 50 $(\frac{\mathrm{W}}{\mathrm{m}\cdot\mathrm{K}})$ for steel). Copper's superior conductivity rapidly transports absorbed pulse energy from the surface into the bulk, reducing peak surface temperatures and ablation efficiency, while steel's poorer conductivity confines heat nearer the surface, promoting hotter surface spikes that drive more efficient ablation and ionization. The literature is inconsistent on this matter, and an alternative hypothesis is that steel's substantially higher melting point and greater latent heat of fusion mean that the ablated steel vapor carries more thermal energy into the plasma, driving more extensive ionization and thus yielding a higher electron density. The lower electron density of 2090 nm laser can also be explained by the difference in pump laser wavelength, where simply the 1064 nm photons have greater energy, thus the ionisation is easier.

Electron density is theoretically highest when the plasma first forms, but because the plasma volume is still very small, the limited imaging resolution of the Mach-Zehnder interferometer might be causing an underestimated density calculation. As the plasma expands, the electron density grows. An explanation for this was found in [28] for the measurement found in Figure 2.18. The author says: "The strong monotonous decay of the electron density is accompanied by an increase in the number of iron atoms for delay times up to 5 µs. This increase is mainly fed by recombining iron ions." As this was not the goal of this thesis, further analysis will be needed to confirm such a statement with the presented data. The Figure 2.18 compares the intensity of spectral peaks to electron density calculated from those spectral peaks, meaning a different method of measurement was implemented. The trends of the curves yield very similar results compared to the method used in this thesis. The spectral intensity vanishes completely in a microsecond, while the plasma lifetime is much longer.

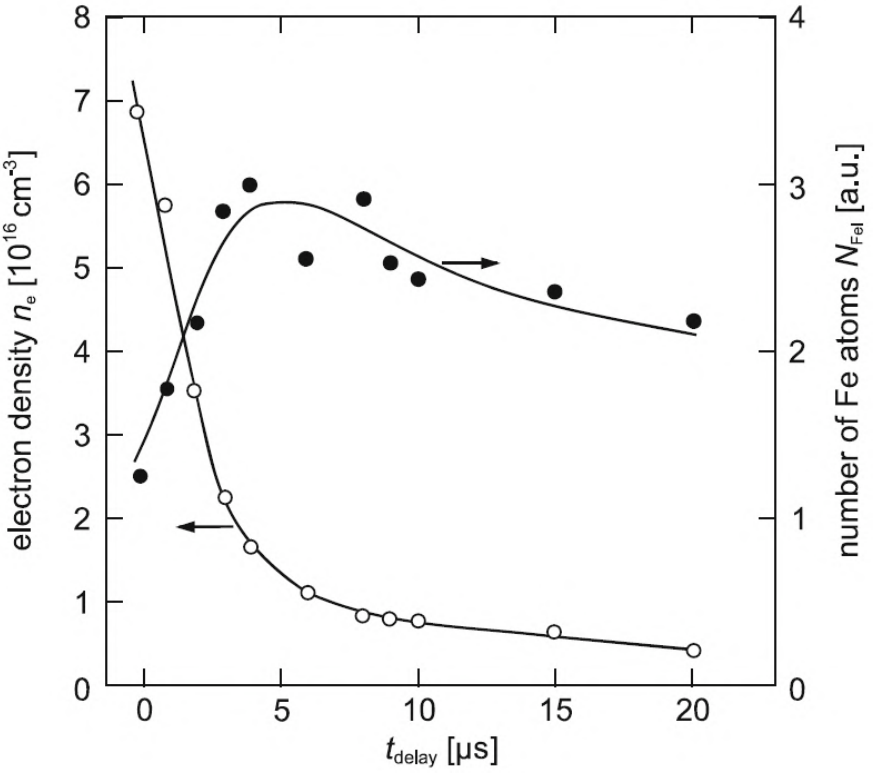

Figure 2.18: Comparison of electron density (black data points) with spectral intensity normalised (white data points) for iron, taken from [28]. The author did not include the laser specifications in the text.

Even though the camera is capturing images with a very short 50 ns exposure, the phase interference is extremely sensitive to sub-wavelength beam path changes, leading to a washout fringe contrast. The data were compromised by blurring caused by vibrations, so a significant number of affected points were excluded from the analysis. Vibrations can arise from building services, foot traffic, and affect the system at low frequencies, which are not damped by the optical table (1-10 Hz). Measurements taken over weekends were slightly less prone to the vibrations. Consequently, specific time window measurements were either entirely omitted or reduced to a smaller sample size, which in turn increased the overall measurement uncertainty.

3. Conclusion

In the theoretical section, I examine various physical characteristics of plasmas and relate them to the behavior of laser-induced plasmas in Laser-Induced Breakdown Spectroscopy. I then introduce the principles of the Mach–Zehnder interferometer and explain the theory behind Abel inversion tomography.

For the experimental work, I integrated a Mach–Zehnder interferometer to LIBS setup, adding a custom beam expander whose lens spacing I optimized to produce a fully collimated probe beam. By minimizing mechanical degrees of freedom and doing a precise alignment, the interferometer achieved long-term stability. Once aligned, it held clear interference fringes for days without further adjustment. Although removing those extra degrees of freedom made the initial alignment challenging, the resulting robustness significantly simplified subsequent measurements.

With the Mach–Zehnder interferometer reliably in place, I performed measurements on copper and on steels of varying Brinell hardness (H0–H6) using two pump wavelengths, 1064 nm and novel 2090 nm under standard laboratory conditions. To the best of our knowledge, the unique 2090 nm pump laser has not been used in any previously published LIBS measurements, as it falls outside its typical wavelength range of 266 - 1064 nm. I examined the resulting ablation craters under a scanning electron microscope to quantify spot size and damage morphology. The laser fluences of the two pump lasers were similar in magnitude, however, their effects on ablation were very different.

The time-resolved interferometric technique proved exceptionally versatile, capturing dynamics from tens of nanoseconds well into the hundreds of microseconds, long after the plasma's own light emission has faded. By recording interferograms at these extended delays, I was able to visualize not only the propagating shock wave but also the hydrodynamic instabilities. Hydrodynamic fission appears in both 1064 nm and 2090 nm experiments shortly after the shock front exits the field of view, and for the 1064 nm shots, Rayleigh–Taylor structures emerge at even later times.

At 1064 nm, the shock wavefront velocity was 224.7 $\frac{\mathrm{m}}{\mathrm{s}}$ for H6 steel and 183.8 $\frac{\mathrm{m}}{\mathrm{s}}$ for H0, providing an independent check on plasma energy via shock-wave analysis. The H6 sample with the higher velocity has a more effective ablation. The shocks produced at 2090 nm were much weaker and too blurry for reliable measurements.

A larger data set consisting of Brinell hardness samples H0, H1, H2, H3, H4, H5, and H6 was measured at 2090 nm wavelength. However, due to the time-intensive nature of the processing, only data for H0, H3, and H6, along with copper, were analyzed. For the 1064 nm wavelength, data were collected only for the H0 and H6 samples due to limited access time with the laser. To manage the large volume of image data, I created an algorithm in the Python programming language that performs plasma electron density reconstruction with minimal manual intervention, as no existing tools offered a fully automated solution for this workflow. The reconstruction process was based on the theoretical understanding of interference and plasma refraction and involved many pre-processing steps. I applied Abel inversion to retrieve the radial change of refractive index profile, and then, through

the Drude model, derived the corresponding electron density maps. One of the main challenges was the lack of clearly defined boundaries in the plasma plume, which made segmentation difficult. While segmentation could theoretically be applied in earlier stages, such as directly on the projection image, it proved more effective after performing Abel inversion and calculating the electron density, where the plasma structure becomes much more distinct and easier to isolate. Background removal played a key role in improving the accuracy of the final plasma segmentation. Although a substantial amount of data points had to be discarded due to loss of Fourier spectra clarity through blurring and segmentation failures, a sufficient number of reconstructions were successful to enable comparison between different materials and excitation wavelengths.

From the segmented plasma electron density map, I calculated the average electron density. Overall, the 1064 nm laser produced higher electron densities than the 2090 nm laser. The maximum electron density was observed at 5 μs, reaching 2.57×10^{17} cm^{-3} for the H6 sample at 1064 nm, compared to 1.94×10^{17} cm^{-3} for the same sample at 2090 nm. Samples with greater hardness exhibited higher electron densities, while copper consistently showed the lowest electron density among all measured materials. The effect of the longer excitation wavelength is evident, as the 1064 nm photons possess higher energy than those at 2090 nm, making ionization more efficient.

The spectral data were used to calculate the integrated average emission intensity and compared with the electron density trends for the steel H6 sample. Using these processed data and comparing them with data from the literature, I proved that the Mach-Zehnder interferometer I built can be used to measure electron density in two dimensions over large time spans and study various spatial plasma effects.

The future development of this work will focus on both experimental and computational improvements. On the experimental side, implementing a pulsed probe laser and a higher-resolution camera might help address issues related to vibrations and producing sufficient data quality. Additionally, a new measurement chamber will be integrated into the LIBS setup, allowing the plasma to be studied under controlled ambient conditions, including different gases and vacuum environments. In terms of data processing, further automation is needed to increase efficiency and data quality. This includes developing a phase-unwrapping validation algorithm to detect and discard flawed reconstructions, as well as an automated blur detection system. Moreover, more advanced segmentation techniques should be explored to better handle the diffuse nature of plasma boundaries. Finally, experimenting with alternative Abel inversion algorithms could lead to improved accuracy and finer spatial resolution in the reconstructed electron density maps.

Literature

[1] KULHÁNEK, Petr. *Úvod do teorie plazmatu*. First. AGA, 2018. ISBN 9788090458222.

[2] ZAJKOV, Oliver. *Video Glow discharge in a low-pressure tube caused by electric current*. 2015.

[3] ATKINS, Peter. *Physical chemistry*. 8th. Oxford University Press, 2006. ISBN 0-7167-8759-8.

[4] NAVE, R. *Phase changes*. 2000. Available also from: http://hyperphysics.phy-astr.gsu.edu/hbase/thermo/phase.html.

[5] LIMPLOUCH, Jiří. *Přednáška základy fyziky plazmatu - Úvod*. 2020. Available also from: http://kfe.fjfi.cvut.cz/~limpouch/plazma/.

[6] CHEN, Francis. *Introduction to Plasma Physics and Controlled Fusion*. Third. Springer, 1984. ISBN 978-3-319-22308-7.

[7] CAPTAIN, Tantan. *Tantan Semiconductor Academy Deposition Process Training 11: "Explain the Debye length"*. 2022. Available also from: https://sshmyb.tistory.com/133.

[8] HARILAL, S. S.; PHILLIPS, M. C.; FROULA, D. H.; ANOOP, K. K.; ISSAC, R. C., et al. Optical diagnostics of laser-produced plasmas. *Reviews of Modern Physics*. 2022, vol. 94. ISSN 15390756. Available from DOI: 10.1103/RevModPhys.94.035002.

[9] SOUBUSTA, Jan. *Fyzika pevných látek*. 1st. Univerzita Palackého v Olomouci, 2012. ISBN 9788024430959. Available also from: http://jointlab.upol.cz/~soubusta/PL/.

[10] SOBUSTA, Jan; ČERNOCH, Antonín. *Optické vlastnosti pevných látek*. Univerzita Palackého v Olomouci, 2022. ISBN 9788024441115.

[11] ELIAS, M.; LAFAIT, J. *La couleur : Lumière, vision et matériaux*. Berlin, 2006. ISBN 2-7011-4192-3.

[12] BORN, Max; WOLF, Emil. *Principles of Optics*. 7th. Cambridge, 1999. ISBN 0521642221.

[13] MIZIOLEK, Andrzej W.; PALLESCHI, Vincenzo; SCHECHTER, Israel. *Laser-Induced Breakdown Spectroscopy (LIBS) Fundamentals and Applications*. Cambridge, 2006. ISBN 978-0-511-24529-9.

[14] HITZ, C. Breck; EWING, J.; HECHT, Jeff. *Introduction to Laser Technology*. 4th. IEEE Press, 2012. ISBN 978-0-470-91620-9.

[15] SINGH, Jagdish P.; THAKUR, Surya N. *Laser-Induced Breakdown Spectroscopy*. 2nd. Ed. by SINGH, Jagdish P.; THAKUR, Surya N. Elsevier, 2020. ISBN 978-0-12-818829-3.

[16] MOHAN, Megha; BUDAY, Jakub; PROCHAZKA, David; GEJDOŠ, Pavel; POŘÍZKA, Pavel, et al. Laser-induced plasma on the boundary of two matrices. *Journal of Analytical Atomic Spectrometry*. 2023, vol. 38, pp. 2433–2440. ISSN 13645544. Available from DOI: 10.1039/d3ja00135k.

[17] CREMERS, David A; RADZIEMSKI, Leon J. *Handbook of Laser-Induced Breakdown Spectroscopy*. John Wiley and Sons, Ltd, 2013. ISBN 9781119971122.

[18] RUSSO, Richard E.; MAO, Xianglei; GONZALEZ, Jhanis J.; ZORBA, Vassilia; YOO, Jong. Laser ablation in analytical chemistry. *Analytical Chemistry*. 2013, vol. 85, pp. 6162–6177. ISSN 00032700. Available from DOI: 10.1021/ac4005327.

[19] PHIPPS, Claude. *Laser ablation and its Applications*. Springer, 2007. ISBN 978-0387-30452-6.

[20] LEITZ, Karl Heinz; REDLINGSHÖER, Benjamin; REG, Yvonne; OTTO, Andreas; SCHMIDT, Michael. Metal ablation with short and ultrashort laser pulses. In: *Physics Procedia*. Elsevier B.V., 2011, vol. 12, pp. 230–238. ISSN 18753892. Available from DOI: 10.1016/j.phpro.2011.03.128.

[21] VERHOFF, B.; HARILAL, S. S.; FREEMAN, J. R.; DIWAKAR, P. K.; HASSANEIN, A. Dynamics of femto- and nanosecond laser ablation plumes investigated using optical emission spectroscopy. *Journal of Applied Physics*. 2012, vol. 112. ISSN 00218979. Available from DOI: 10.1063/1.4764060.

[22] HUMPHREY, Nathan; VOLKOV, Alexey N. Hydrodynamic splitting of laser-induced plasma plumes: two-dimensional kinetic simulations. *Applied Physics A: Materials Science and Processing*. 2022, vol. 128. ISSN 14320630. Available from DOI: 10.1007/s00339-022-05790-9.

[23] WANI, Rauoof; MIR, Ajaz; BATOOL, Farida; TIWARI, Sanat. Rayleigh–Taylor instability in strongly coupled plasma. *Scientific Reports*. 2022, vol. 12. ISSN 20452322. Available from DOI: 10.1038/s41598-022-15725-2.

[24] LEI, Wenqi. *Temporal and spatial characteristics of laser-induced plasma on organic materials and quantitative analysis of the contained inorganic elements*. 2012. Available also from: https://www.researchgate.net/publication/278644890. PhD thesis. East China Normal University.

[25] LAHAYE, Nicole L.; HARILAL, Sivanandan S.; DIWAKAR, Prasoon K.; HASSANEIN, Ahmed. The effect of laser pulse duration on ICP-MS signal intensity, elemental fractionation, and detection limits in fs-LA-ICP-MS. *Journal of Analytical Atomic Spectrometry*. 2013, vol. 28, pp. 1781–1787. ISSN 02679477. Available from DOI: 10.1039/c3ja50200g.

[26] GAMALY, E. G.; RODE, A. V.; LUTHER-DAVIES, B.; TIKHONCHUK, V. T. Ablation of solids by femtosecond lasers: Ablation mechanism and ablation thresholds for metals and dielectrics. *Physics of Plasmas*. 2002, vol. 9, p. 949. ISSN 1070664X. Available from DOI: 10.1063/1.1447555.

[27] GUO, Baoshan; SUN, Jingya; HUA, Yanhong; ZHAN, Ningwei; JIA, Jingang, et al. *Femtosecond Laser Micro/Nano-manufacturing: Theories, Measurements, Methods, and Applications*. Vol. 3. Springer Science and Business Media B.V., 2020. ISSN 2520811X. Available from DOI: 10.1007/s41871-020-00056-5.

[28] NOLL, Reinhard. *Laser-Induced Breakdown Spectroscopy: Fundamentals and Applications*. Springer, 2012. ISBN 978-3-642-20667-2.

[29] CRISTOFORETTI, G.; GIACOMO, A. De; DELL'AGLIO, M.; LEGNAIOLI, S.; TOGNONI, E., et al. Local Thermodynamic Equilibrium in Laser-Induced Breakdown Spectroscopy: Beyond the McWhirter criterion. *Spectrochimica Acta - Part B Atomic Spectroscopy*. 2010, vol. 65, pp. 86–95. ISSN 05848547. Available from DOI: 10.1016/j.sab.2009.11.005.

[30] SHABANOV, S. V.; GORNUSHKIN, I. B. Modeling chemical reactions in laser-induced plasmas. *Applied Physics A: Materials Science and Processing*. 2015, vol. 121, pp. 1087–1107. ISSN 14320630. Available from DOI: 10.1007/s00339-015-9445-0.

[31] GALBÁCS, Gábor. *Laser-Induced Breakdown Spectroscopy in Biological, Forensic and Materials Sciences*. Ed. by GALBÁCS, Gábor. Springer International Publishing, 2022. ISBN 9783031145025. Available from DOI: 10.1007/978-3-031-14502-5.

[32] KRAMIDA, A.; OLSEN, K.; RALCHENKO, Y. *NIST LIBS Database*. [N.d.]. Available also from: https://physics.nist.gov/PhysRefData/ASD/LIBS/libs-form.html.

[33] HARIHARAN, P. *Basics of Interferometry*. Second. Academic press, School of Physics, University ofSydney, 2007. ISBN 978-0-12-373589-8.

[34] BASS, Michael. *Handbook of Optics, Volume I - Fundamentals, Techniques, and Design*. Vol. 1. Second. Ed. by BASS, Michael; STRYLAND, W. Eric Van; WILLIAMS, R. David; WOLFE, L. William. R . R . Donnelly and Sons Company, 1995. ISBN 0-07-047740-7.

[35] CAO, Shiquan; SU, Maogen; MIN, Qi; SUN, Duixiong; MA, Pengpeng, et al. Dynamics and density distribution of laser-produced Al plasmas using optical interferometry and optical emission spectroscopy. *Journal of Quantitative Spectroscopy and Radiative Transfer*. 2019, vol. 225, pp. 69–75. ISSN 00224073. Available from DOI: 10.1016/j.jqsrt.2018.12.029.

[36] OPTICS, Edmund. *Building a Mach-Zehnder Interferometer*. [N.d.]. Available also from: https://www.edmundoptics.com/knowledge-center/application-notes/optomechanics/building-a-mach-zehnder-interferometer/.

[37] DEANS, Stanley Roderick. *The Radon Transform and Some of Its Applications-Wiley*. John Wiley and Sons, Inc., 1983. ISBN 0-471-89804.

[38] GONZALEZ, Rafael C.; WOODS, Richard E. *Digital Image Processing*. 2nd ed. Prentice Hall, 2002. ISBN 0-201-18075-8.

[39] KALENSKÁ, Petra; DRUCKMÜLLEROVÁ, Hana. *Numerical Methods of Image Analysis*. 2024.

[40] TAKEDA, Mitsuo; INA, Hideki; KOBAYASHI, Seiji. Fourier-transform method of fringe-pattern analysis for computer-based topography and interferometry. *J. Opt. Soc. Am.* 1982, vol. 72, pp. 156–160. Available from DOI: https://doi.org/10.1364/JOSA.72.000156.

[41] ALEXANDER, Poularikas D. *The transforms and applications handbook*. 2nd ed. Ed. by RICHARD, Dorf C. IEEE Press, CRC Press, 2000. ISBN 0-8493-8595-4.

[42] ZHANG, Linan; SCHAEFFER, Hayden. *Stability and Error Estimates of BV Solutions to the Abel Inverse Problem*. 2017.

[43] ALVAREZ, R; RODERO, A; QUINTERO, M C. An Abel inversion method for radially resolved measurements in the axial injection torch. *Spectrochimica Acta Part B*. 2002, vol. 57, pp. 1665–1680.

[44] NILSSON, Sebastian; SANNED, David; ROTH, Adrian; SUN, Jinguo; BERROCAL, Edouard, et al. Holistic analysis of a gliding arc discharge using 3D tomography and single-shot fluorescence lifetime imaging. *Communications Engineering*. 2024, vol. 3. ISSN 27313395. Available from DOI: 10.1038/s44172-024-00250-z.

[45] KÉPEŠ, Erik; GORNUSHKIN, Igor; POŘÍZKA, Pavel; KAISER, Jozef. Tomography of double-pulse laser-induced plasmas in the orthogonal geometry. *Analytica Chimica Acta*. 2020, vol. 1135, pp. 1–11. ISSN 18734324. Available from DOI: 10.1016/j.aca.2020.06.078.

[46] WHITAKER, Benjamin. *Imaging in Molecular Dynamics Technology and Applications*. Ed. by WHITAKER, Benjamin. Cambridge, 2003. ISBN 978-0-511-06427-2.

[47] HICKSTEIN, Daniel D.; GIBSON, Stephen T.; YURCHAK, Roman; DAS, Dhrubajyoti D.; RYAZANOV, Mikhail. A direct comparison of high-speed methods for the numerical Abel transform. *Review of Scientific Instruments*. 2019, vol. 90. ISSN 10897623. Available from DOI: 10.1063/1.5092635.

[48] BRANDI, Fernando; GIZZI, Leonida Antonio. Optical diagnostics for density measurement in high-quality laser-plasma electron accelerators. *High Power Laser Science and Engineering*. 2019, vol. 7. ISSN 20523289. Available from DOI: 10.1017/hpl.2019.11.

[49] AREVALLILLO HERRÁEZ, Miguel; BURTON, David R.; LALOR, Michael J.; GDEISAT, Munther A. Fast two-dimensional phase-unwrapping algorithm based on sorting by reliability following a noncontinuous path. *Applied Optics*. 2002, vol. 41, no. 35, pp. 7437–7444. Available from DOI: 10.1364/AO.41.007437.

4. Supplementary data

4.1. Image processing

Figure 4.1: Raw interferogram reference and plasma image.

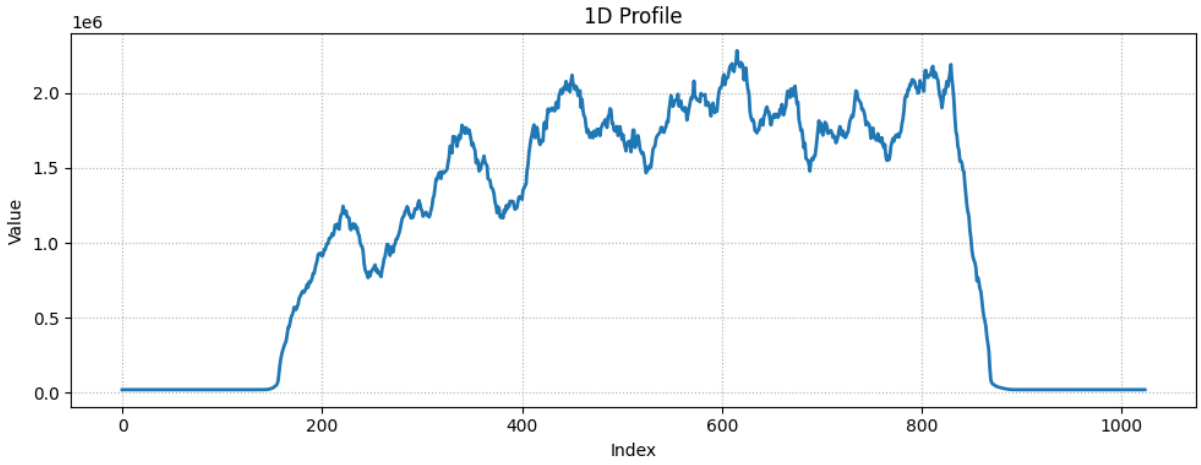

Figure 4.2: Example of a sum of intensities in the vertical direction for the automatic cropping process.

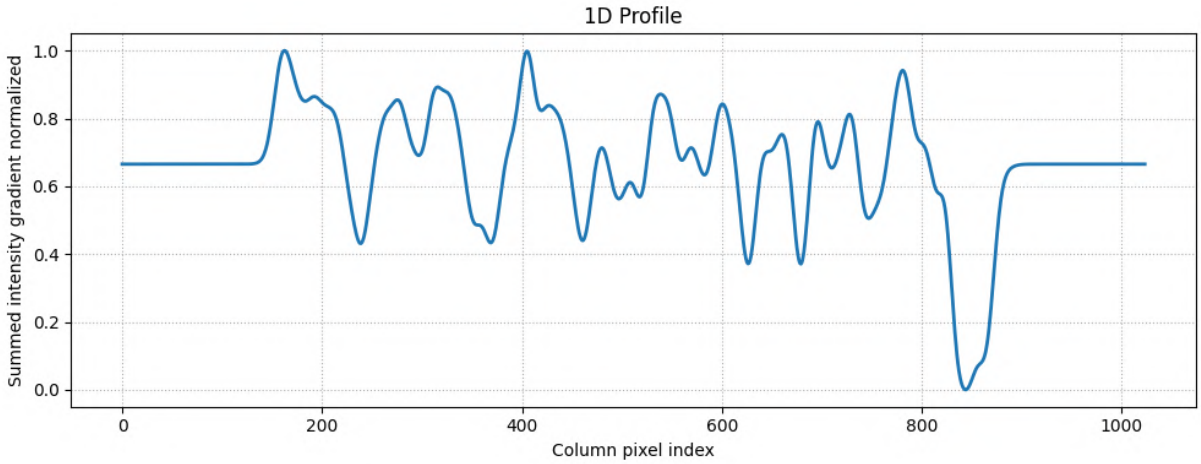

Figure 4.3: Calculated profile gradient from smoothed data in Figure 4.2

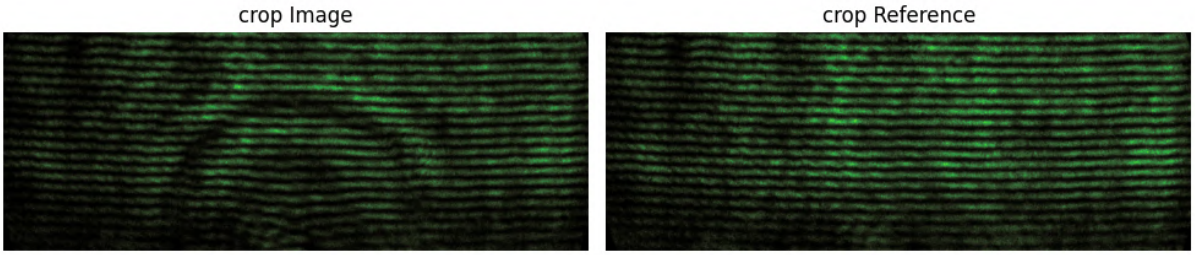

Figure 4.4: Cropped interferogram of reference and plasma.

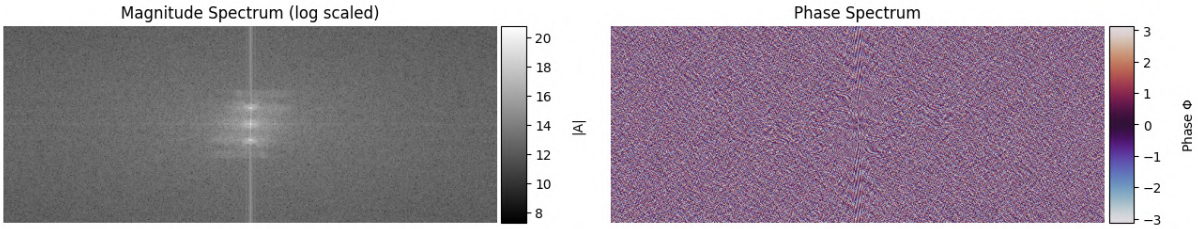

Figure 4.5: Spectrum of a plasma interferogram

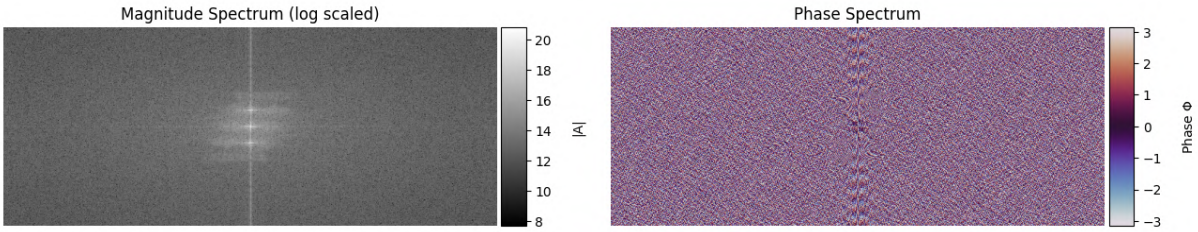

Figure 4.6: Spectrum of a reference interferogram

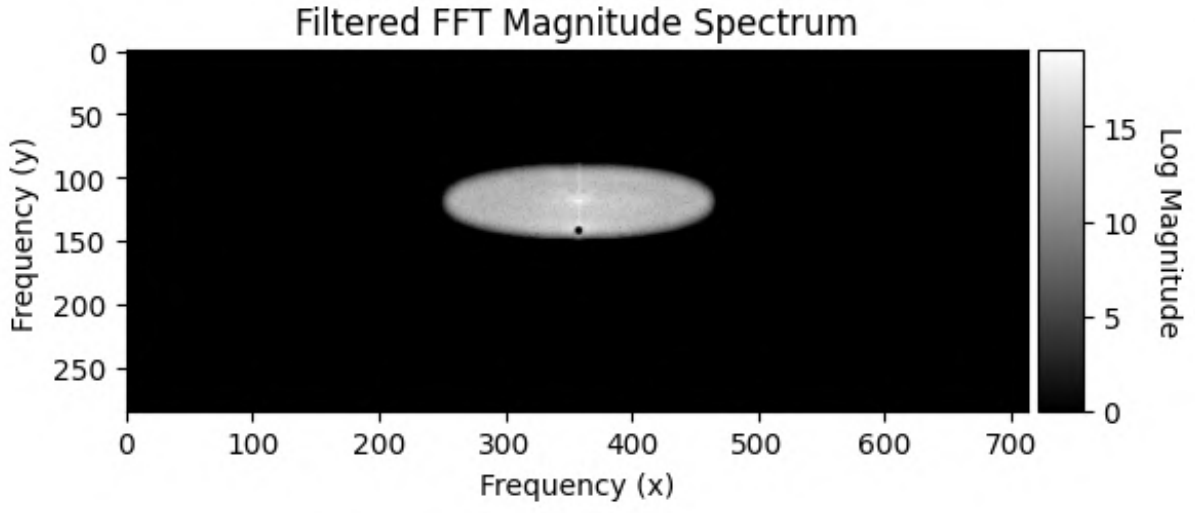

Figure 4.7: Plasma interferogram masked spectrum

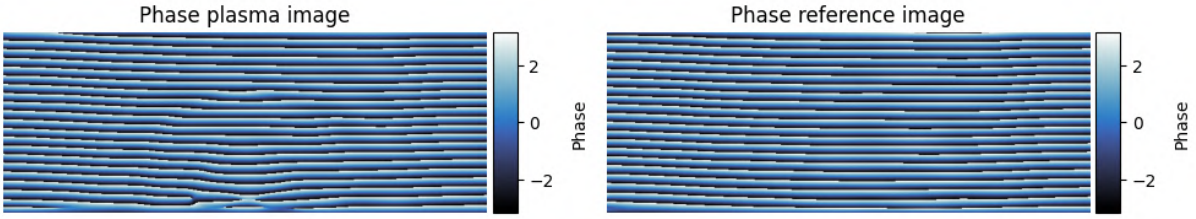

Figure 4.8: Phase map retrieved from the diffraction term.

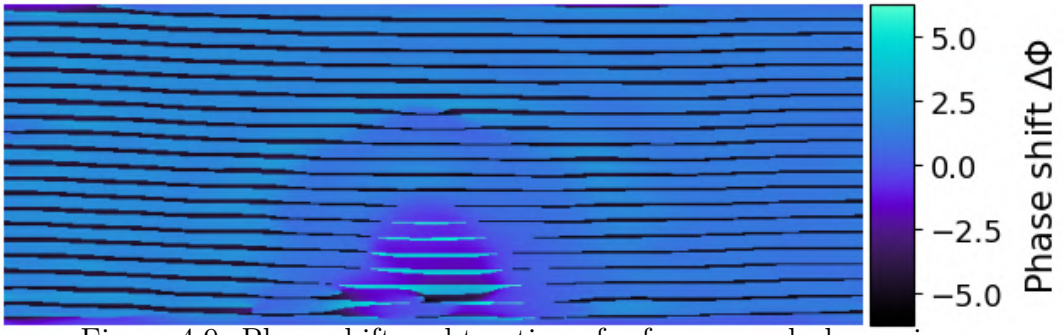

Figure 4.9: Phase shift: subtraction of reference and plasma image

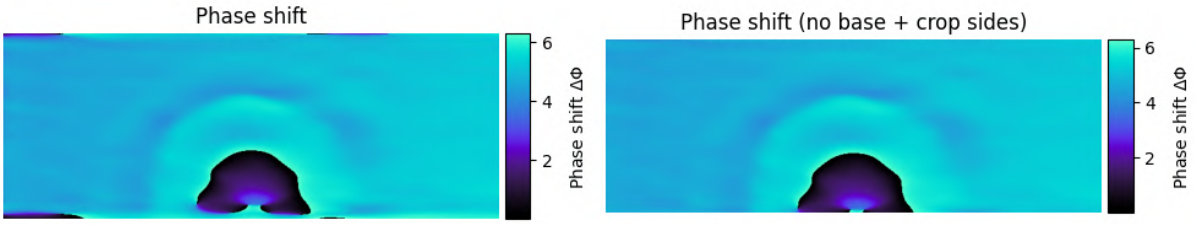

Figure 4.10: Phase shift modulo 2π

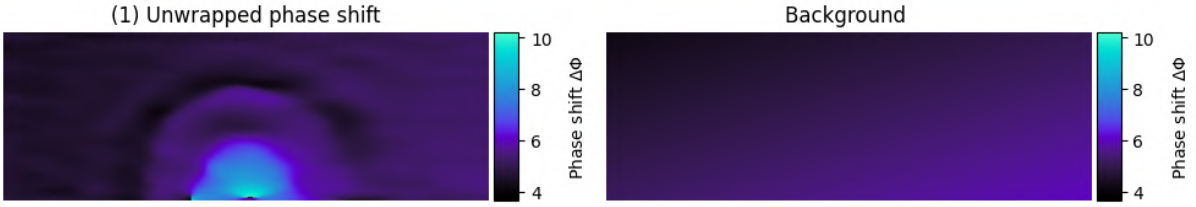

Figure 4.11: (1) Unwrapped phase with background removed

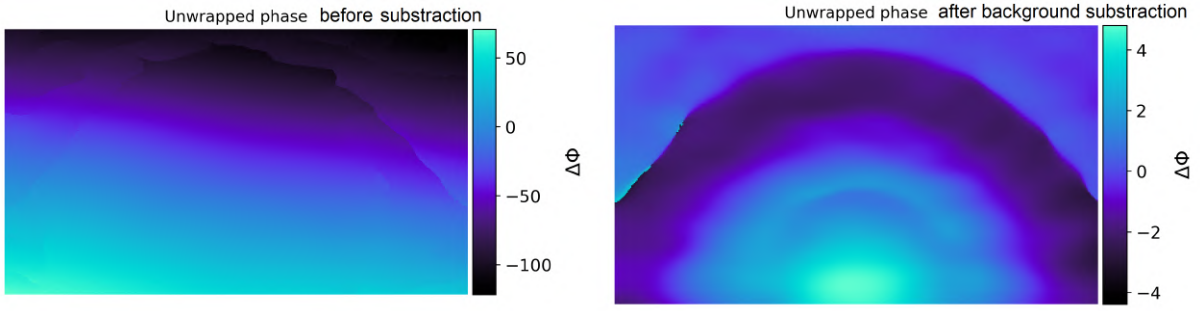

Figure 4.12: Unwrapped phase with background removed, which revealed the plasma structure

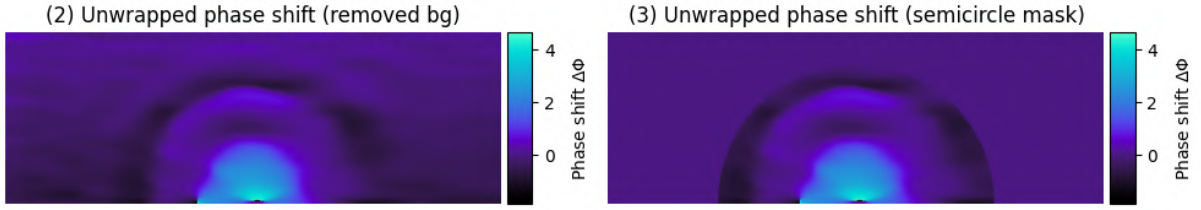

Figure 4.13: (2) Unwrapped phase with removed background and (3) masked with a semicircle mask

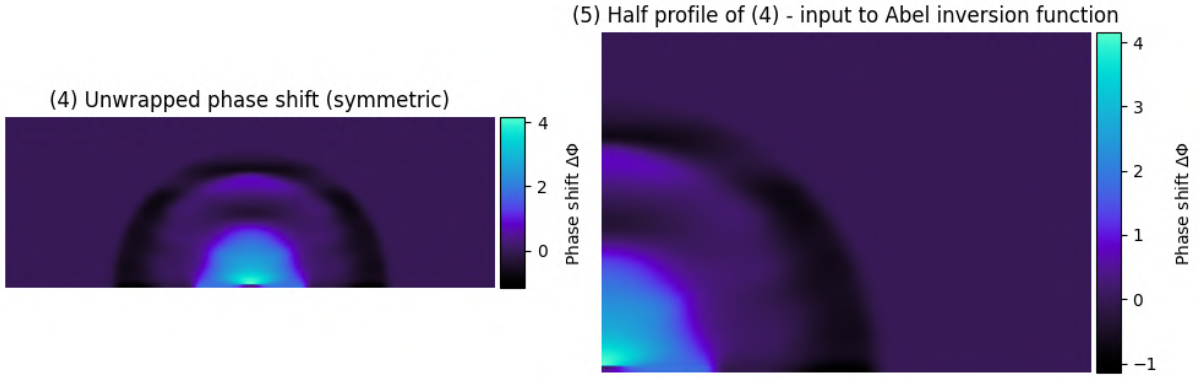

Figure 4.14: (4) Symmetrized unwrapped phase, where the (5) is the input halved image to the Abel inversion method.

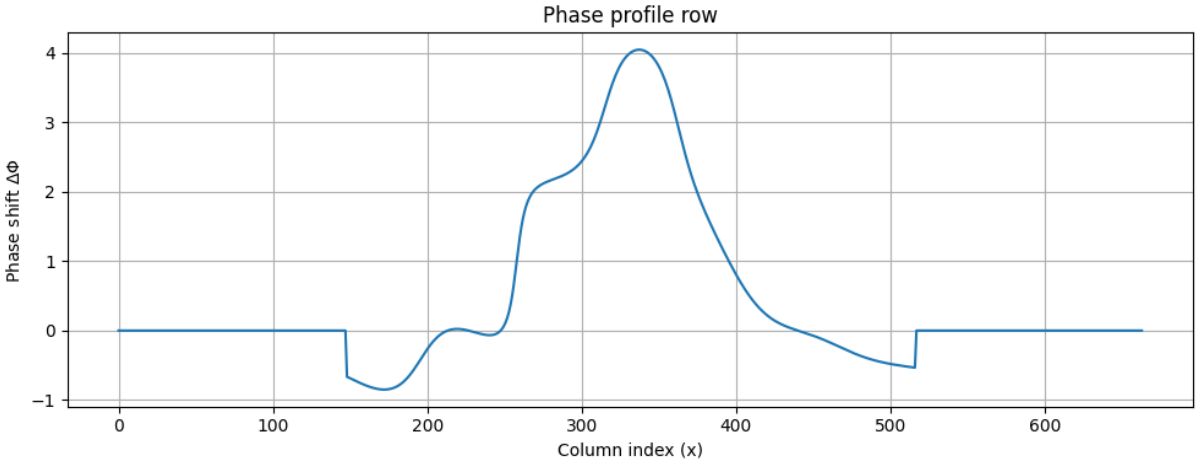

Figure 4.15: Phase shift 1D profile slice

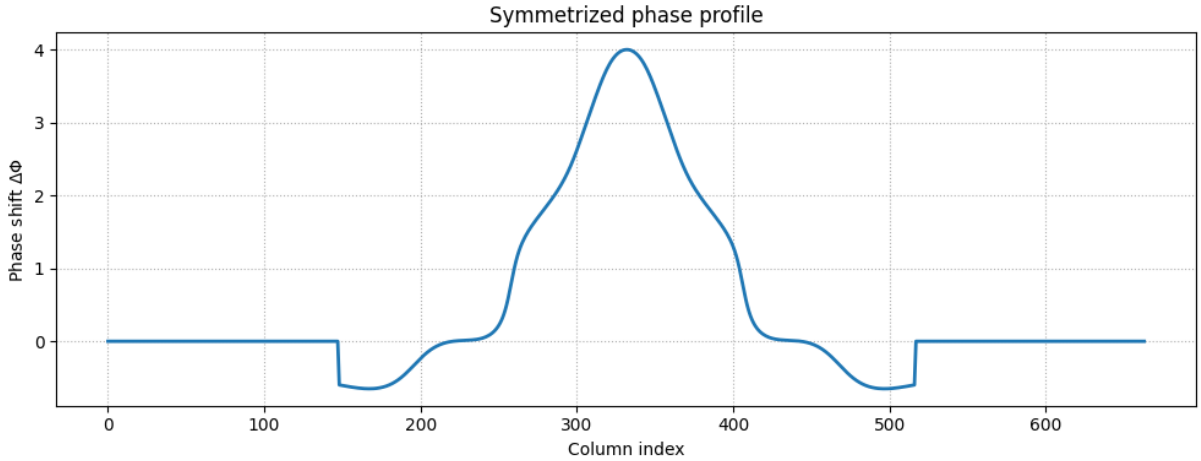

Figure 4.16: Phase shift 1D profile symmetrized

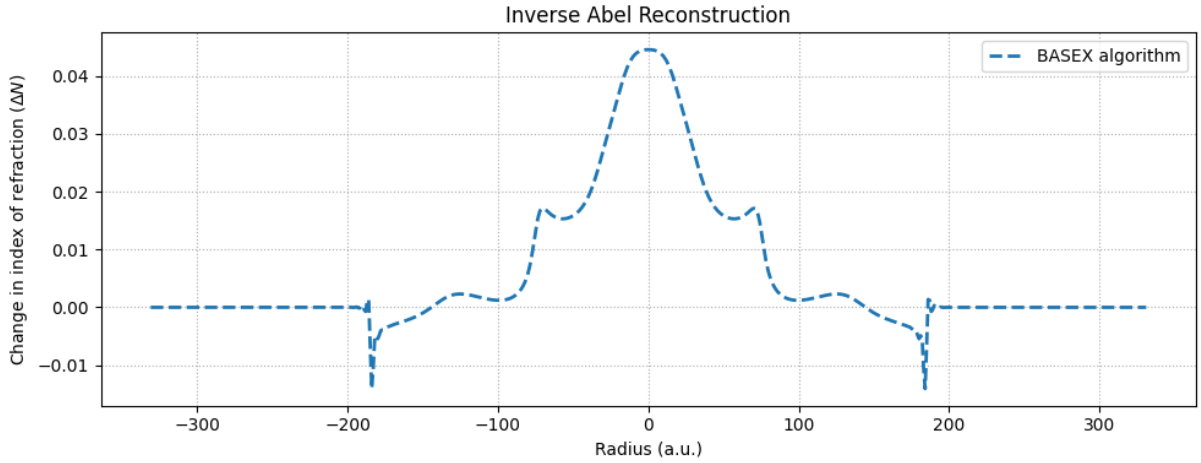

Figure 4.17: Abel inversion of 1D profile, resulting in change of index of refraction profile

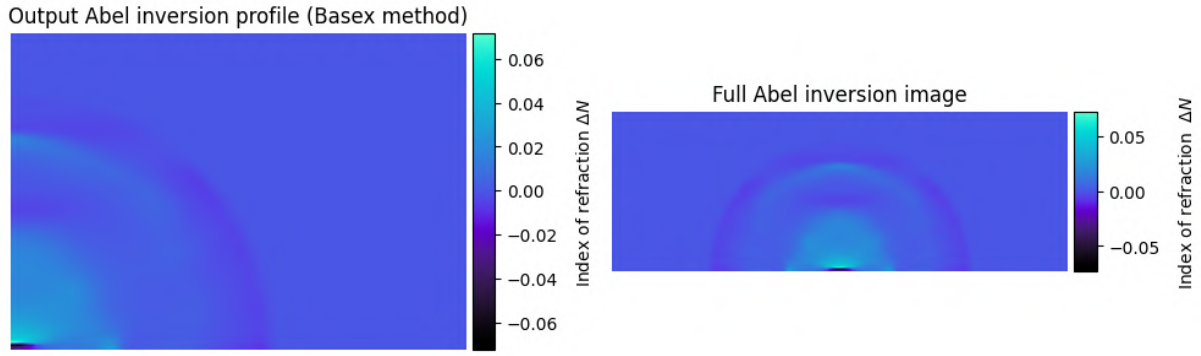

Figure 4.18: Abel inversion (left) output from the function, (right) symmetrized profile. Inversion returned the map of change of index of refraction

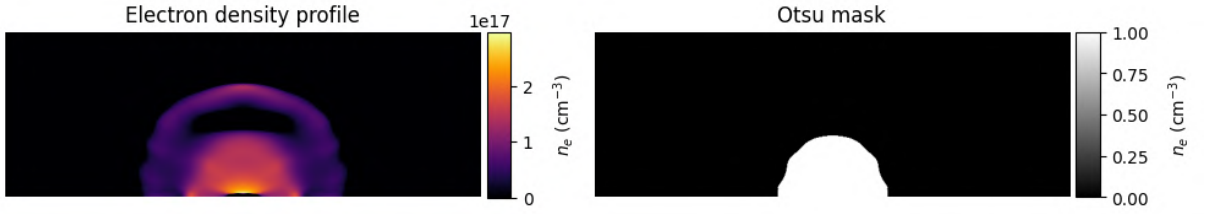

Figure 4.19: Election density profile (left) with a segmentation mask (right)

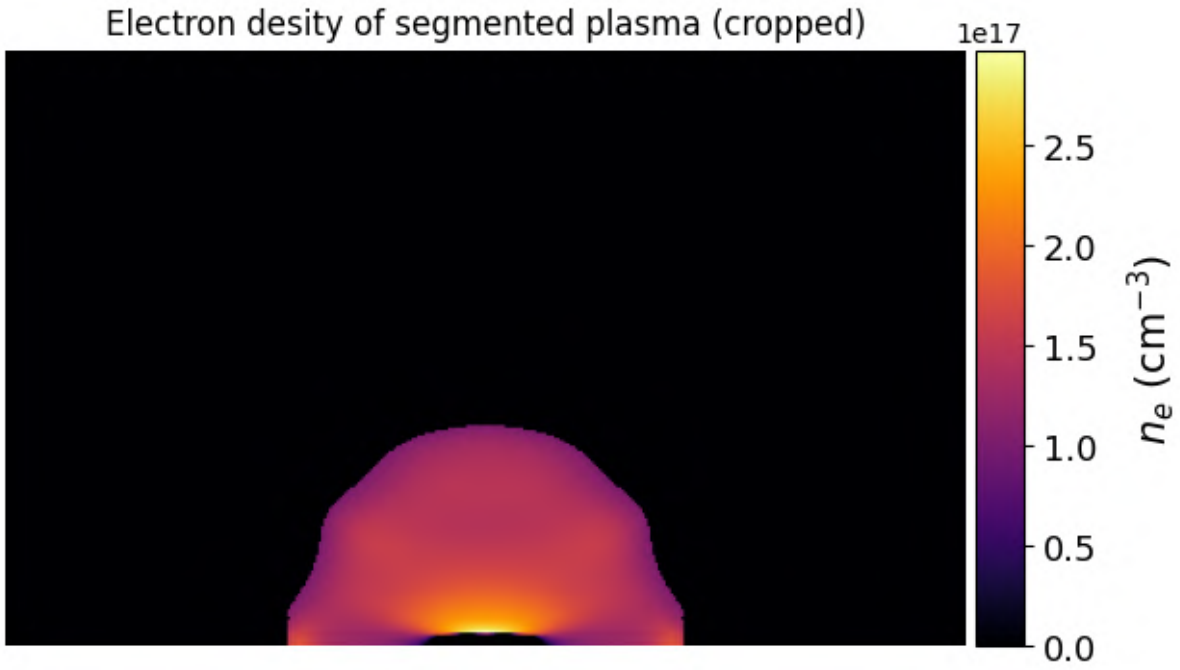

Figure 4.20: segmented Election density profile

4.2. Challenges in image processing

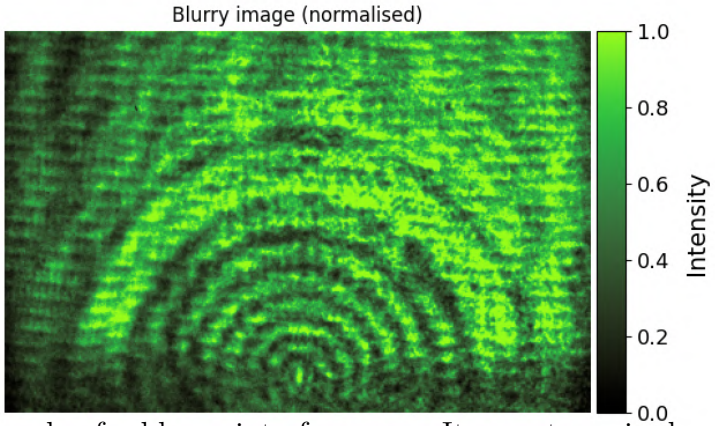

Figure 4.21: Example of a blurry interferogram. Its spectrum is shown in Figure 4.22.

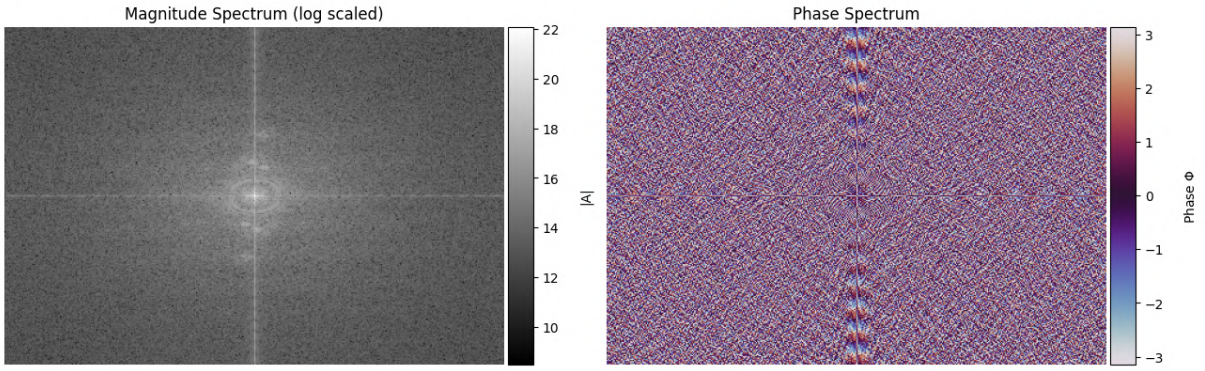

Figure 4.22: Spectrum of a blurry interferogram

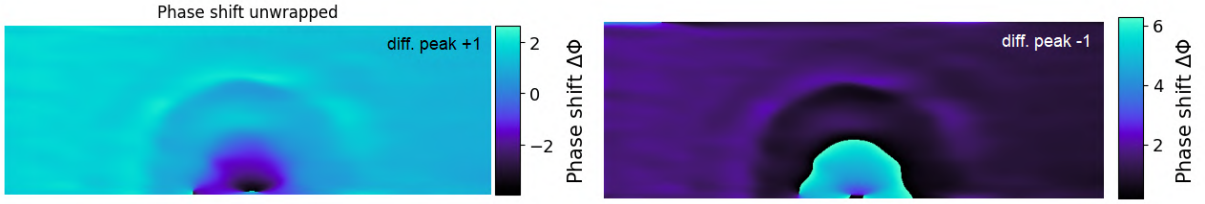

Figure 4.23: Unwrapped phase reconstructed for +1 and -1 diffraction peaks.

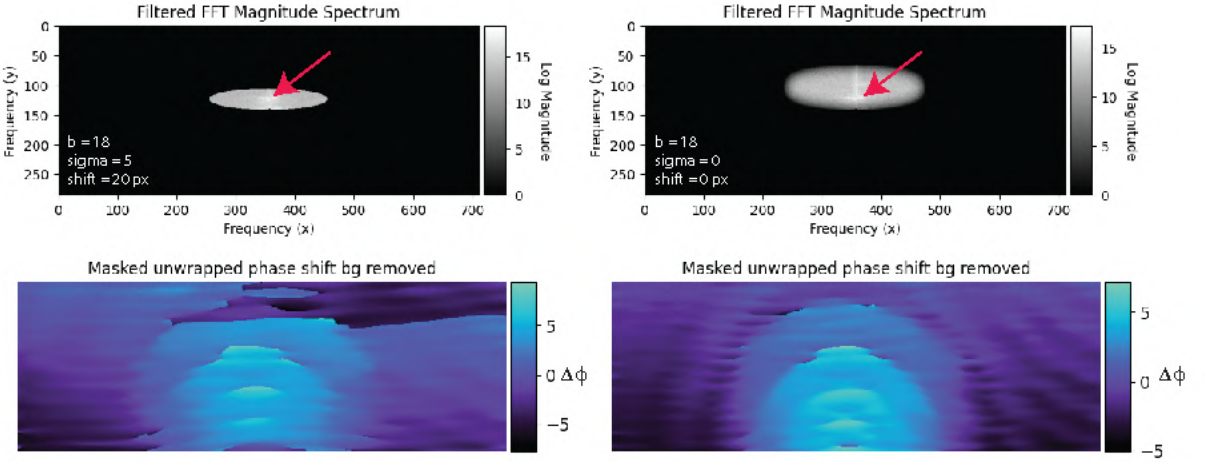

Figure 4.24: Comparison of reconstructed unwrapped phase with greater ellipse radius to a smaller radius, where loss of frequencies occurs.

Table 4.1: Parameter settings for H0 and H6 over different time data sets for 1064 nm laser. Peak shift has been done on all data by 20 px.

	50–1000 ns	1.1–2.1 µs	2.2–5 µs	6–15 µs
H0				
Mask gauss σ	5	5	1	3
Remove tilt	no	yes	no	yes
Smooth profile σ	5	1	0	0
Segmentation method	radius mask	radius mask	Otsu	Multiotsu
H6				
Mask gauss σ	1	5	5	5
Remove tilt	no	yes	yes	yes
Smooth profile σ	5	1	5	0
Segmentation method	radius mask	radius mask	Multiotsu	Multiotsu

Table 4.2: Parameter settings for Cu, H0, H3 and H6 over different time data sets for 2090 nm laser. Peak shift has not been done for any data, and subtraction of tilt was done on all data.

	50–1000 ns	1.1–2.1 µs	2.2–5 µs	6–15 µs
Cu				
Mask gauss σ	1	1	3	3
Smooth profile σ	0	0	1	1
Method for mask	radius mask	non-zero mask	radius mask	Multiotsu
H0				
Mask gauss σ	1	1	2	2
Smooth profile σ	0	0	3	1
Method for mask	non-zero mask	non-zero mask	radius mask	radius mask
H3				
Mask gauss σ	2	1	2	2
Smooth profile σ	0	0	0	0
Method for mask	non-zero mask	Multiotsu	radius mask	non-zero mask
H6				
Mask gauss σ	2	1	1	2
Smooth profile σ	1	1	0	1
Method for mask	non-zero mask	Multiotsu	radius mask	non-zero mask

4.3. Time-resolved image data

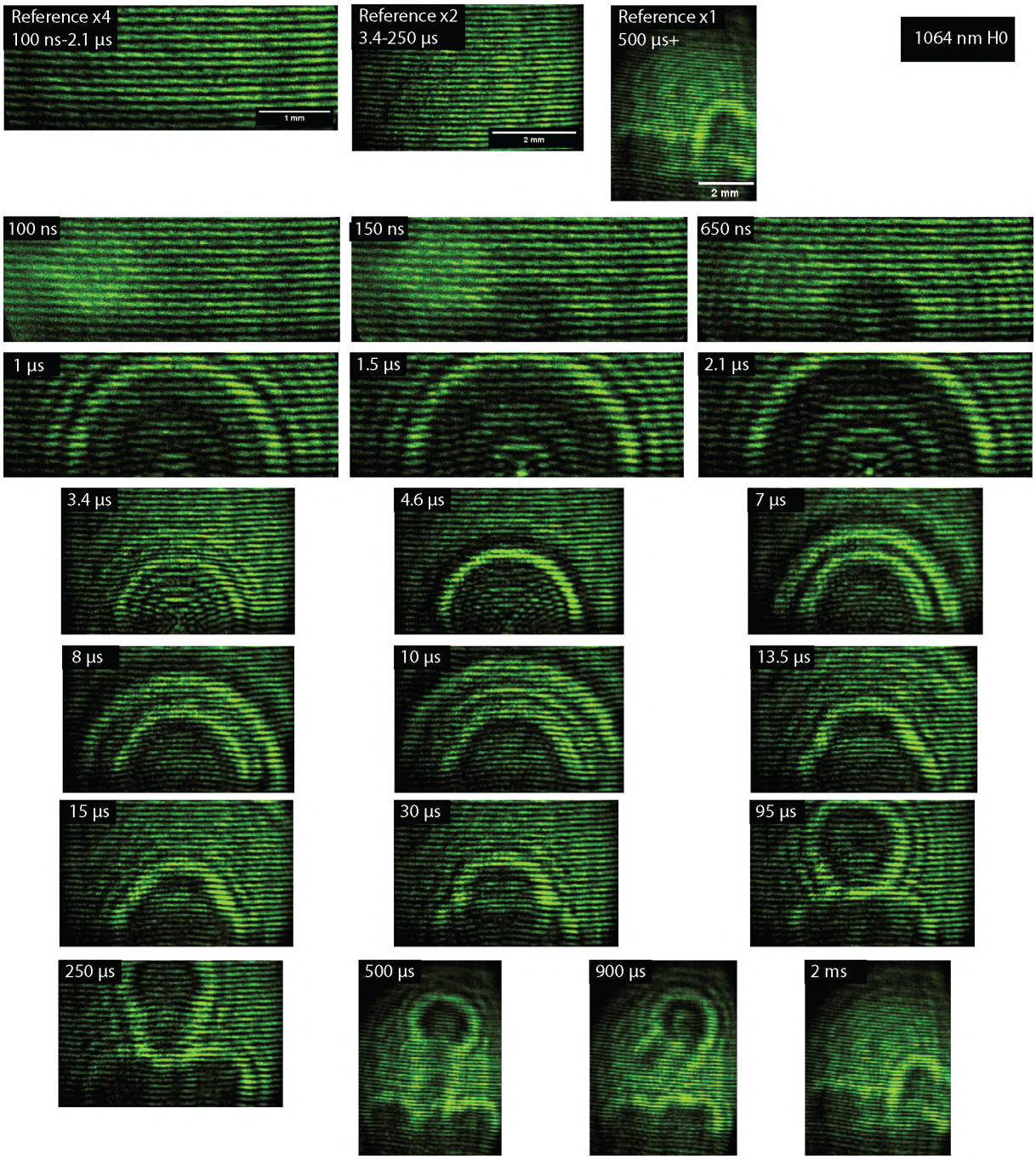

Figure 4.25: Selection of interferograms for 1064 nm H0. The image is normalised to the interval (0,1), and gamma correction 1.5 is used to enhance contrast.

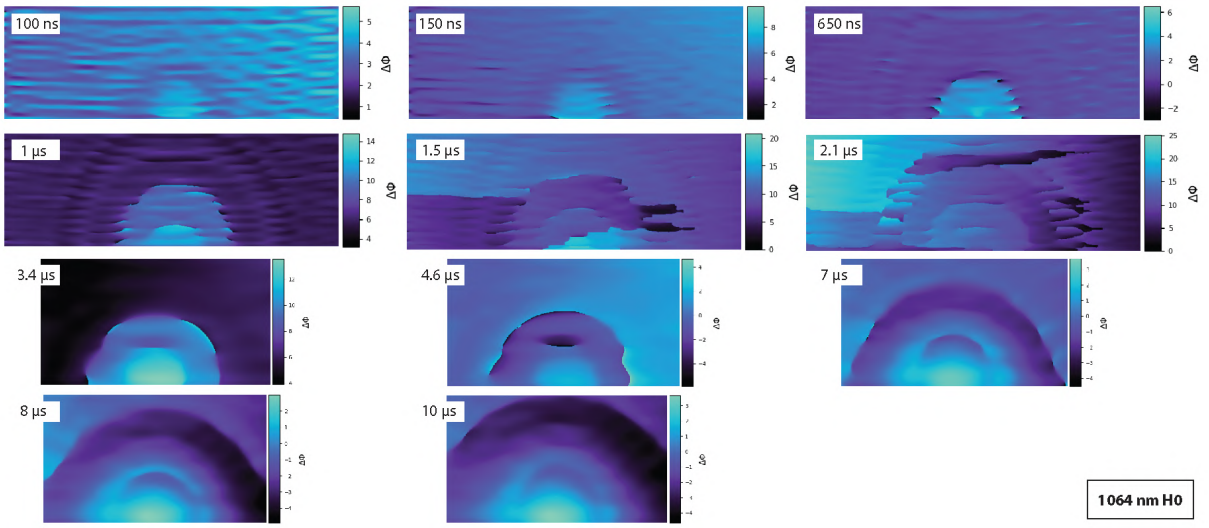

Figure 4.26: Unwrapped phase for 1064 nm H0 (no base)

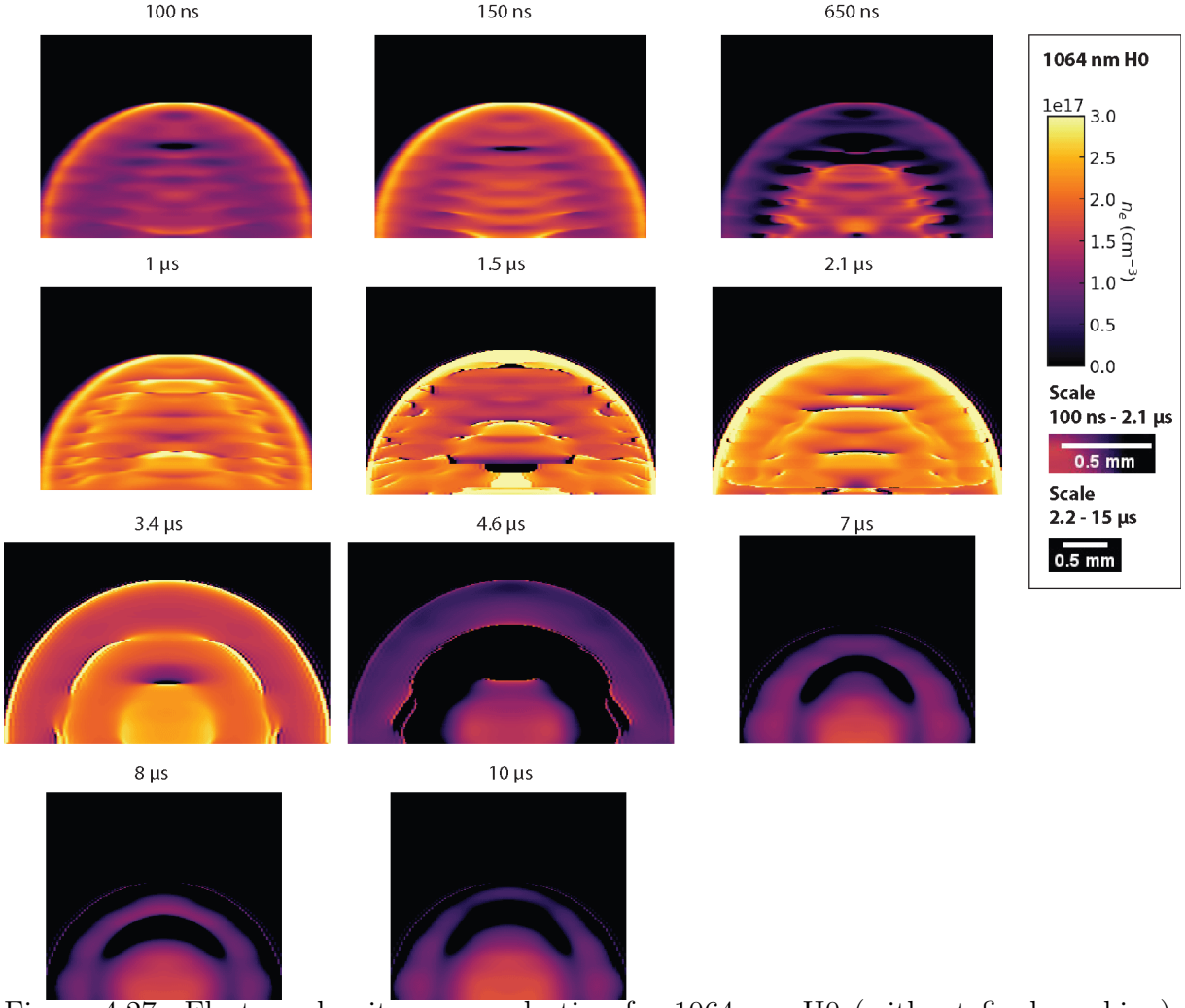

Figure 4.27: Electron density maps selection for 1064 nm H0 (without final masking). Calculated from unwrapped phase from Figure 4.26

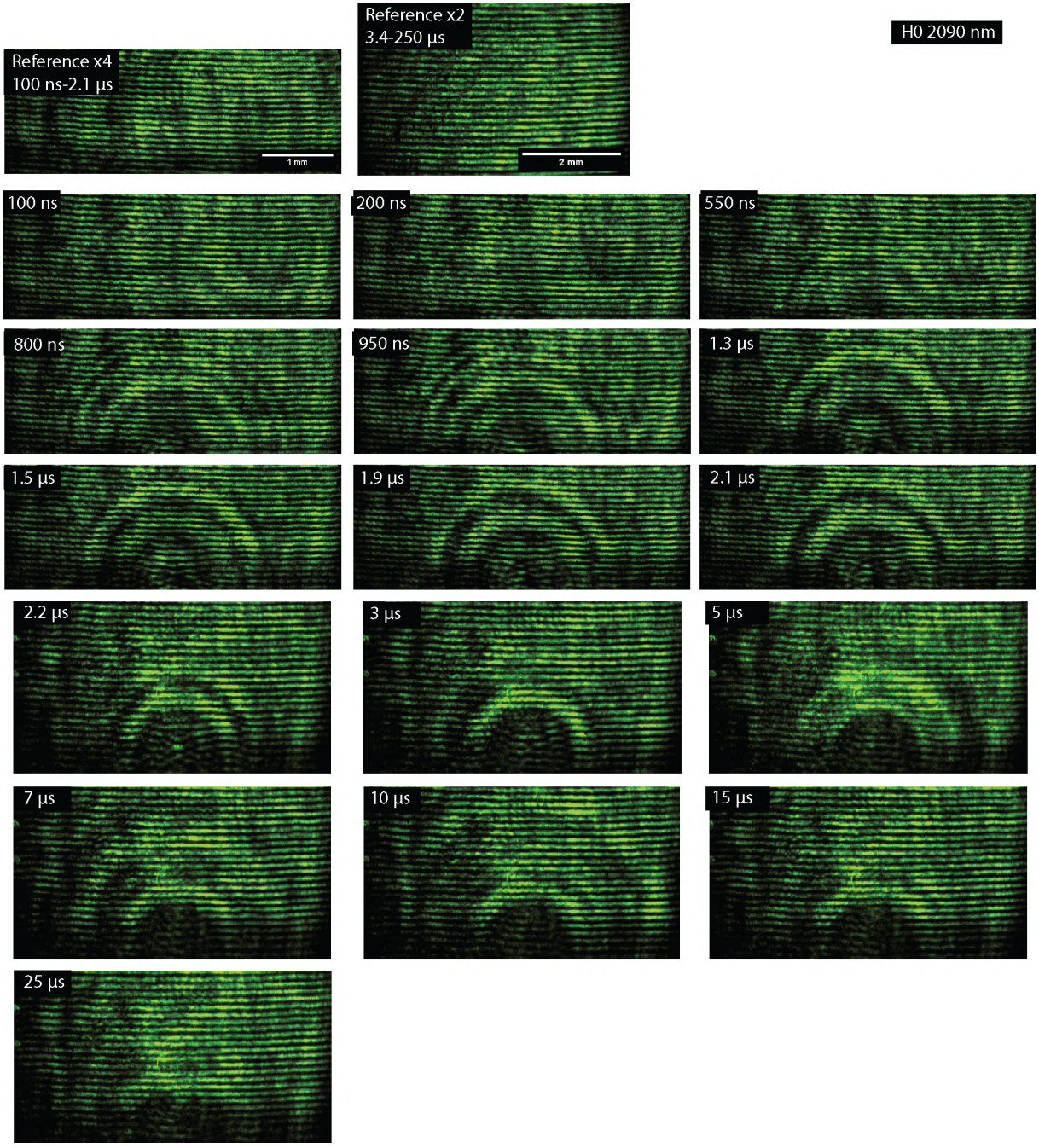

Figure 4.28: Selection of interferograms for 2090 nm H0. The image is normalised to the interval (0,1), and gamma correction 1.5 is used to enhance contrast.

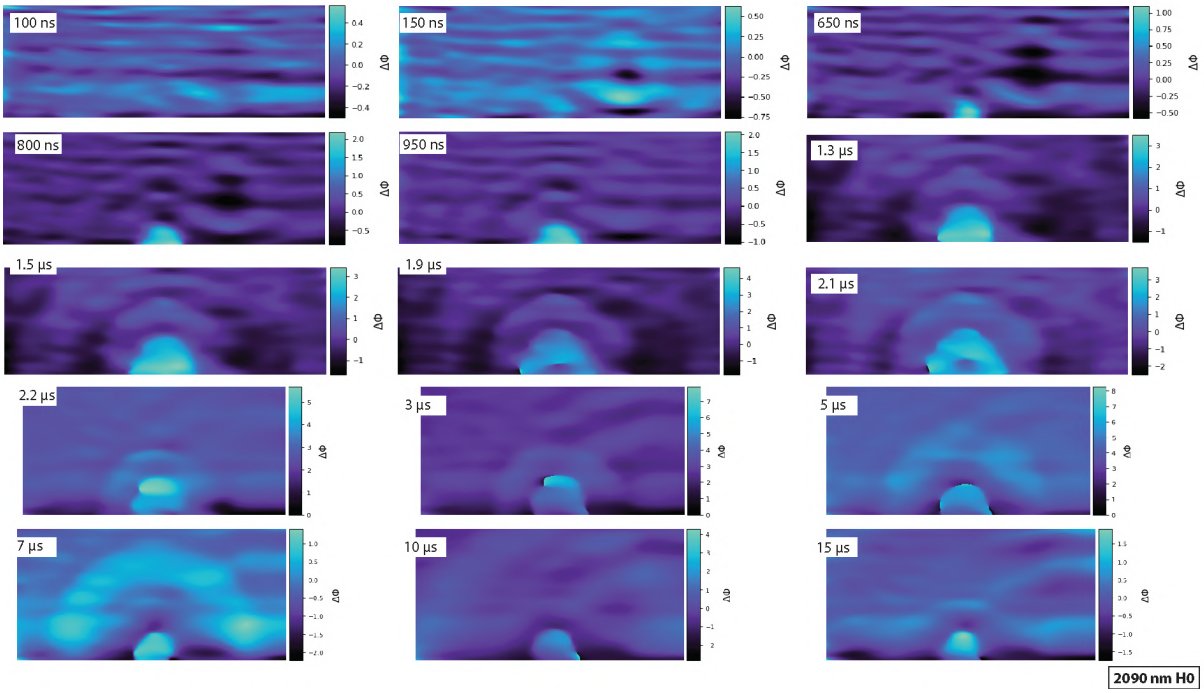

Figure 4.29: Unwrapped phase for 2090 nm H0 (no base)

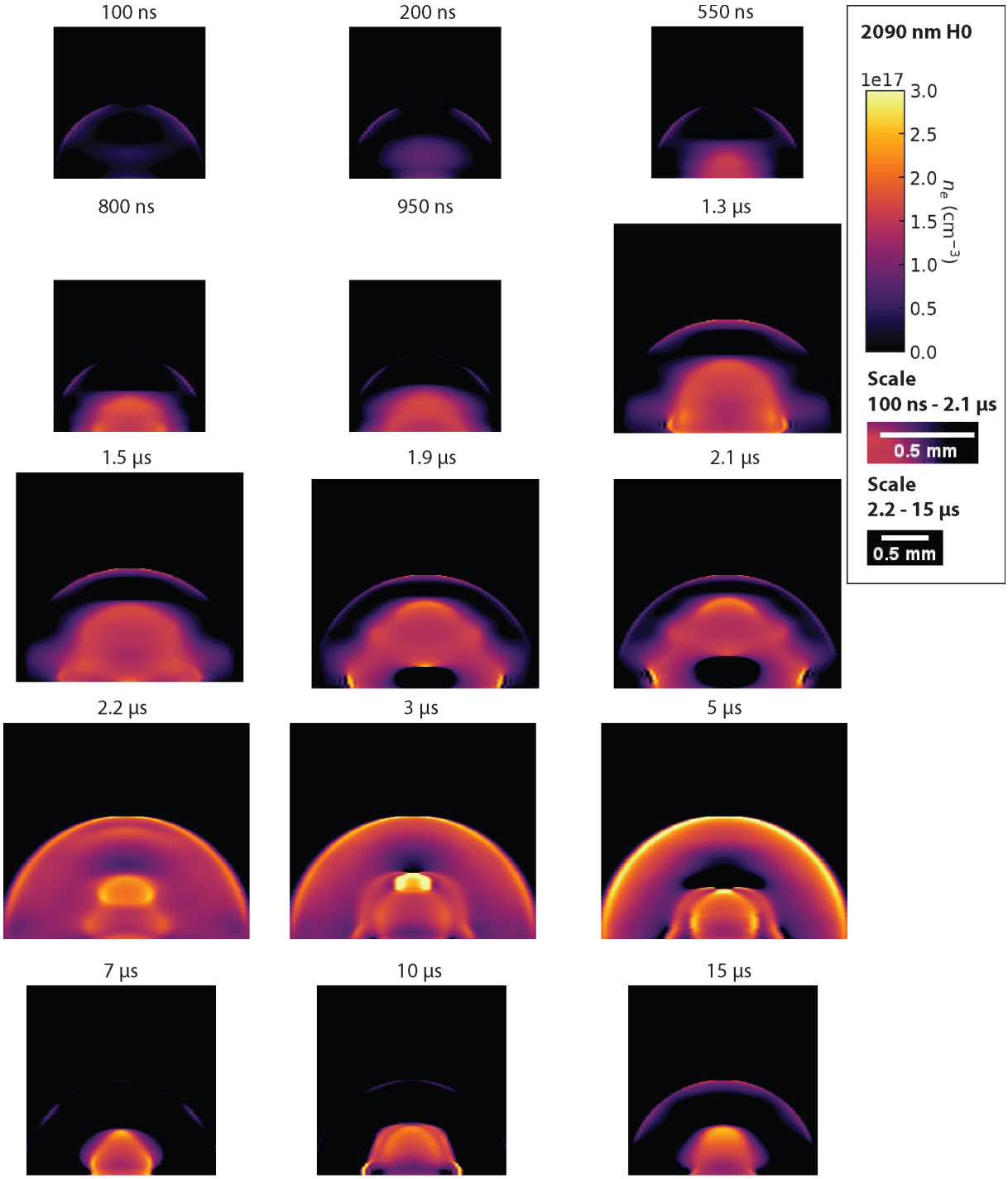

Figure 4.30: Electron density maps selection for 2090 nm H0 (without final masking). Calculated from unwrapped phase from Figure 4.29

4.4. Electron density fitting parameters

Table 4.3: Polynomial fit coefficients for H0 and H6 at 1064 nm

Power	H0 early plasma	H0 late plasma	H6 early plasma	H6 late plasma
t^0	6.12×10^{16}	1.04×10^{17}	-2.86×10^{18}	1.94×10^{17}
t^1	7.01×10^{17}	4.29×10^{16}	2.16×10^{19}	-5.74×10^{16}
t^2	-4.45×10^{18}	9.44×10^{15}	-7.60×10^{19}	5.61×10^{16}
t^3	1.44×10^{19}	-6.70×10^{15}	1.43×10^{20}	-1.58×10^{16}
t^4	-2.25×10^{19}	1.04×10^{15}	-1.48×10^{20}	1.96×10^{15}
t^5	1.65×10^{19}	-6.35×10^{13}	7.90×10^{19}	-1.12×10^{14}
t^6	-4.60×10^{18}	1.38×10^{12}	-1.70×10^{19}	2.42×10^{12}

Table 4.4: Polynomial fit coefficients for Cu and H0 at 2090 nm

Power	Cu early plasma	Cu late plasma	H0 early plasma	H0 late plasma
t^0	1.53×10^{16}	-4.35×10^{13}	-1.73×10^{16}	-6.12×10^{12}
t^1	-8.84×10^{16}	2.00×10^{15}	1.37×10^{17}	2.74×10^{14}
t^2	1.17×10^{17}	-3.48×10^{16}	-3.86×10^{17}	-4.81×10^{15}
t^3	5.44×10^{16}	2.80×10^{17}	4.44×10^{17}	4.11×10^{16}
t^4	1.92×10^{16}	-1.01×10^{18}	-2.04×10^{16}	-1.74×10^{17}
t^5		1.38×10^{18}		4.03×10^{17}

Table 4.5: Polynomial fit coefficients for H3 and H6 at 2090 nm

Power	H3 early plasma	H3 late plasma	H6 early plasma	H6 late plasma
t^0	5.21×10^{15}	4.52×10^{12}	-3.63×10^{16}	-1.74×10^{13}
t^1	-1.47×10^{16}	-2.61×10^{14}	2.50×10^{17}	7.91×10^{14}
t^2	-4.17×10^{16}	6.15×10^{15}	-5.78×10^{17}	-1.38×10^{16}
t^3	1.57×10^{17}	-7.64×10^{16}	5.34×10^{17}	1.14×10^{17}
t^4	2.09×10^{16}	5.36×10^{17}	-1.60×10^{16}	-4.37×10^{17}
t^5		-2.10×10^{18}		7.78×10^{17}
t^6		4.22×10^{18}		
t^7		-3.24×10^{18}		